

**Development of a cw-cavity ring down
spectrometer and electronic
spectroscopy of transient species**

Inauguraldissertation

Zur Erlangung der Würde eines Doktors der Philosophie

vorgelegt der

Philosophisch-Naturwissenschaftlichen Fakultät

der Universität Basel

von

Bîrză A. Petre

aus Drăgănești-Olt (Romania)

Basel, 2004

Genehmigt von der Philosophisch-Naturwissenschaftlichen Fakultät

auf Antrag von

Prof. Dr. John P. Maier und Prof. Dr. Martin Jungen

Basel, den 19.10.2004

Prof. Dr. Jakob Wirz

Dekan

To my Parents!

Acknowledgements

During the course of my Ph. D. studies, I had the fortune to meet and work with excellent people, some of whom deserve a great deal of credit for the work presented in this thesis.

I would like to thank Professor John P. Maier for his guidance and encouragement during my Ph. D. studies. I would also like to thank Professor Martin Jungen for his courteously agreement to act as my co – referee.

I am also particularly indebted to PD. Dr. Harold Linnartz for his guidance and assistance for the first 1.5 years of my study. I would like to express my appreciation to Dr. Mitsunori Araki for his supervision and contribution to preparation and presentation of scientific results described in this work.

Other people I have the pleasure of discussing and working with are Dr. Andrei Chirokolava, Dr. Przemyslaw Kolek, Dr. Dorinel Verdes and Dr. Nicola Solca. The other group members, past and present, have always been a source of fruitful discussion and enjoyable times.

I express my profound gratitude to Dr. Tomasz Motylewski for helping me with the data card acquisition part and sharing his deep knowledge with me.

I am grateful to David Pfluger for sharing with me the secrets of the cw laser and making me familiar with the field of gas spectroscopy, and to my colleague from the cw – crd – lab Dmitriy Khoroshev, Richa Chauhan.

I am also grateful to the people who were technically involved in the experiment for their effort and patience. The generous offer of their experience and knowledge is most deeply appreciated. My special thanks are especially directed to Karl Mutschler from the mechanical workshop for his service and extraordinary skills in constructing sophisticated technical devices; and to Georg Holderied for his help on the field of the electronics. I also feel especially indebted to Jacques Lecoultre for synthesizing huge amounts of exotic isotopic substances, which were used in the

experiments. I also thank our secretaries Esther Stalder and Daniela Tischauser for taken care of all bureaucratic matters.

The Swiss national Foundation and the City of Basel are thanked for financial support.

TABLE OF CONTENTS

CHAPTER 1	INTRODUCTION.....	1
1.1	GOAL OF THESIS	1
1.2	STRUCTURE OF THESIS.....	3
CHAPTER 2	THEORY OF CAVITY RING DOWN SPECTROSCOPY...4	
2.1	ABSORPTION SPECTROSCOPY	4
2.2	PRINCIPLE OF CAVITY RING DOWN	7
2.3	PULSED CAVITY RING DOWN.....	10
2.3.1	CAVITY MODES.....	14
2.3.2	SENSITIVITY OF CAVITY RING-DOWN SPECTROSCOPY	17
2.4	CONTINUOUS-WAVE CAVITY RING DOWN	19
2.4.1	SENSITIVITY	20
2.4.2	APPLICATIONS	21
	REFERENCES.....	22
CHAPTER 3	DEVELOPMENT OF CW-CRD SPECTROMETER.....	24
3.1	CW-CRD SPECTROMETER WITH A PULSED PLANAR PLASMA EXPANSION	24
3.1.1	ABSTRACT	24
3.1.2	INTRODUCTION	24
3.1.3	MECHANISM OF CW-CRD SPECTROMETER	26
3.2	SLIT NOZZLE PLASMA	31
3.3	ACOUSTO-OPTIC MODULATOR, CAVITY AND LIGHT DETECTOR	34
3.3.1	THE ACOUSTIC-OPTIC MODULATOR (AOM).....	34
3.3.2	CAVITY.....	36
3.3.3	PZT	37
3.3.4	LIGHT DETECTOR.....	39

Table of contents

3.4	CONTINUOUS WAVE LASER SETUP	40
3.5	CONTROLLING EXPERIMENTAL CONDITIONS	43
3.6	DATA ACQUISITION	49
3.7	RESULTS.....	53
3.8	CONCLUSION	54
	REFERENCES.....	56
	APPENDIX 1.....	58
	APPENDIX 2.....	61
CHAPTER 4 HIGH RESOLUTION SPECTROSCOPY WITH CW-CRD		
SPECTROMETER.....		64
4.1	LIFETIME BROADENING IN THE GAS PHASE $\tilde{B}^2\Pi \leftarrow \tilde{X}^2\Pi$ ELECTRONIC SPECTRUM OF C_8H	64
4.1.1	ABSTRACT	64
4.1.2	INTRODUCTION	64
4.1.3	EXPERIMENTAL APPROACH.....	65
4.1.4	RESULTS AND DISCUSSION.....	66
4.2	ROTATIONALLY RESOLVED ELECTRONIC SPECTRUM OF PROPADIENYLIDENE	70
4.2.1	ABSTRACT	70
4.2.2	INTRODUCTION	70
4.2.3	EXPERIMENT.....	73
4.2.4	RESULTS AND DISCUSSION.....	74
4.2.4.1	ROTATIONAL ANALYSIS	74
4.2.4.2	AB INITIO CALCULATIONS	81
4.2.5	MOLECULAR STRUCTURE	84
4.2.6	CONCLUSION.....	86
	REFERENCES.....	90
	APPENDIX 1 SENSITIVITY.....	93

Table of contents

APPENDIX 2	SHOT NOISE LIMIT	94
CHAPTER 5	CONCLUDING REMARKS AND OUTLOOK.....	96
5.1	CONCLUDING REMARKS	96
5.2	OUTLOOK	97
5.3	PUBLICATION IN JOURNALS DURING PH. D. STUDIES.....	99
5.4	CURRICULUM VITAE OF AUTHOR	100

List of figures

- 2.1 Basic principle of CRD spectroscopy (upper figure), and a more realistic diagram (lower figure)
- 2.2 Decay of the light leaking out of the cavity (upper figure) and result in extra losses $k(\nu)$ to a species in the cavity (lower figure)
- 3.1 Overview of cw-CRD experiment
- 3.2 An artist's view of the high pressure slit nozzle discharge. The orifice consists of two sharp stainless steel jaws (actual slit), a ceramic insulator, a slotted metal plate (grounded) and a second ceramic insulator. Both insulators and metal parts are mounted to the body of the nozzle using electrically isolated screws. A pulsed negative high voltage is applied to the jaws via ballast resistors at the moment that a high pressure gas pulse expands through the channel. The discharge strikes to the grounded plate, localizing the reaction zone to a region upstream of the expansion. The body is floating and connected to an electromagnetic driven pulsed valve. A multi-channel system inside the nozzle regulates the gas flow towards the slit and allows a further reduction of the Doppler broadening.
- 3.3 Schematic of the whole experimental setup
- 3.4 Timing and triggering scheme. I. A 30 Hz ramp is applied to a piezo element. II. The photodiode shows when cavity resonances occur. The data-acquisition program chose the transmission closest to the middle of the ramp, defining t_0 and the ramp voltage for which the resonance occurs. When the transmission intensity exceeds a certain threshold, the AOM is switched off and a ring

down event is induced. III. The program defines a 300 μs time window in which the next resonance is expected. In order to circumvent hysteresis effects only signals on positive or negative ramps are taken. IV. t_0 is also used 11 to trigger the gas and discharge pulse every second ramp. The plasma free ring down event is used for background subtraction. Further details are given in the text.

- 3.5 High pressure slit nozzle discharge
- 3.6 Slit nozzles with a series of cylindrical holes
- 3.7 High pressure slit nozzle discharge with new multi channel body
- 3.8 Diffraction of a light beam by traveling acoustic plane waves in a acousto-optic modulator
- 3.9 Schematic description of the cavity
- 3.10 Electrical connection of disks in a PZT stack actuator
- 3.11 Photodiode amplifier circuit
- 3.12 Ring laser tuning curves
- 3.13 Data card acquisition system. One is used to control the analog channels and to send analog spectrum to the autoscan computer via network and the second one just to receive the data from the photodiode (small spikes) and to generate the ramp voltage. By this means the noise coming from the valves can be avoided
- 3.14 Relative timing of the piezo ramp voltage, cavity resonances, valve opening, and high voltage pulse applied to the slit electrodes. (a) Ramp voltage applied to the piezo. (b) Signal on the photodetector
- 3.15 Parameters used to control delays. The labels on the arrows are the parameters used in the data acquisition program and correspond to the next parameters from the shm.tcl panel: d_{laser} – laser delay, $d_{\text{dis_laser}}$ – discharge – laser delay, w_{dis} – discharge length, $d_{\text{valve_dis}}$ – valve discharge delay, w_{valve} – valve opening

- 3.16 Nonlinearity of the piezo element
- 3.17 User interface (shm.tcl) used for tuning crdst-rt.o RTLinux trigger generator.
- 3.18 Data acquisition. DIO – Digital Input/Output, DMA – Direct Memory Access, crdst.c – multiple real time control threads
- 3.19 User interface (crd.tcl) used for tuning crdst-rt.o RTLinux trigger generator a – run/stop the program, b – measure the ring down on the ramp up or down, c – frequency of the ramp samples, d – counter of the ring downs, e – the minimum and maximum of the ring down, f – minimum and maximum absorption used for scaling analog absorption output, g – define the number of points to fit of samples to fit $b \cdot \exp(-a \cdot t) + c$ function, h – detection threshold for vacuum (blue), i – detection threshold for jet (red), j – ring down events.
- 3.20 User interface (scan) used for recording spectra
- 3.21 The origin band of the $\tilde{A}^2\Pi_g \leftarrow \tilde{X}^2\Pi_u$ electronic spectrum of triacetylene cation, HC_6H^+ , measured by cw-CRD spectroscopy through a supersonic pulsed planar plasma. The inset shows the corresponding spectrum measured in a ‘hot’, *i.e.* liquid N_2 cooled environment with $T_{\text{rot}} \approx 170$ K
- 3.22 PZT unit cell: 1) Perovskite-type lead zirconate titanate (PZT) unit cell in the symmetric cubic state above the Curie temperature. 2) Tetragonally distorted unit cell below the Curie temperature
- 4.1 Experimental spectra of the origin band in the $\tilde{B}^2\Pi_{3/2} \leftarrow \tilde{X}^2\Pi_{3/2}$ electronic transition of C_8H .

- 4.2 Rotationally resolved CRD absorption spectrum of the ${}^2\Pi_{\frac{3}{2}} \leftarrow {}^2\Pi_{\frac{3}{2}}$ electronic origin band transition of HC_8H^+ , recorded through a supersonic planar plasma $T_{\text{rot}} \approx 15$ K
- 4.3. Experimental and simulated spectra of the origin band in the $\tilde{B}^2\Pi_{\frac{3}{2}} \leftarrow \tilde{X}^2\Pi_{\frac{3}{2}}$ electronic transition of C_8H
- 4.4 Structure of CCCH_2 using rotational constants from the ground state
- 4.5 Rotationally-resolved spectrum of C_3H_2 (trace **c**) in comparison with the simulated ones: trace **a** using the independent Boltzmann population model, trace **b** a single Boltzmann population for the two nuclear spin isomers (spin statistical weights ee:eo:oe:oo=1:1:3:3). The broad structure around 15970 cm^{-1} is the origin band of the $\tilde{B}^2\Pi_{3/2} - \tilde{X}^2\Pi_{3/2}$ transition of C_8H .
- 4.6 Schematic potentials of the ${}^1\text{A}_2$ and ${}^1\text{B}_1$ states and the intersection point. The parameter k is used to define the intersection point between the states.
- 4.7 Diffuse interstellar bands in the 628 nm region (lowest trace) taken from ref. 55 and the simulated C_3H_2 spectrum obtained using the independent Boltzmann population model for 10, 40 and 150 K (upper three traces) using 0.2 cm^{-1} (FWHM) for the rotational lines.

List of Tables

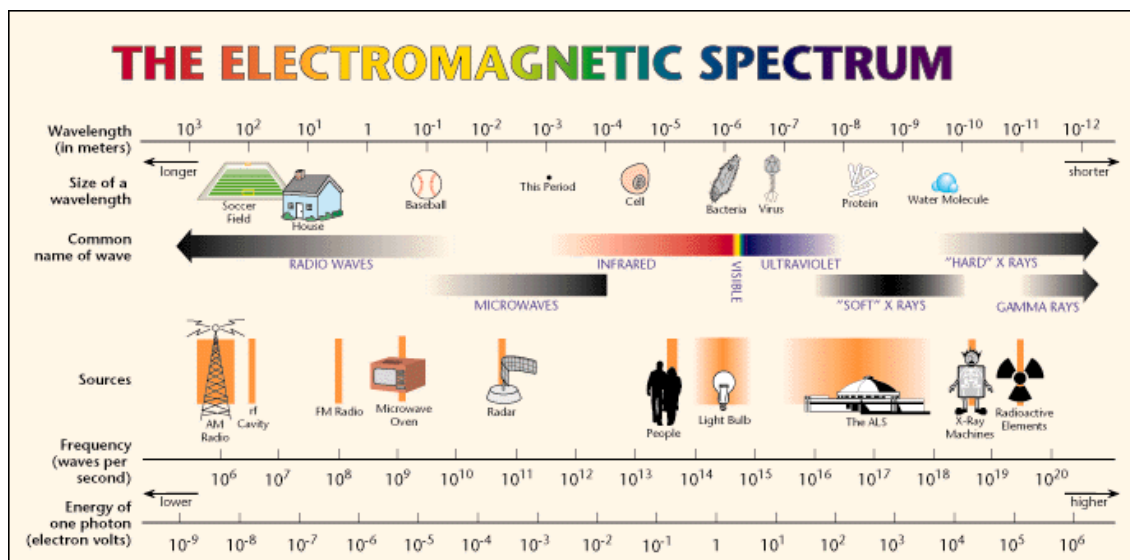
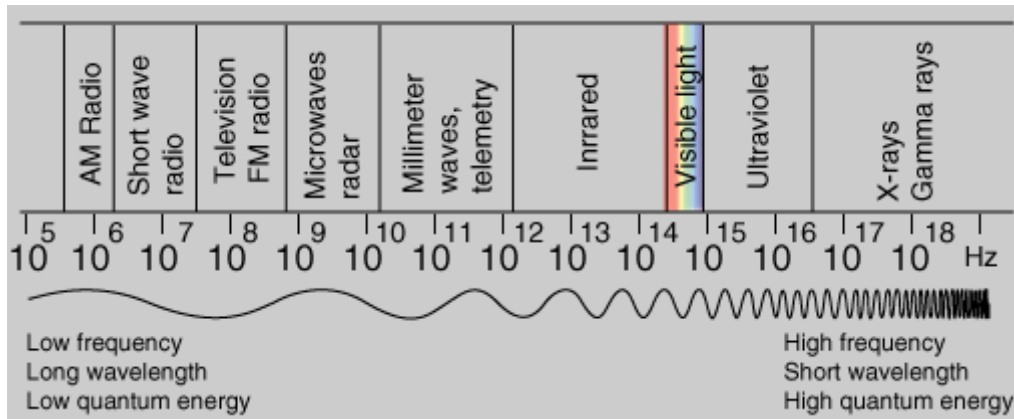
- 3.1 Available tuning ranges and configurations for the ring laser system
- 3.2 Correspondence between source-program and function
- 4.1 Frequencies of the observed rovibronic lines in the $\tilde{A}^1A_2 \leftarrow \tilde{X}^1A_1$ transition of C_3H_2
- 4.2 Molecular constants (cm^{-1})^a of C_3H_2
- 4.3 Adiabatic transition energies (eV) of C_3H_2
- 4.4 Calculated vibrational frequencies (cm^{-1}) of C_3H_2
- 4.5 Molecular structure and rotational constants of C_3H_2 ^a
- 4.6 Computed relative energies for the 1A_2 , 1B_1 and intersection point, and the geometry of the intersection point.

Abbreviation

AOM	- acousto-optical modulator
CASPT3	- complete active space perturbation theory 3 rd order
CASSCF	- complete active space self consistent field
CAS6	- active spaces for CASSCF, including 6 orbital
CAS10	- active spaces for CASSCF, including 10 orbital
CLCW-CRD	- cavity locked cw-CRD
CRD	- cavity ring-down
CW	- continuous wave
cw-CRD	- continuous-wave cavity ring down
DIB	- diffuse interstellar band
DIO	- digital input/output
DMA	- direct memory access
FPM	- frequency plasma double modulation
FSR	- free spectral range
FWHM	- full width at half maximum
HV	- high voltage
MRCI	- multi reference configuration interaction
IR	- infrared (wavelengths: 1mm – 750nm)
OPO	- optical parametric oscillators
OAM	- optical activity monochromator
PD	- photodiode
PID	- proportional integral, derivative
PZT	- piezoelectric translators
PL-CC	- plano-concave
RSPT3	- Rayleigh - Schrödinger perturbation theory 3 rd order
S/N	- signal-to-noise-ratio
TEM ₀₀	- transverse electromagnetic mode (fundamental mod)
Ti:S	- titanium: sapphire

Abreviation

- VET - vernier etalon
 VIS - visible spectrum (wavelengths: 400 nm – 750 nm)
 UV - ultraviolet (wavelengths: 400 nm - 10 nm)



Chapter 1 Introduction

1.1 Goal of thesis

The study of molecular absorption and emission of radiation is of great importance in basic and applied science. Much of our knowledge on the geometrical and electronic structure of various molecules and molecular clusters stems from optical absorption studies performed in either bulk samples or, in molecular beam expansions. For many applications involving large polyatomic molecules, however, absorption measurements are potentially superior to those based on emission since rapid quenching (through energy redistribution processes) of the excited state will occur resulting in a greatly reduced emission quantum yield.

In the limit of weak absorption the transmitted optical intensity decreases exponentially with absorption path length, in accordance with Beer's law, where the exponential decay constant, k , is the absorption coefficient at the frequency of the incident beam. The ability to accurately measure the ratio of I to I_0 typically limits the measurement to minimum losses of 0.01% to 0.001% and, as a rule, such precision absorption measurements require sophisticated optical systems and sources (often laser based) which have a stable output intensity. The required intensity stability has been achieved using several types of continuous lasers (e.g. infrared lasers diode lasers and tunable continuous wave dye lasers) using experimental configurations which typically employ some form of frequency modulation to discriminate against low frequency noise. The same success has not yet been possible for experimental systems based upon pulsed laser sources for several reasons. First, the pulse to pulse amplitude variation is typically large, greater than 10%, requiring a larger detector dynamic range and reducing the effective signal resolution. In addition, the short pulse widths of such lasers, typically 10-30 nsec, make it very difficult to modulate the frequency for differential analysis.

In our laboratory a very successful experiment was already developed, based on frequency production double modulation spectroscopy of static plasma generated in a discharge cell. However, here the temperature is high ($T_{rot}=150$ K), which produces a temperature broadening. Three qualities: high resolution, low temperature and Doppler-free are required simultaneously to solve the problem with laboratory spectroscopy. The solution was to construct a cavity ring down experiment using a continuous laser and slit jet.

A continuous wave cavity ring down spectrometer has been constructed with the aim to record the electronic spectrum of rotationally-cold carbon chain radicals at high spectral resolution in direct absorption. The radicals are generated in a discharge of a high pressure gas pulse of acetylene in helium in a multilayer slit nozzle. A passive cavity mode locking scheme has been developed to handle refractive index changes inside the cavity caused by gas pulse and plasma fluctuations.

A continuous wave cavity ring down spectrometer has the advantage that it is easier to record weak signals due to a single mode laser in resonance with only one transversal mode at a time. When multimode pulsed laser linewidth is much larger than cavity free spectral range, pulse to pulse give a fluctuation of spectral energy distribution. In case of a cw laser, we have one cavity mode at the same optical frequency. High accuracy (0.007 cm^{-1}) and a linewidth of typically 500 KHz, gives the possibility to resolve the rotational structure. Another big advantage of a cw spectrometer is the low intracavity optical power of a few W/cm^2 , giving a stable transverse distribution. (In contrast, pulsed lasers have a very high intracavity optical power: the fluxes are of the order of MW/cm^2 and the energy is then distributed over several transverse and longitudinal modes.)

1.2 Structure of thesis

This thesis has the following structure:

Chapter 2 provides a detailed description of the theory of cavity ring down spectroscopy. This chapter is structured in two parts: pulsed cavity ring down and continuous wave spectroscopy.

Chapter 3 contains the description of the spectrometer; additionally, it contains the details of the main components of the experiment from a theoretical point of view and more detailed description of the data acquisition and software.

Chapter 4 describes the high resolution spectroscopy with a cw-CRD spectrometer. Two studies of the origin band of the $\tilde{B}^2\Pi_{3/2} \leftarrow \tilde{X}^2\Pi_{3/2}$ electronic transition of linear C_8H and the rotationally-resolved vibrational band in the $\tilde{A}^1A_2 \leftarrow \tilde{X}^1A_1$ transition of a short cumulene carbon chain C_3H_2 measured in the 625 nm region using supersonic planar discharge are presented.

Chapter 2 Theory of cavity ring down spectroscopy

2.1 Absorption spectroscopy

Molecules (and atoms) absorb electromagnetic radiation of specific frequencies. The rate of absorption depends on the nature of the species, the frequency of the light and external condition such as temperature and pressure. The frequency dependence of absorption is unique; each species possesses a ‘spectrum’ of frequency dependent absorptions. Measurement of a spectrum can be used to determine the nature of an unknown species or conditions of known species, such as concentration and temperature. Absorption of light under conditions where saturation does not occur, described by Beer’s law:

$$I_{(\nu)}^l = I_{(\nu)}^0 \cdot \exp\{-\sigma(\nu)nl\} \quad (2.1)$$

where $I_{(\nu)}^0$ is the intensity of an incident light beam at frequency ν , $I_{(\nu)}^l$ the intensity of that beam after a distance l through the absorbing medium, n the number density of the species, and $\sigma(\nu)$ the frequency-dependent absorption cross section from Eq. 2.1,

$$\alpha(\nu) = \frac{1}{l} \ln \left(\frac{I_{(\nu)}^0}{I_{(\nu)}^l} \right) \quad (2.2)$$

The lowest absorption detectable by conventional direct absorption techniques is limited by the minimum intensity change that can be measured and the absorption path length. A first order Taylor expansion of Beer’s law:

$$\alpha(\nu) = 1 - \alpha(\nu)l \quad (\alpha(\nu)l \ll 1) \quad (2.3)$$

reveals the limitations. Substituting Eq. 2.3 in Eq. 2.1 simplifies Eq. 2.2 to

$$\alpha(\nu) = \frac{I(\nu)^0 - I(\nu)^l}{I(\nu)^0 l} = \frac{\Delta I(\nu)}{I(\nu)^0 l} \quad (2.4)$$

It is evident from Eq. 2.4 that the detection limit is governed by intensity fluctuations. The sensitivity of conventional direct absorption techniques can be improved by increasing the absorption path length, l . Very long absorption path lengths are achieved in sunset spectra of the Earth's atmosphere [1], with absorption sensitivities of $\approx 10^{-11} \text{ cm}^{-1}$ [2]. In laboratory, multi-pass absorption cells can be used to increase the effective absorption path length. Commonly used are the White cell [3] and the Herriot configuration [4].

Incoherent absorption spectroscopic technique uses broad-band light sources e.g. (lamp, sun). Absorption spectra can be obtained through the use of a dispersive element (grating, prism) that unravels the light in its frequency components before the light reaches the detector. This can be a diode array, a CCD camera, or a photographic plate [5]. The resolution and the sensitivity achieved are remarkable. The 1948 study of Babcock and Herzberg [1], using data from the sunset spectrum of the Earth's atmosphere of the forbidden $b^1\Sigma_g^+ - X^3\Sigma_g^-$ transition in O_2 , can still compete with recent spectroscopic studies of O_2 isotopomers [6]. These techniques benefit greatly from the multiplex advantage of detecting a wide frequency range at all times. Fourier transform spectroscopy possesses the additional advantage of a high light intensity, there is no narrow entrance slit which severely restricts the radiation throughput in a prism or a grating spectrometer [5].

A tunable laser source enables recording of an absorption spectrum by detecting the transmitted intensity of the laser beam while the frequency is scanned. The sensitivity is limited by the minimum detectable intensity change, but normalization of the transmitted intensity with respect to the incoming intensity can yield a signal-to-noise-ratio (S/N) in a spectrum of better than $\approx 10^{-6} \text{ cm}^{-1}$. Further sensitive techniques (up to $\approx 10^{-10} \text{ cm}^{-1}$) use absorption-induced effects, such as intracavity laser absorption spectroscopy and frequency modulated spectroscopy. Although these techniques cannot measure direct absorption the obtained signals are

Theory of cavity ring down spectroscopy

directly correlated to the absorption coefficient $\alpha(\nu)$, unlike in techniques as photoacoustic spectroscopy, laser induced fluorescence, and resonance enhanced multiphoton ionisation. The latter three techniques need calibration against signals from known absorption for quantitative absorption measurements.

The above mentioned techniques are often more sensitive than direct absorption techniques, but cannot measure absorption directly. The cavity ring down (CRD) technique, however, can measure absorption directly and is a few orders of magnitude more sensitive than all other direct absorption techniques.

2.2 Principle of cavity ring down

Cavity ring-down spectroscopy is a direct absorption technique, which can be performed with pulsed or continuous light sources and has a significantly higher sensitivity than obtainable in conventional absorption spectroscopy. The CRD technique is based upon the measurement of the rate of absorption rather than the magnitude of absorption of a light pulse confined in a closed optical cavity with a high Q factor. The advantage over normal absorption spectroscopy results from, firstly, the intrinsic insensitivity to light source intensity fluctuations and, secondly, the extremely long effective path lengths (many kilometers) that can be realized in stable optical cavities. In the last decade, it has been shown that the CRD technique is especially powerful in gas-phase spectroscopy for measurements of either strong absorptions of species present in trace amounts or weak absorptions of abundant species.

A typical CRD cavity is a stable, linear resonator with identical mirrors. To form a stable resonator with identical mirrors the geometry of the cavity has to obey the criterion

$$0 < g^2 < 1 \quad (2.5)$$

where $g = 1 - d/r_c$, d is the cavity length, and r_c the curvature radius. For a given radius of curvature of the mirrors the cavity length of a stable resonator is restricted to values between 0 and $2r_c$. Due to boundary conditions only light with frequencies that match resonator modes can be coupled into an optical resonator and will propagate unchanged inside the resonator. The trapped light in the resonator can be described as a superposition of longitudinal and transversal modes.

The mode spectrum of a stable confocal resonator ($d = r_c$) is given by:

$$\nu = \frac{c}{2d} \left(q + \frac{1}{2}(m + n + 1) \right) \quad (2.6)$$

where q is the longitudinal mode index, and m and n are the transverse-mode indices. A mode is represented by TEM_{qmn} , where the longitudinal mode index q is often omitted for simplicity.

The frequency difference between two successive transverse modes n and $n+1$, the Free Spectral Range (FSR), is:

$$\delta\nu_{trans} = \frac{c}{4d} \quad (2.7)$$

while the distance between two longitudinal modes q and $q+1$ is:

$$\delta\nu_{long} = \frac{c}{2d} \quad (2.8)$$

The mode structure of the resonator can have considerable effects on CRD measurements. When the bandwidth of the probing laser is much narrower than the FSR of a confocal cavity a continuous scan is not possible, and absorption can be missed if the FSR is larger than the width of absorption. The absorption could remain unnoticed in a 10 cm long confocal cavity with an FSR of 0.05 cm^{-1} because the absorption line may fall exactly between two successive cavity modes.

The frequency spectrum of the resonator can be made quasi-continuous by changing the geometry from confocal to a stable, nonconfocal geometry. When the distance d , between the mirrors is not equal to r_c and the resonator geometry satisfies the stability criteria (Eq. 2.5), the degeneracy of the modes is lifted and frequency spectrum becomes:

$$\nu = \frac{c}{2d} \left(q + \frac{1}{2}(m+n+1) \left(1 + \frac{4}{\pi} \arctan \left(\frac{d-r_c}{d+r_c} \right) \right) \right) \quad (2.9)$$

Multiple mode excitation, however, can result in mode beating effects and nonexponential decay of the light intensity. Beating between different frequency components (modes) can result in a periodic signal superimposed on the decay transient, if for example the output of the cavity is not completely collected with equal

efficiency. This beat signal can influence the determination of the decay rate. Non-exponential decay can occur when the loss in the cavity is not equal for each mode, even if no absorptions is present. The empty cavity loss β_0 is then not mode independent because different transverse modes TEM_{mn} experience different Fresnel losses. As a result the decay of the light intensity in the cavity is a superposition of decays with slightly different decay rates:

$$I(t) = I \sum_{mn} e^{-\beta_0^{mn} t} \quad (2.10)$$

2.3 Pulsed cavity ring down

A short laser pulse of light with intensity I_{in} is ‘coupled’ into a stable cavity of length d , consisting of two highly reflecting curved mirrors with a reflectivity R , loss L , and transmittance T ($R+L+T=1$). At each mirror, a small part T of the trapped light leaks out while the remaining part is reflected, as schematically shown in Fig 2.1.

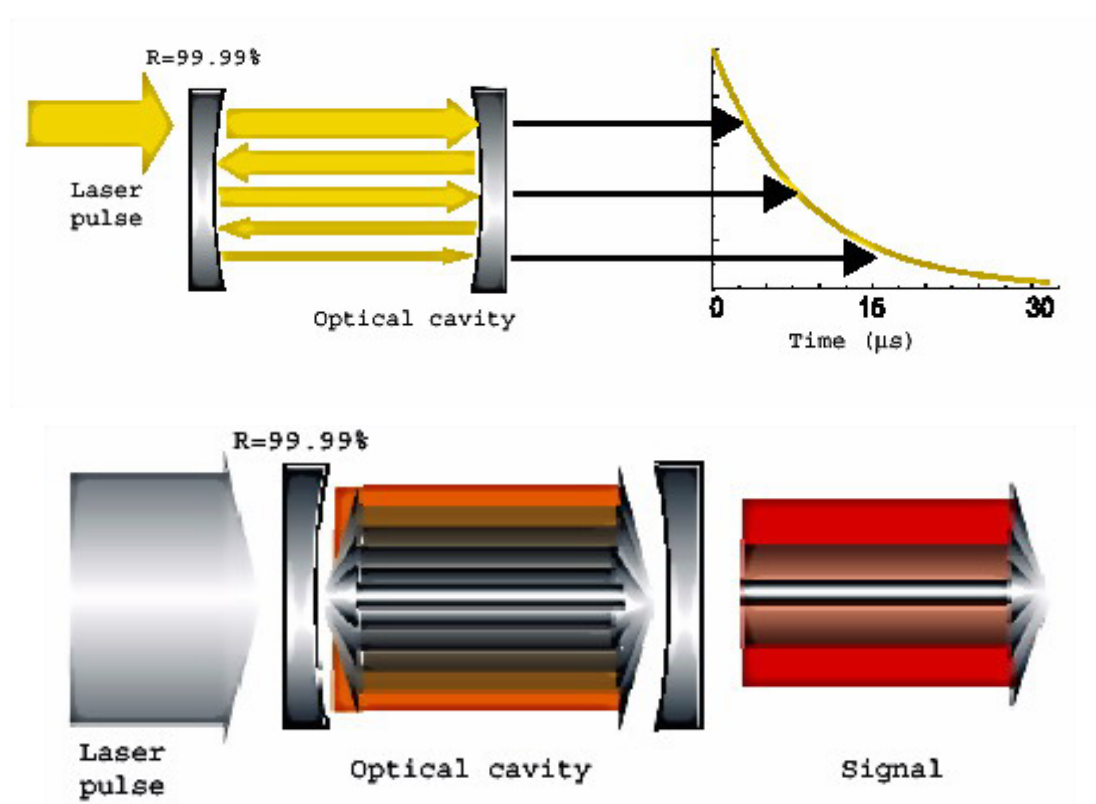


Figure 2.1 Basic principle of the CRD spectroscopy (upper figure), and a more realistic diagram (lower figure)

The first pulse of light leaking out of the cavity will have the intensity $I_0 = T^2 I_{in}$. The n^{th} pulse with intensity

$$I_n = I_0 R^{2(n-1)} = I_0 \exp\{2(n-1)\ln(R)\} \quad (2.11)$$

will leak out $(2d(n-1)/c)$ seconds after the first pulse, where c is the speed of light; the exponent is negative because $R < 1$. When the cavity is shorter than the light pulse and due to limited response time of the detection circuit, the pulses leaking out of cavity will overlap and smear out to a continuously decaying signal as a function of time t ,

$$I(t) = I_0 \exp\left\{-\left(\frac{c}{d}\right)|\ln(R)|t\right\} \quad (2.12)$$

The decay rate of an empty cavity β_0 , or the decay time $\tau_0 = 1/\beta_0$, is the background signal of a spectrum recorded with the CRD technique. This decay rate β_0 is determined by the reflectivity R of the mirrors and the cavity length d :

$$\beta_0 = \frac{c|\ln(R)|}{d} \quad (2.13)$$

Additional losses in the cavity will result in a faster decay. These losses can be due to species in the cavity (absorption, Rayleigh scattering). To distinguish between the frequency dependent, absorption coefficient $\alpha_{(\nu)}$ and species induced extinction in general, the extinction coefficient is represented by $k_{(\nu)}$. If the extra losses are only due to absorption, $k_{(\nu)} = \alpha_{(\nu)}$.

When the additional losses satisfy Beer's law, the decay remains exponential:

$$I_n = I_0 R^{2(n-1)} \exp\left\{-2(n-1)k_{(\nu)}l\right\} = I_0 \exp\left\{2(n-1)\ln(R) - 2(n-1)k_{(\nu)}l\right\},$$

hence

$$I(t) = I_0 \exp\left\{-\left(\frac{c}{d}\right)(|\ln(R)| + k(\nu)l)t\right\} \quad (2.14)$$

where $k(\nu)$ is the extinction coefficient of a species inside the cavity, ν the frequency, and l the single pass absorption path length. The decay rate β in case of additional

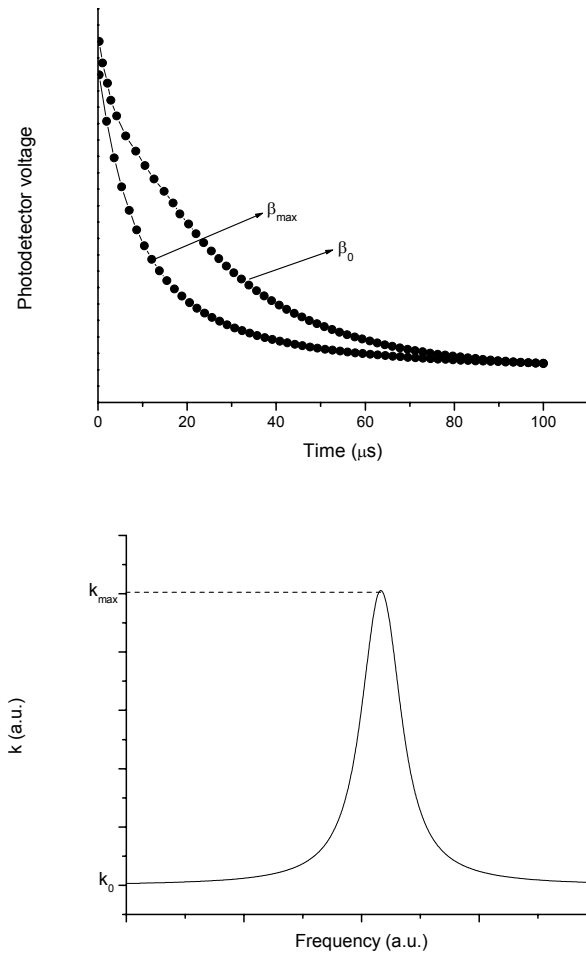


Figure 2.2 Decay of the light leaking out of the cavity (upper figure) and result in extra losses $k(\nu)$ to a species in the cavity (lower figure)

extinction is larger than β_0 , as schematically shown in Fig. 2.2, and is given by

$$\beta(\nu) = \frac{c}{d} (\ln(R) + k(\nu)l) \quad (2.15)$$

From Eq. 2.7 and 2.9 the extra loss in the cavity follows:

$$\beta - \beta_0 = \frac{c}{d} k(\nu)l \quad (2.16)$$

hence

$$k(\nu) = \frac{d(\beta - \beta_0)}{l c} \quad (2.17)$$

When the cavity is completely filled with the medium of interest d and l cancel and Eq. 2.17 becomes

$$k(\nu) = \frac{(\beta - \beta_0)}{c} \quad (2.18)$$

The coefficient $k(\nu)$ measured as a function of frequency constitutes, in case of absorption, an absorption spectrum in which β_0/c is the background level.

The CRD technique has two marked advantages. At first, information on absorption is embedded in the decay rate of the light intensity leaking out of the cavity, and is thus independent of intensity fluctuations. Secondly, the use of low loss optical resonators enhances the absorption path length; up to 100 km in a 1 m long cell can be achieved.

Some remarks must be added to the explanation of the principle of the CRD technique. Since the two mirrors are not equal, R used in the explanation is a geometric average $\sqrt{R_1 R_2}$ of the reflectivity R_1 and R_2 of the two mirrors. Furthermore, not only the transmission T and the reflectivity R of the mirrors are involved. Additional independent losses L have to be taken into account, i.e., diffraction, scattering, and absorption of light by the substrate of the mirrors. In an experiment the background signal is the equivalent of an ‘effective reflectivity’: $R_{\text{eff}} = 1 - (T + L)$. In the following R_{eff} is assumed, unless stated otherwise. The reflectivity R may be frequency dependent, which can result in a slope in the background of a frequency scan, but often the effect is negligibly small and the background is constant.

Whereas these effects are easily accounted for, effects due to the finite line width of the exciting laser pulses are not. Both the laser and the absorption cross sections possess a spectral distribution. If $(dk(\nu)/d\nu) \neq 0$ within the laser bandwidth Eq. 2.14 should be replaced by

$$I(t) = \int_{\nu} I(\nu) \exp\{-\beta(\nu)t\} d\nu \quad (2.19)$$

which does not result in a mono-exponential decay. A mono-exponential decay fit of Eq. 2.19 leads to the underestimation of the decay rate, which in turn gives the underestimation of $k(\nu)$ [7 - 9]. This effect is comparable to the ‘slit function problem’ of other spectroscopic techniques. However, correction for these effects in CRD spectroscopy is not trivial, since each frequency component within the laser bandwidth profile will give rise to a different decay time, thus producing multi-exponential decay.

2.3.1 Cavity modes

Above, a rather simplified picture of CRD spectroscopy has been given, namely a pulse of light which is reflected back and forth in a high-finesse optical cavity. This picture gives the impression that this process is independent of the frequency of the laser light exciting the cavity, which is obviously not the case since we have to consider the mode structure. This can cause several problems. Narrow molecular absorption features might fall between the cavity modes and these features will then be absent in the spectrum. Furthermore, beating, resulting from multimode excitation, can generate oscillations in the ring-down transient, which prevents the accurate determination of the decay time τ .

Potential problems associated with the mode structure can easily be circumvented by using a stable optical cavity with a near-continuum mode structure [10, 11]. In general, a cavity has both longitudinal and transverse modes. The frequency of a TEM_{qmn} mode having a longitudinal index q and transverse indices m , n is given by [9]:

$$\nu_{qmn} = \frac{c}{2d} \left[q + (m+n+1) \frac{2}{\pi} \arctan \left(\frac{d}{[d(2r-d)]^{1/2}} \right) \right] \quad (2.20)$$

From this equation it is seen that the longitudinal mode spacing (often referred to as the free spectral range of the cavity) is $\Delta\nu=c/2d$ and that the transverse mode spacing

is given by $(c/\pi d) \arctan \frac{d}{[d(2r-d)]^{1/2}}$. Therefore, the mode structure in the cavity is a continuum when the ratio of the transverse to longitudinal mode spacing is irrational.

Experimentally, such a continuum can readily be achieved. First of all, no mode matching optics should be used to couple light into the cavity. Second, the cavity should be stable (and non-confocal), that is $0 < d < r$ or $r < d < 2r$. Third, the ratio of the mirror diameter to the length of the cavity should be not too small in order to ensure that the transverse modes remain in the cavity (i.e. the diffraction losses of the transverse modes should be minimized). Finally, care should be taken that all modes exiting the cavity are detected with equal efficiency, since transverse modes are spatially more extended. For example, a cavity with a length of 50 cm, mirrors with a diameter of 25 mm, and curvature radius r of 1 m satisfies the second and third conditions. All modes are detected by placing a photomultiplier directly behind the cavity. If the effective surface of the detector is small, a lens with an appropriate diameter and a short focal length should be used to focus the light onto the detector.

Since the bandwidth of the excitation laser is often much larger than the (residual) mode spacing, many modes are excited. As shown by Hodges *et al.* (1996b), the excitation of many (transverse) modes dramatically reduces the modulation depths of the beats observed in the ring-down transients. By making the cavity mechanically unstable, the mode spacing varies, assuring that all frequencies are coupled into the cavity with an ‘equal probability’ (this also assures that the ratio of transverse and longitudinal modes is most of the time irrational). When the ring-down transients are averaged, the residual mode beating effects are further minimized, leading to a single exponentially decaying transient. Note that mode beating effects in the transient are often difficult to observe owing to a ‘slow’ detector response or electronic filtering.

There are a few disadvantages of the continuum-mode approach. First of all, the spatial resolution of CRD spectroscopy is not optimal because of the spatial extent of the transverse modes. Spatial resolution is important in experiments where one wants to map out the spatial distributions of molecular species [12, 13]. Exciting only longitudinal modes (‘TEM₀₀ mode matching’) improves the spatial resolution and can

be achieved by using mode matching optics to couple the laser light into the cavity, or by using small-diameter mirrors [17], or by placing apertures in the cavity [9, 15].

Another disadvantage of the continuum-mode approach is the ultimate sensitivity that can be obtained [9], which is important for quantitative high sensitivity absorption measurements. The accuracy in the determination of the decay time is limited owing to very small quasirandom variations in the residual transverse mode beating. The ultimate sensitivity is obtained if only one single longitudinal mode is excited in the cavity, giving a truly single-exponential decay [14].

Lehmann and Romanini [17] suggested that one can perform CRD spectroscopy with a higher spectral resolution than the laser which is used to excite the cavity. In order to perform such an experiment, the mode spacing of the cavity should be larger than the spectral width of the laser, and the length should be carefully controlled in order to prevent drift of the modes [14].

It should be noted that pure TEM_{00} mode matching is not straightforward. As shown above, observing a single-exponentially decaying ring-down transient does not have to indicate that a single mode is excited in the cavity, since this can also be due to excitation of (many) transverse modes and/or slow detector response. A charge coupled device camera should be used in order to visualize the mode pattern (spatial structure) of the light exiting the ring-down cavity [9]. This provides a way to maximize coupling into the TEM_{00} modes.

A more extensive discussion on the mode structure in a ring-down cavity, and how this affects the ring-down transient (mode beating) and the measured absorption spectrum, can be found in the work by Zalicki and Zare (1995), Martin *et al.* (1996), Lehmann and Romanini (1996), [9, 18]. However, it should be emphasized that, for the majority of CRD applications, problems associated with the mode structure of the ring-down cavity are largely absent.

2.3.2 Sensitivity of cavity ring-down spectroscopy

The absorption coefficient is obtained from a CRD spectrum after subtracting the cavity loss measured without the absorber. Practically, however, one determines the cavity loss without an absorber from the baseline in the spectrum.

$$\kappa(\nu)\frac{l}{d} = \frac{1}{c\tau} - \frac{1}{c\tau_0} = \frac{\tau_0 - \tau}{c\tau_0\tau} \quad (2.21)$$

in which τ_0 is the decay time measured without an absorber [14]. This equation shows that measuring the absorption coefficient simply involves the determination of two time constants. Furthermore, it shows that, for a simple static cell experiment where $l=d$, the absorption coefficient does not depend on the actual length of the cell. Therefore, the sensitivity of a CRD experiment is determined by the accuracy with which the ring-down times can be determined.

The minimum detectable absorption in CRD spectroscopy depends on the reflectivity R of the mirrors and on the accuracy in the determination of τ [15] :

$$[\kappa(\nu)l]_{\min} = (1 - R) \left(\frac{\Delta\tau}{\tau} \right)_{\min} \quad (2.22)$$

It should be emphasized that R in this equation is in fact R_{eff} which is smaller than (or equal to) the reflectivity of the mirrors. Equation (2.22) shows an attractive feature of CRD spectroscopy; in order to achieve high sensitivity in the absorption measurement, only a rather low accuracy in the time measurement is needed. For example, 1% accuracy for the determination of τ combined with a cavity 10 cm long consisting mirrors with a reflectivity of 99.999%, leads to a minimum detectable absorption of 10^{-8} cm^{-1} .

The obtainable accuracy of τ is determined by many factors, for example, the laser system (bandwidth, modes and power), cavity (mirror reflectivity and modes),

detector, data acquisition and data analysis. In most of the reported CRD experiments the accuracy of τ is of the order of a per cent, which is due to multimode excitation of the ring-down cavity. The sensitivity of CRD spectroscopy can thus be increased by single-mode excitation of the cavity.

In summary, CRD spectroscopy offers a sensitivity of 10^{-6} - 10^{-9} cm^{-1} with a rather simple experimental set-up. The sensitivity can be increased by exciting a single longitudinal mode. This single-mode approach is experimentally more involved than the 'normal' (i.e. multimode) CRD approach, which is due to the locking and simultaneously scanning of the laser and the ring-down cavity.

2.4 Continuous-wave cavity ring down

The intrinsic bandwidth of a pulsed laser not only limits the spectral resolution but also complicates the data analysis due to the possibility of mode beating and nonexponential decay. Another limitation of pulsed lasers is the repetition rates thus fast data acquisition continuous-wave cavity ring down (cw-CRD) can eliminate this limitation.

The first cw-CRD experiments were performed with a cw-dye laser [19, 20], but these were soon replaced by cheaper, smaller, and ‘turn-key’, single mode diode lasers [21, 22]. Decay can be recorded if the cw laser beam is rapidly interrupted when a certain intensity level of the leaking out of cavity is reached. The spectral resolution of a typical cw diode laser is 2 orders of magnitude higher than the resolution of a pulsed laser with typical bandwidth of 1.5 GHz (0.05 cm^{-1}). The narrow bandwidth of a diode laser also enables the excitation of a single resonator mode; then the mode beating and nonexponential decay are avoided.

Mode matching a cw laser with (TEM_{00}) cavity modes can increase the efficiency with which the light is coupled into the resonator. The intensity of the light leaking out of the cavity is thus increased, which simplifies the detection of the decay transient and reduces the shot noise. This can be achieved by locking the CRD cavity to the laser: cavity locked cw-CRD (CLCW-CRD) [23]. State of the art CLCW-CRD setups achieve repetition rates of 80 kHz, a resolution of 75 kHz, and use analog detection schemes to determine the decay rate [24]; the sensitivity of the method is better than 10^{-11} cm^{-1} . Closely related to CLCW-CRD technique is noise-immune cavity enhanced optical heterodyne molecular spectroscopy [25] with an even higher sensitivity; discussion of this technique however is beyond the scope of this thesis.

Although the achievements of cw-CRD are impressive, there are also some drawbacks. Diode laser often have a limited scan range compared to pulsed laser. To record spectra multiple short scans of $\approx 3 \text{ cm}^{-1}$ would be required, where a single scan of a pulsed dye laser is sufficient. A diode laser can cover the frequency range of 400 cm^{-1} , but controlled single mode scans are only possible over a limited frequency range. Pulsed dye laser system can cover the frequency range $11000\text{-}20000 \text{ cm}^{-1}$. The

development of all solid state narrow bandwidth optical parametric oscillators extends the wavelength range of pulsed systems. Not only is the scan range of a diode laser limited, more important is that they are not yet available at every desired wavelength. cw-CRD lacks the simplicity of pulsed-CRD because it requires delicate electronics and optical devices. Nevertheless cw-CRD remains a very powerful and sensitive technique.

2.4.1 Sensitivity

Exciting a single longitudinal mode of the ring-down cavity provides the best sensitivity, just as in pulsed CRD spectroscopy. By locking the cavity to the laser line, the energy build-up in the cavity is high, which results in a high intensity on the detector that records the ring-down transient, thus improving the signal-to-noise ratio. With a locked cavity consisting of three mirrors with a reflectivity $R=0.9993$, [23] a sensitivity of $5 \times 10^{-9} \text{ cm}^{-1}$ is achieved. Although the repetition rate could in principle be more than 10 kHz, the actual repetition rate was only a few hundred hertz, limited by the acquisition speed of the digitizing electronics. Furthermore, the sensitivity of this spectrometer was limited by electronic noise imposed by the detection electronics (e.g. the digitizer). Recently, this set-up has been improved by using an analogue detection scheme [24]. With this improved CRD spectrometer, a sensitivity of $8.8 \times 10^{-12} \text{ cm}^{-1} \text{ Hz}^{-1/2}$ was achieved for the detection of carbon dioxide at around 1064 nm. The cavity round-trip path was 42 cm, and the ring-down time of the empty cavity was 2.8 μs . The switching speed of the AOM, used for turning the laser beam on and off, was 80 kHz. Mirrors of modest reflectivity were used in order to obtain not too low intensities on the detector.

Van Zee *et al.* (1999) compared, very generally, the sensitivities which can be obtained with single-mode pulsed and cw-CRD spectroscopy. Their conclusion is that, in principle, the highest sensitivity can be obtained when a cw laser with a very narrow bandwidth is used. This is mainly due to the more efficient coupling of light into the cavity. Obviously, a real comparison between pulsed and cw-CRD spectroscopy is very difficult since detailed knowledge is needed of all components of the spectrometer.

2.4.2 Applications

CW-CRD spectroscopy is suitable for ultrahigh-resolution spectroscopy of molecules and clusters in supersonic expansion. In general, jet spectra are much simpler to interpret than spectra recorded in a cell, because of the reduced Doppler width of the rovibrational transitions and the reduced number of spectral lines as a result of rotational and vibrational cooling. Hippler and Quack [30] recorded the jet-cooled spectrum of the $\nu_2+2\nu_3$ combination band of methane, and Biennier [31] recorded the rotationally resolved spectrum of the electronic transition of the O₂ dimer.

An additional advantage of cw-CRD spectroscopy is the high intracavity power which can be achieved, which offers the possibility of studying nonlinear effects [26, 27]. Romanini [26] recorded the absorption spectrum of NO₂ in a jet, using a 2 W single-mode titanium-doped sapphire laser. The power in their ring-down cavity was about 20 W, which allowed them to observe saturation effects such as decreased absorption and Lamb dips. It should be noted, however, that such nonlinear effects have also been observed with pulsed CRD spectroscopy [28, 29].

Furthermore, cw-CRD spectroscopy can also be used for trace gas detection. For example, Campargue [32] demonstrated the sensitive detection of SiH₂ in argon-silane discharge. In this context, the development of compact and low-cost diode lasers is important. Since only one (or a few) rovibrational transitions of a trace gas molecule need to be monitored, the limited spectral region in which a single diode laser operates is not a disadvantage. For example, with a multiplexed diode laser system consisting of two diode lasers operating at 1391 and 1402 nm, Totschnig [33] could measure, simultaneously, methanol and isopropanol in a cell with a sensitivity of $2.4 \times 10^{-9} \text{ cm}^{-1}$ for a 4.3 s averaging time.

References:

- [1] H. B. Babcock, G. Herzberg, *Astroph. J.* **108**, (1948), 167
- [2] J. W. Brault, *J. Mol. Spectr.* **80**, (1980), 384
- [3] J. U. White, *J. Opt. Soc. Am.* **66**, (1976), 411
- [4] D. Herriot, *Appl. Opt.* **3**, (1964), 523
- [5] W. Demtröder, *Laser spectroscopy*, Springer Verlag, Berlin, (1996)
- [6] H. Naus, A. de Lange, W. Ubachs, *Phys. Rev. A* **56**, (1997), 4755
- [7] P. Zalicki, R. N. Zare, *J. Chem. Phys.* **102**, (1995), 2708
- [8] R. T. Jongma, M.G.H. Boogaarts, I. Holleman, G. Meijer, *Rev. Sci. Instr.* **66**, (1995), 2821
- [9] J. T. Hodges, J. P. Looney, R. D. van Zee, *Appl. Opt.* **35**, (1996), 4112
- [10] G. Meijer, M. G. H. Boogaarts, R. T. Jongma, D. H. Parker, A. M. Wodtke, *Chem. Phys. Lett.*, **217**, (1994), 112.
- [11] R. Engeln, G. Meijer, *Rev. Scient. Instrum.*, **67**, (1996), 2708
- [12] P. Zalicki, Y. Ma, R. N. Zare, E. H. Wahl, J. R. Dadamio, T. G. Owano, C. H. Kruger, *Chem. Phys. Lett.*, **234**, (1995), 269.
- [13] M. Zhao, E. H. Wahl, T. G. Owano, C. C. Largent, R. N. Zare, C. H. Kruger, *Chem. Phys. Lett.*, **318**, (2000), 555.
- [14] R. D. Van Zee, J. T. Hodges, J. P. Looney, *Appl. Optics*, **38**, (1999), 3951.
- [15] P. Zalicki, R. N. Zare, *J. Chem. Phys.*, **102**, (1995), 2708.
- [16] J. Martin, B. A. Paldus, P. Zalicki, E. H. Wahl, T. G. Owano, J. S. Harris, Jr, C. H. Kruger, R. N. Zare, *Chem. Phys. Lett.*, **258**, (1996), 63.
- [17] K. K. Lehmann, D. Romanini, *J. Chem. Phys.*, **105**, (1996), 263.
- [18] J. J. Scherer, J. B. Paul, A O'Keefe, R. J. Saykally, *Chem. Rev.* **25** (1995), 149
- [19] R. Engeln, G. Meijer, *Chem. Phys. Lett.* **262**, (1996), 105
- [20] D. Romanini, A. A. Kachanov, N. Sadeghi, F. Stokel, *Chem. Phys. Lett.* **264**, (1997), 316
- [21] D. Romanini, A. A. Kachanov, N. Sadeghi, F. Stokel, *Chem. Phys. Lett.* **270**, (1997), 538
- [22] B. A. Paluds, C. C. Harb, T. G. Spence, J. Xie, J.S. Harris, and R. N. Zare, *J. Appl. Phys.* **82**, (1997), 3199

- [23] B. A. Paluds, C. C. Harb, T. G. Spence, J. Xie, J.S. Harris, and R. N. Zare, J. Appl. Phys. **83**, (1998), 3991
- [24] T. G. Spence, C. C. Harb, B. A. Paldus, R. N. Zare, B. Willke, R. L. Byer, Rev. Sci. Instr. **71**, (2000), 347
- [25] L. Gianfrani, R. W. Fox, L. Hollberg, J. Opt. Soc. Am. B **16**, (1999), 2247
- [26] D. Romanini, P. Dupre, R. Jost, Vibr. Spectrosc., **19**, (1999), 93.
- [27] C. R. Bucher, K. K. Lehmann, D. F. Plusquellic, G. T. Fraser, Appl. Optics, **39**, (2000), 3154.
- [28] L. Lehr, P. Hering, IEEE J. quant. Electron., 33, 1465 ; 1997b, Appl. Phys. B, **65**, (1997), 595.
- [29] I. Labazan, S. Rudic, S. Milosevic, Chem. Phys. Lett., **320**, (2000), 613.
- [30] M. Hippler, M. Quack, Chem. Phys. Lett., **314**, (1999), 273.
- [31] L. Biennier D. Romanini, A. Kachanov, A. Campargue, B. Bussery-Honvault, R. Bacis, J. Chem. Phys., **112**, (2000) 6309.
- [32] A. Campargue, D. Romanini, N. Sadeghi, J. Phys. D, **31**, (1998), 1168
- [33] G. Totschnig, D. S. Baer, J. Wang, F. Winter, H. Hofbauer, R. K. Hanson, Appl. Optics, **8**, (2000), 2009

Chapter 3 Development of cw-CRD spectrometer

3.1 CW-CRD spectrometer with a pulsed planar plasma expansion

3.1.1 Abstract¹

A new cw cavity ring down spectrometer has been constructed with the aim to record electronic spectra of rotationally cold carbon chain radicals at high spectral resolution in direct absorption. The radicals are generated by discharging a high pressure gas pulse of acetylene in He in a multilayer slit nozzle geometry. A passive cavity mode locking scheme is used to handle refractive index changes inside the cavity caused by gas pulse and plasma fluctuations. The performance is demonstrated with the rotationally resolved origin band spectrum of the $\tilde{A}^2\Pi_g \leftarrow \tilde{X}^2\Pi_u$ electronic transition of the triacetylene cation, HC_6H^+ , around 16654.7 cm^{-1} .

3.1.2 Introduction

The general description of cavity ring down spectroscopy (CRD) experimental setup is presented in Ref. [24]. In Fig. 3.1 an overview of the update version of the apparatus is shown. Detailed drawings and description of the construction and operation of the transient molecule source, laser and computer system are presented in this chapter.

¹ This Chapter is a slightly modified from the article published in: P. Birza, T. Motylewski, D. Khoroshev, A. Chirokolava, H. Linnartz, J.P. Maier, Chem. Phys. 283 (2002) 119.

High resolution spectra of unsaturated carbon chain radicals are of interest in view of their role in interstellar hydrocarbon chemistry. Following Fourier transform microwave work, a series of cyanopolyynes and (cyano)poly-acetylenes has been identified by radio astronomy in dark interstellar clouds [1]. It is argued that electronic transitions of such chains may be responsible for unidentified absorption features in diffuse interstellar clouds [2]. The first experimental indication of this came from observations of the electronic absorption spectra of mass-selected carbon species in neon matrices [3], but owing to solvation effects, the absorption bands exhibit a shift relative to the corresponding gas phase spectra.

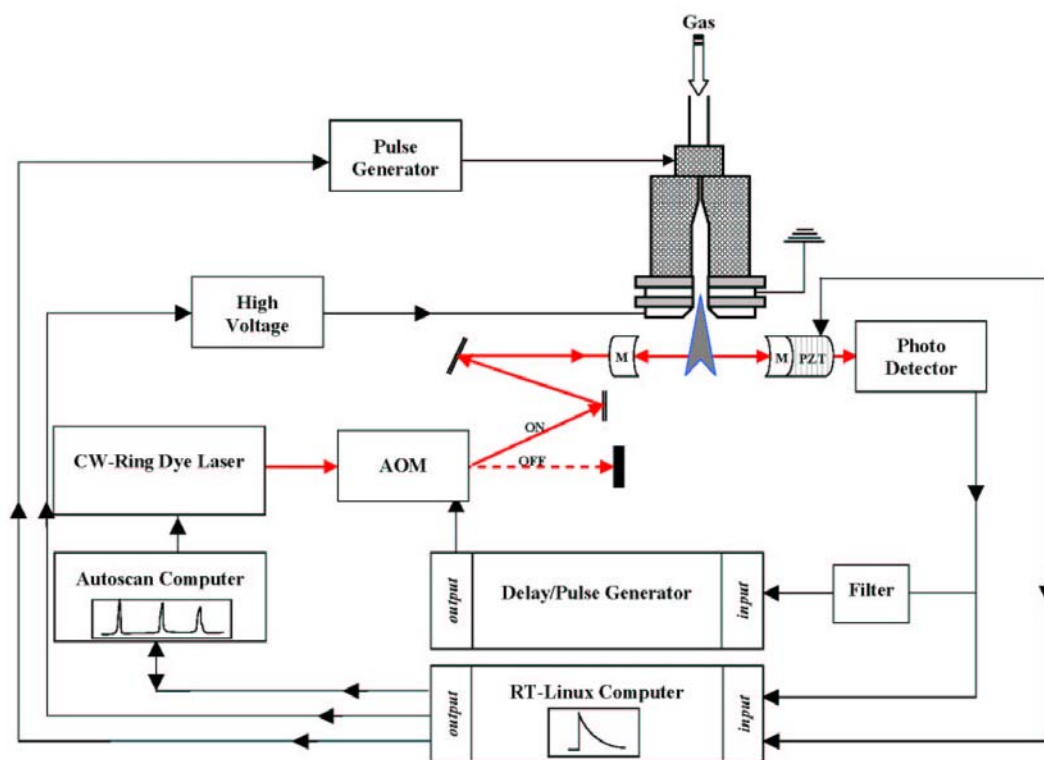


Figure 3.1 Overview of cw-CRD experiment.

The latter are now available from a series of experiments on supersonic plasma expansions, using photo-detachment [4], REMPI-TOF [5], and CRD [6,7] spectroscopy with pulsed laser systems. The frequency resolution in these experiments is typically of the order of 0.035 cm^{-1} or worse. In a single-mode cw laser experiment a much higher resolution can be obtained and with this aim a cw-CRD setup has been constructed.

CRD spectroscopy has become a powerful tool for the study of the structural and dynamical properties of molecules in the gas phase. In a series of recent review articles [8–10] a number of useful applications is listed. One of the reasons for this success is the conceptual simplicity of a CRD experiment [11]. That is, the ring down time reflects the rate of absorption rather than its magnitude and as such it is independent of power fluctuations. In addition, very long absorption path lengths are obtained by confining light tens of microseconds to the cavity. This increases the sensitivity considerably and absorption values as small as 10^{-6} per pass have been achieved.

In conventional CRD experiments, pulsed lasers are used; each light pulse induces a ring down event. In cw experiments this is not the case and more complicated detection schemes must be applied, either by measuring the phase retardation of an amplitude modulated cw laser [12] or by analyzing the exponential decay after switching off the laser beam with a fast optical switch [13–18]. In addition, the cavity has to be in resonance with the laser wavelength, because the laser bandwidth is generally too narrow to excite more than one cavity mode at a time. For this reason several active tracking schemes have been developed [14, 15, 17], but in a pulsed jet experiment - as it is the case here – such schemes do not work: the gas pulse changes the refraction index, effectively changing the optical length of the cavity, pushing it out of resonance. This effect is further enhanced when plasma fluctuations cause additional instabilities. In this case a passive scheme for mode locking must be used, as it was introduced recently in Refs. [16, 18].

In this contribution the experimental details are described of a cw-CRD setup capable of detecting unstable carbon chains generated in a pulsed supersonic planar plasma expansion. The performance is discussed on the example of a rotationally resolved electronic spectrum of the triacetylene cation, HC_6H^+ .

3.1.3 Mechanism of cw-CRD spectrometer

The carbon chain radicals are generally produced by applying a 500 μs high voltage pulse (- 600 V, 100 mA) to a 1 ms high pressure gas pulse of an 0.5 % HCCH/He mixture that is expanded through a $3\text{cm} \times 200\mu\text{m}$ slit with a backing

pressure of approximately 10 bar. The system has been used before (see e.g. Refs. [19, 20]) and combines high molecular densities and relatively large absorption path lengths with an effective adiabatical cooling. In addition, the effective resolution is increased compared to pinhole expansions due to a reduced Doppler broadening parallel to the slit. A further reduction is obtained by using a multichannel body. A 3D picture of the nozzle is shown in Fig. 3.2 together with a short description of its operation. More details are

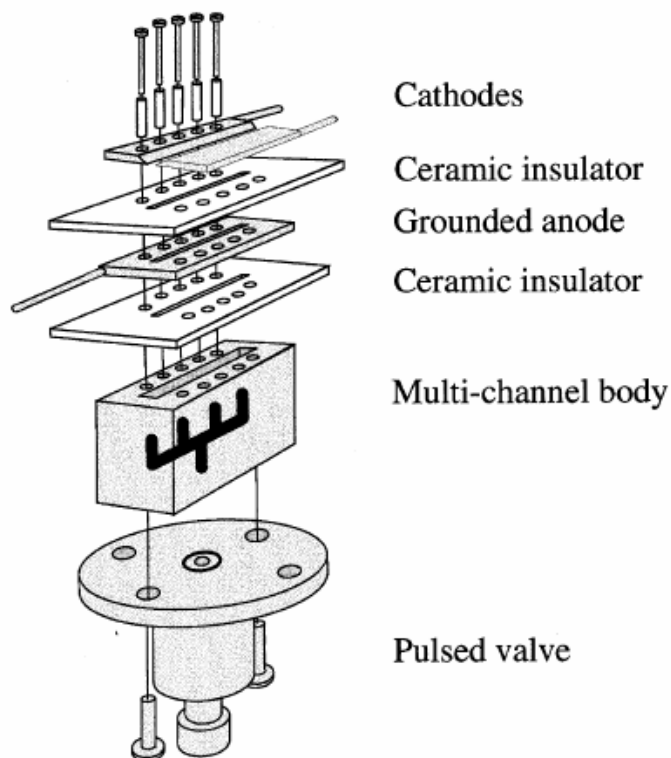


Figure 3.2 An artist's view of the high pressure slit nozzle discharge. The orifice consists of two sharp stainless steel jaws (actual slit), a ceramic insulator, a slotted metal plate (grounded) and a second ceramic insulator. Both insulators and metal parts are mounted to the body of the nozzle using electrically isolated screws. A pulsed negative high voltage is applied to the jaws via ballast resistors at the moment that a high pressure gas pulse expands through the channel. The discharge strikes to the grounded plate, localizing the reaction zone to a region upstream of the expansion. The body is floating and connected to an electromagnetic driven pulsed valve. A multichannel system inside the nozzle regulates the gas flow towards the slit and allows a further reduction of the Doppler broadening.

available from Ref. [21]. Fig. 3.3 shows the whole experimental setup. The light of a single mode ring dye laser (Coherent, cw-899 autoscan), pumped by a 6 W solid state laser (Verdi), is guided through an acousto-optical modulator (AOM, Isomet 1205C-2). The first order detection is focused into the ring down cavity via a lens that matches a TEM_{00} cavity mode, where it crosses the planar plasma expansion

approximately 6 mm downstream. The cavity ring down mirrors (REO, 1 m plano/convex, $R > 99.995\%$) are mounted in a mechanically stable holder at a distance of $L = 32$ cm. A system of internal diaphragms facilitates a careful alignment and He-curtains protect the mirrors from pollution during jet operation.

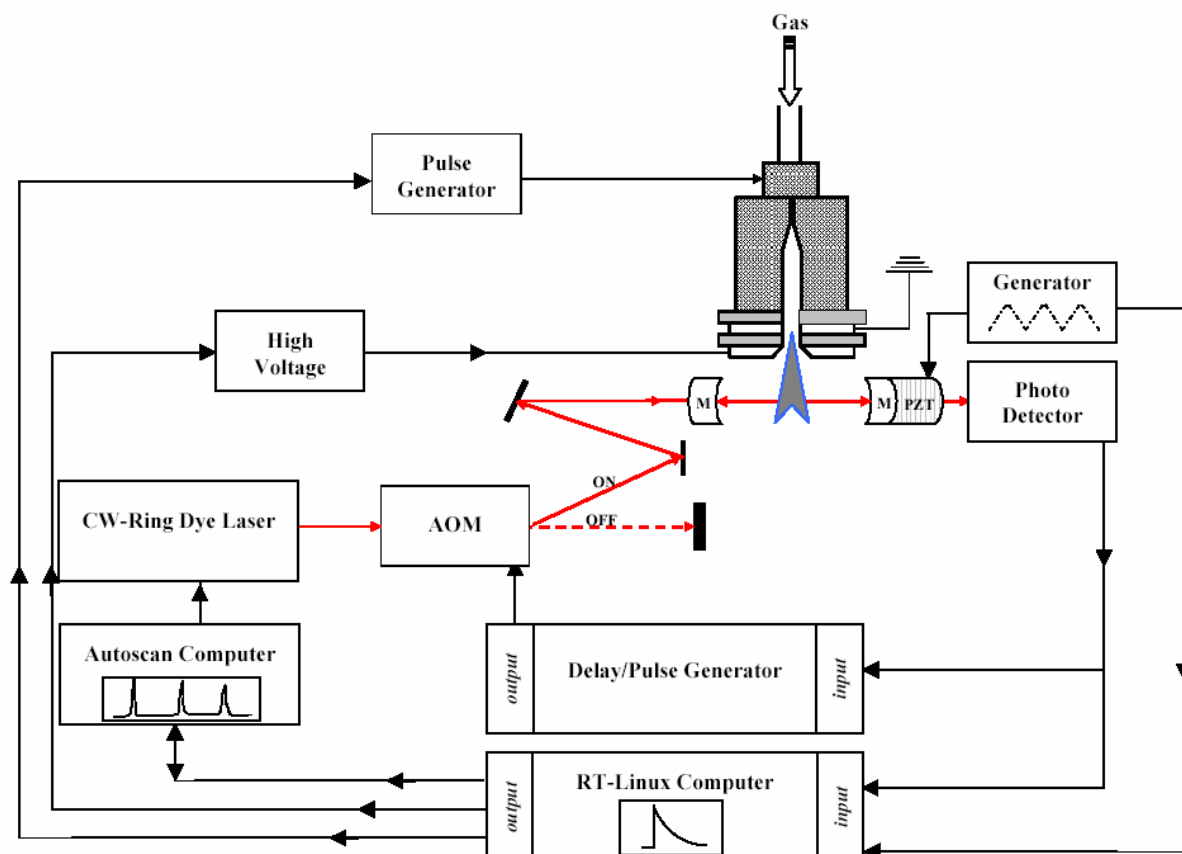


Figure 3.3 Schematic of the whole experimental setup using an external generator for the ramp

A strong transmission occurs only when cavity and laser wavelength are mode matched. To achieve this, a passive mode locking system has been used, similar to the method described in Ref. [16, 18]. One of the mirrors is mounted on a piezo element (PI S314.10) and by applying a periodical (30 Hz) triangular shaped voltage to the element the cavity length is modulated. The amplitude is chosen in such a way that it corresponds to at least two free spectral ranges of the laser frequency, *i.e.* the cavity is at least four times in resonance with the laser during one period (Fig. 3.4). A resonance results in a maximum of transmitted light intensity after the cavity and is monitored using an oscilloscope. When the intensity reaches a certain threshold, a trigger signal is generated that switches off the AOM; the laser beam is interrupted and a ring down event is initiated.

The following detection scheme is used to guarantee that plasma pulse and ring down event coincide (Fig. 3.4). The data acquisition program chooses via a simple algorithm for the transmission that is strongest and closest to the middle of the

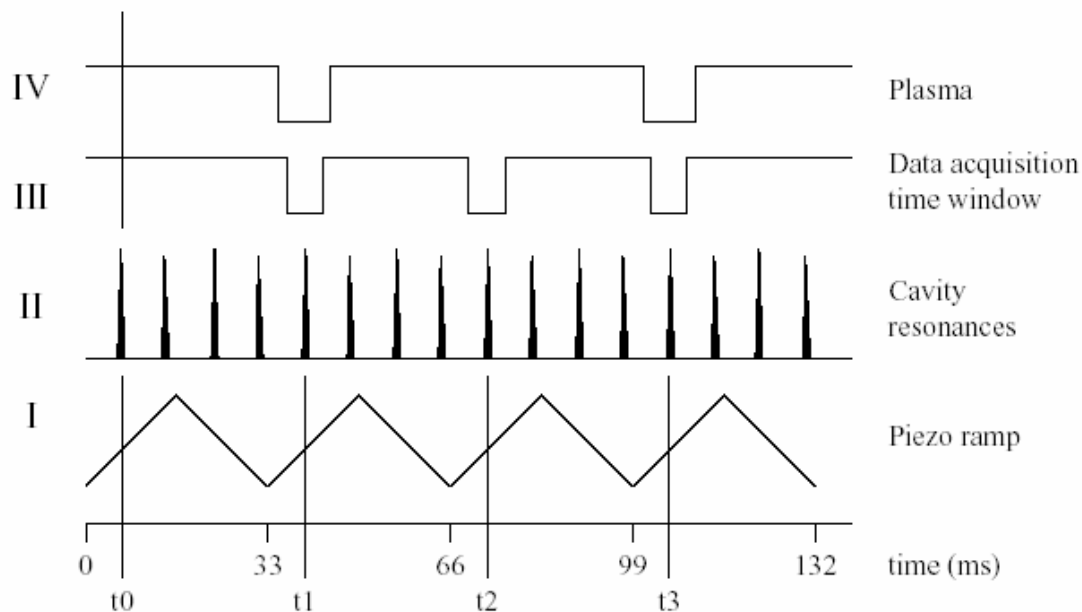


Figure 3.4 Timing and triggering scheme. I. A 30 Hz ramp is applied to a piezo element. II. The photo diode shows when cavity resonances occur. The data-acquisition program chooses the transmission closest to the middle of the ramp, defining t_0 and the ramp voltage for which the resonance occurs. When the transmission intensity exceeds a certain threshold, the AOM is switched off and a ring down event is induced. III. The program defines a 300 μ s time window in which the next resonance is expected. In order to circumvent hysteresis effects only signals on positive or negative ramps are taken. IV. t_0 is also used 11 to trigger the gas and discharge pulse every second ramp. The plasma free ring down event is used for background subtraction. Further details are given in the text.

ramp voltage. This defines t_0 . The exact ramp voltage ($V_{1,res}$) at which this cavity resonance occurs is used to define a 300 μ s time window at the same ramp voltage in the next cycle. (In order to minimize hysteresis effects of the piezo-element, only transmissions on positive or negative ramps are used.) It also defines a delay at which gas and discharge pulse are activated, in such a way that the plasma expansion coincides with the time window: when a ring down event occurs it automatically samples the plasma. To further increase the sensitivity, only every second cycle is used to trigger gas and discharge pulse. The plasma free ring down event is then used for background subtraction. This means that with a 30 Hz periodic modulation, 15 ring down events with plasma and 15 ring down events without plasma are measured.

The major part of the predicted resonances is within the $300 \mu\text{s}$ time window, but due to external instabilities the procedure might fail. In this case the data acquisition program checks the whole ramp, defines a new t_0 and restarts predicting the position of the next resonance. During this short time (3 cycles) only a few data points are lost. The transmission after the ring-down cavity is focussed via a narrow band pass filter onto a broad band UV/VIS Si-photodiode (Hamamatsu, ST336-44BQ). Ring down events are recorded using home-written software running under real-time Linux. The complete decay curve is fitted to an exponential defining τ . The CRD spectrum is obtained by recording τ while scanning the laser. Typical ring down times amount to $\tau = 27 \mu\text{s}$. This is equivalent with approximately 25000 passes through the plasma or an effective plasma absorption pathlength of 760 m.

3.2 Slit nozzle plasma

The spectroscopy of ions and radicals in a cooled discharge cell suffers from high rotational and vibrational temperatures and Doppler limited resolution. Due to high temperatures, the spectra are congested and fine and hyperfine splitting are hard to be seen because of Doppler broadening. Higher temperatures in the cells decrease the quantum state population density and consequently the detection sensitivity is greatly reduced.

Free jet expansions combined with plasma techniques overcome such problems. A number of discharges techniques have been applied to nozzles both with circular and slit geometries. The first design in this direction was introduced by Egelking with a corona discharge in a expansion through a pine hole [25]. A small gauge tungsten wire is introduced through a 'T' fitting attached to the glass tube, and positioned with one end just behind the nozzle aperture on the high-pressure side. When this side is connecting at high voltage (typically 15kV through stabilizing resistors limiting the current to 50 μ A), a small corona discharge forms at the tip of the tungsten wire. The current flows through the gas in the nozzle throat, making connection to the ground by ionic and electronic conduction over the expansion to a grounded plate.

A new pulsed, discharge slit source was developed by Nestbitt et. al. generating intense jet-cooled densities of radicals and molecular ions [26]. The design confines the discharge region upstream of the supersonic expansion orifice to achieve an efficient rotational cooling down to 30 K or less. The basic discharge design consists of two electrically stainless steel jaws that form the limiting aperture for the 4 cm slit expansion, separated from the pulsed valve body by a thin isolator. A negative bias voltage is applied to both jaws. The electron current therefore flows across the insulator against the supersonic gas stream and terminates on the inside of the pulsed valve. Gating circuits are used to switch the discharge voltage to the jaws on and off 50 μ s before and after the gas pulse arrives. The discharge is essentially completely confined inside the 300 μ m wide slit. Molecular radical densities of 10^{12} / cm^3 and protonated ions densities of 10^{10} / cm^3 have been obtained with this source.

Our construction is similar to a slit nozzle incorporating discharge zone, which was used to measure high-resolution infrared spectra of methyl and ethyl radicals [54, 55] using methanol and ethyl iodine as precursors. The source body consists of a slit insulator, a metal plate, a second insulator and two sharp plates that form the exit slit ($\sim 250 \mu\text{m}$, 60° exit angle).

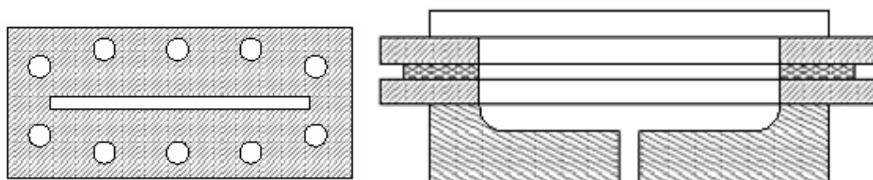


Figure 3.5 High pressure slit nozzle discharge

To have a high gas peak pressure and eliminate waste of precursor substances we use a version of nozzle with internal volume 1 cm^3 (see fig. 3.5) and a gas buffer (600 cm^3) before the valve to avoid pressure drop during the pulse (Fig. 3.1). This resulted in shorter expansion times ($500\text{-}1000 \mu\text{s}$) and stable gas pulses.

Unfortunately, the nozzle has one disadvantage. The gas coming out the circular opening has to expand first horizontally to fill the internal volume and then vertically through the slit. The horizontal speed component is partially preserved while the gas passes through the slit. This results in a non-homogeneous expansion and causes Doppler broadening and even splitting of observed spectral lines. The splitting can be as large as 0.06 cm^{-1} when He is used as carrier gas, which corresponds to a relative velocity of 900 m/s . To make the gas flow less divergent in the direction parallel to the slit and to the laser beam a wide slit in a bottom ceramic plate was substituted with a series of cylindrical holes (1 mm hole, 0.3 mm ceramic walls in between, see fig. 3.6).

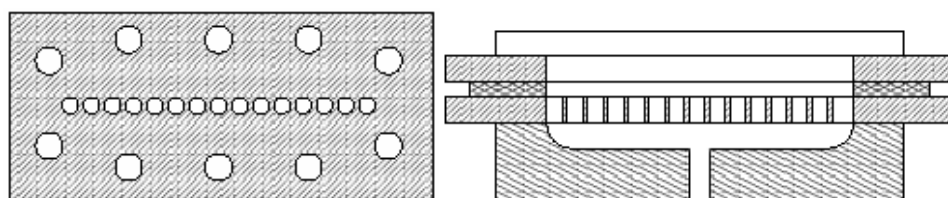


Figure 3.6 Slit nozzles with a series of cylindrical holes

This design Fig. 3.2 resulted in significantly reduced Doppler broadening. Nevertheless, to reduce more the Doppler broadening we built a new body with a

multi channel system (Fig.3.3) inside the nozzle to regulates the gas flow towards the slit and allows a further reduction of Doppler broadening.

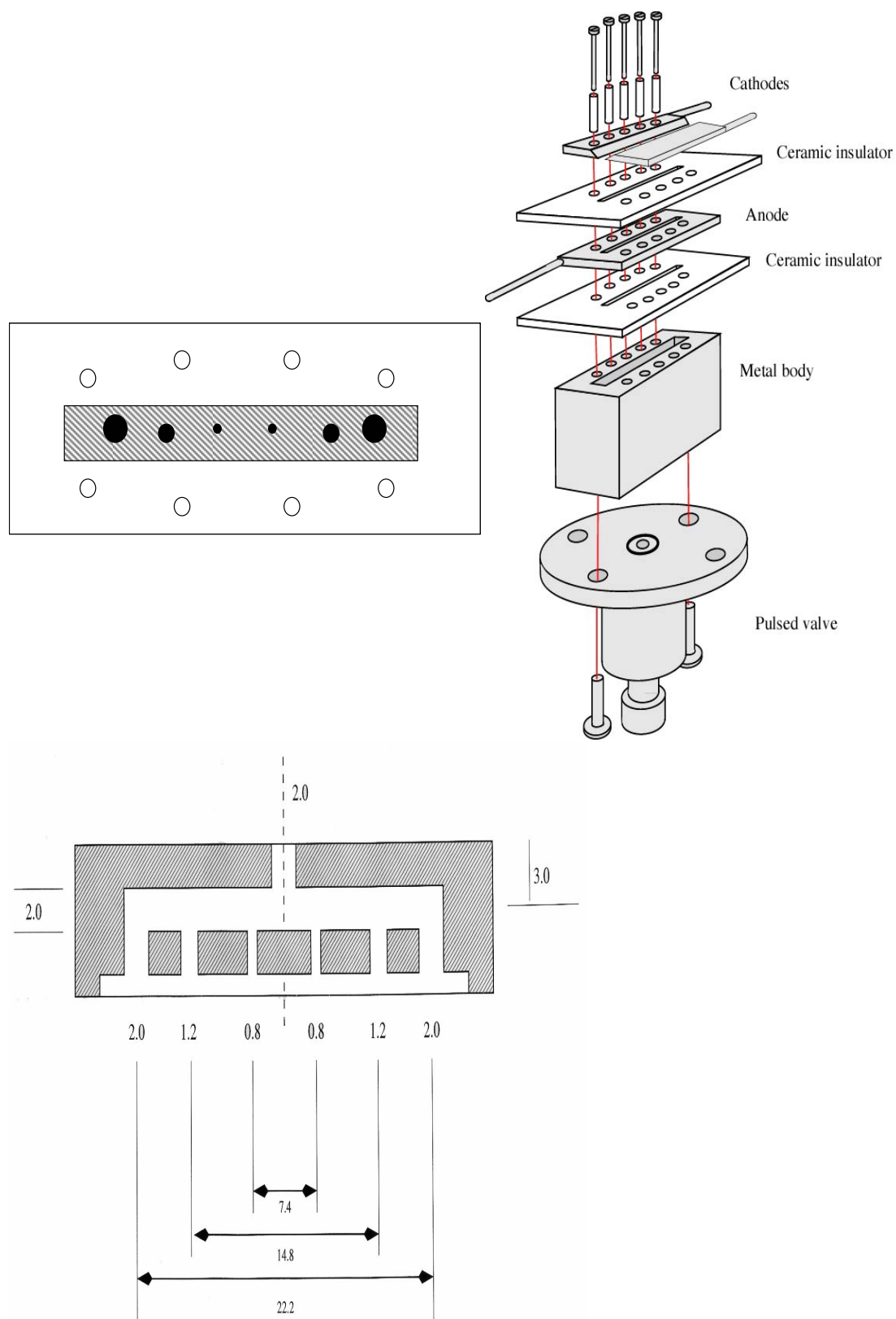


Figure 3.7 High pressure slit nozzle discharge with new multi channel body

3.3 Acousto-optic modulator, cavity and light detector

3.3.1 The Acoustic-Optic Modulator (AOM)

One of the most important components of the experiment is the acoustic optical modulator (AOM). The laser beam is guided through the AOM and the first order deflection is focused into the ring down cavity via a telescope that matches a TEM₀₀ cavity mode. When the transmission intensity exceeds a certain threshold, a trigger signal is generated than switched off the AOM, the laser beam is interrupted and a ring down event is initiated. The principle of the operation can be briefly described as follows.

The acousto-optic effect occurs when a light beam passes through a transparent material, such as glass, in which traveling acoustic waves are also present, as depicted in Fig. 3.8. Acoustic waves are generated in the glass by a piezoelectric transducer that is driven by a RF signal source. The spatially periodic density variations in the glass corresponding to compressions and rarefactions of the traveling acoustic wave are accompanied by corresponding changes in the index of refraction for propagation of light in the medium. These traveling waves of index of refraction variation diffract the incident light much as the atomic planes of a crystal diffract x-rays in Bragg scattering. For acoustic waves of sufficiently high power, most of the light incident on the acousto-optic modulator can be diffracted and therefore deflected from its incident direction.

For acoustic waves of frequency f traveling at the speed of sound in a medium, v_s , the wavelength of the acoustic waves, Λ , and therefore the spacing between the planes of index of refraction variation, is given by the usual wave relation $v_s = \Lambda f$. A light beam passing through the acoustically driven medium will be diffracted to angles θ given by:

$$\sin \theta = (m\lambda / 2\Lambda) \quad (1)$$

where $m = 0, \pm 1, \pm 2$, is called the diffraction order. In this experiment only the $m = +1$ diffraction order will be important. Note the similarity of Eq. (1) to the analogous formula for Bragg diffraction of x-rays by atomic planes separated by a distance d :

$$\sin \theta = (m\lambda / 2d)$$

From Fig. 1, the angle α between a diffracted beam and the undiffracted beam is given by:

$$\sin(\alpha/2) = (m\lambda / 2\Lambda) = (m\lambda f / 2vs) \quad (2)$$

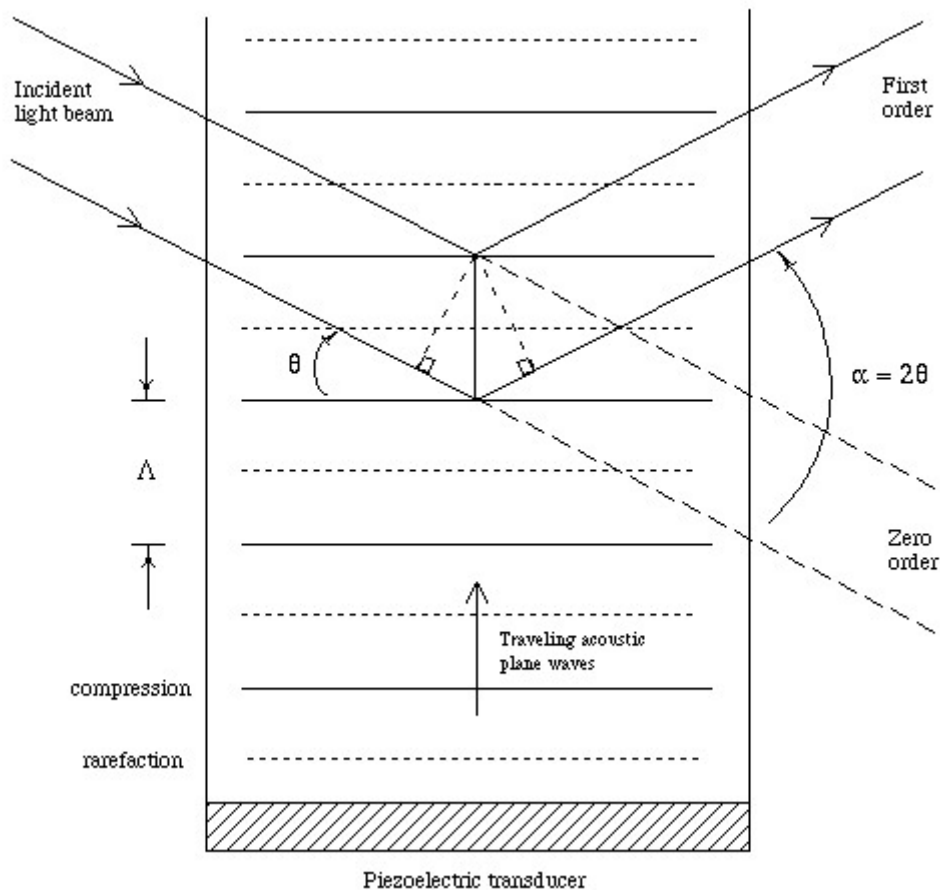


Figure 3.8 Diffraction of a light beam by traveling acoustic plane waves in a acousto-optic modulator.

3.3.2 Cavity

The high finesse optical cavity is the most characteristic element of the CRD experiment. It is formed by two plano-concave (PL-CC) dielectric mirrors facing each other. The reflectivity coefficient of the mirrors used in this experiment is in the range from 99.98-99.995%. Such high reflectivity could not be achieved using metal mirrors. The other advantage of the dielectric mirrors is very low absorption – the light which is not reflected, passes through the mirror. ($T=1-R$).

The cavity ring down mirrors (REO, 1 m plano/convex, $R > 99.995\%$) are mounted in a mechanically stable holder at a distance of $L=32$ cm Fig 3.9. A system of internal diaphragms facilitates a careful alignment and He-curtains protect the mirrors from pollution during jet operation.

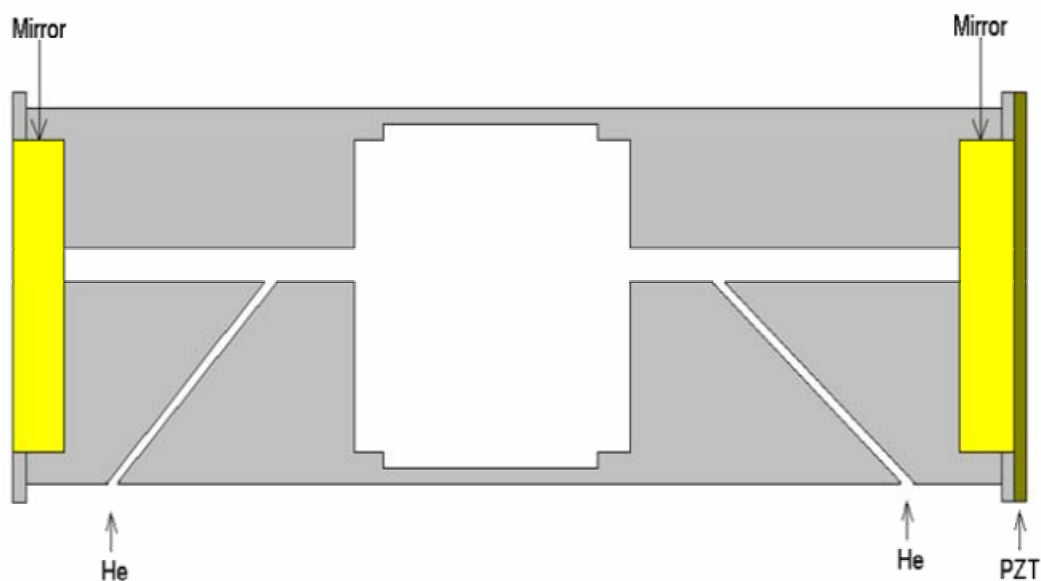


Figure 3.9 Schematic description of the cavity

3.3.3 PZT

One of the keys of this experiment is the PZT (piezoelectric translators), because by applying a periodical triangular shaped voltage to the element the cavity length is modulated. The amplitude is chosen in such a way that it corresponds to at least two free spectral ranges of the laser frequency, *i.e.* the cavity is at least four times in resonance with the laser during one period.

Two main types of piezo actuators are available: low-voltage (multilayer) devices requiring 100 volts or less for full motion and high-voltage devices requiring about 1000 volts for full extension. Modern piezo ceramics capable of greater motion replace the natural material used by the Curies, in both types of devices. Lead zirconate titanate (PZT) based ceramic materials are most often used today. Actuators made of this ceramic are often referred to as PZT actuators.

The maximum electrical field PZT ceramics can withstand is on the order of 1 to 2 kV/mm. In order to keep the operating voltage within practical limits, PZT actuators consist of thin layers of electro active ceramic material electrically connected in parallel (Fig. 3.10). The total displacement is the sum of the displacements of the individual layers. The thickness of the individual layer determines the maximum operating voltage for the PZT.

High-voltage piezo actuators consist of bulk ceramic disks which are 0.4 to 1 mm thick and glued together to form a stack (for more details see appendix 1).

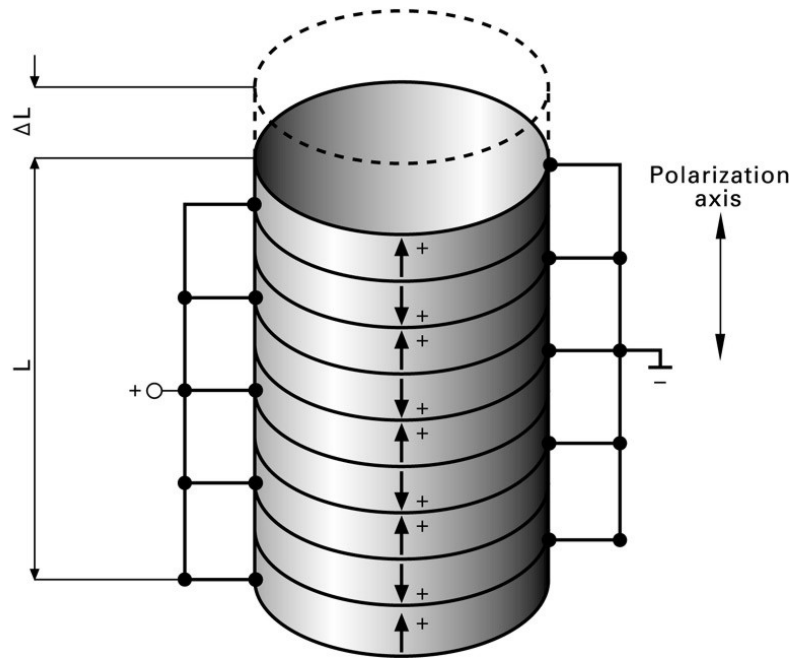


Figure 3.10 Electrical connection of disks in a PZT stack actuator.

3.3.4 Light detector

The light it was detected by a broad band UV-VIS-NIR Si photodiode. A fast, low noise LM6365N amplifier was applied (Fig 3.11). The photodiode amplifier circuit combines fast response (bandwidth 10 MHz), minimal noise and linear DC operation. The photodiode voltage is amplified 250 times which results in a signal up to 5 V recorded by the data card. It should be noted that LM6365N amplifier is not a conventional operational amplifier. It is stable only for gains higher than 25 and has input impedance of about 10 K Ω which matches well the 1.5 K Ω load required for a fast photodiode response. The circuit is supplied with stabilized ± 15 V.

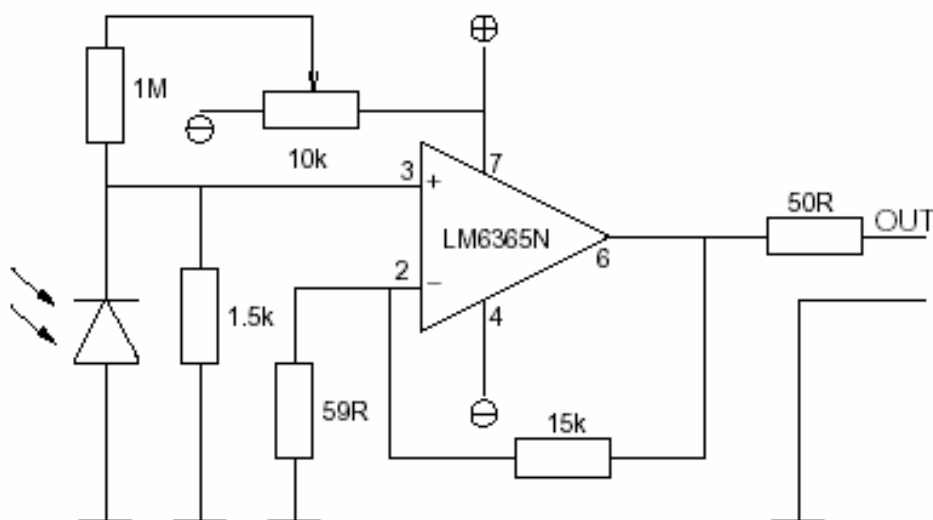


Figure 3.11 Photodiode amplifier circuit

To reduce the noise we use a simple RC filter between the delay generator and the data card.

3.4 Continuous wave laser setup

The range of applications for continuous wave tunable lasers has expanded steadily since the introduction of the world's most widely used ring laser in 1979—Coherent's 699 Ring Dye Laser. Advances in ring laser technology, particularly the development of laser-quality titanium-doped sapphire, have made wider tunability and outstanding performance in the near-infrared, with the convenience of a solid-state gain medium, possible. Today, increasing demands on research time and budgets, as well as performance, call for a ring laser system that is versatile and easy to operate, as well as capable of high power and tunability. The new 899 Ring Laser is designed for quick set-up and optimization with both dye and titanium: sapphire gain media. The 899 Ring Laser operates reliably over extended periods in every type of application, from routine semiconductor analysis to laser cooling of atoms. The 899 is the most flexible and economical ring laser system available, with the widest range of modular and upgradeable configurations, including full computer control.

899-29 AUTOSCAN II

The AUTOSCAN II combines an 899-21, a personal computer, a wavelength meter, analog-to-digital conversion capabilities, and a powerful software package to create a unique spectroscopic tool. Features include automatic selection of wavelengths (with absolute accuracy of ± 200 MHz and reproducibility of ± 50 MHz), automatic data acquisition of scans of any length permitted by the laser gain medium, a macro language, and extensive interfacing and customization capabilities.

899 Broadband Operation

High performance, stability, and ease of operation—in any configuration—require a carefully designed, optimized resonator. Because the 899 Ring Laser was designed as an upgradeable system, the basic resonator for broadband operation fulfills the most demanding requirements of stabilized, single-frequency operation in titanium: sapphire and dye. All optical components, including the dye jet and

titanium: sapphire crystal assemblies are mounted on a two-inch diameter, low-thermal expansion Invar rod. This extremely rigid, high thermal mass structure reduces system sensitivity to vibration and temperature changes.

System

Titanium-doped sapphire is a solid-state gain medium with superior laser performance from approximately 680 nm to 1.1 μm . The 899 Ring Laser is the only laser to offer the high output power and exceptional convenience of titanium: sapphire (Ti:S), together with the flexibility, visible and UV performance of dyes. This combination provides continuous tunability from 370 nm in the UV (or lower with frequency doubling) to approximately 1.1 μm in the IR (Figure 3.12).

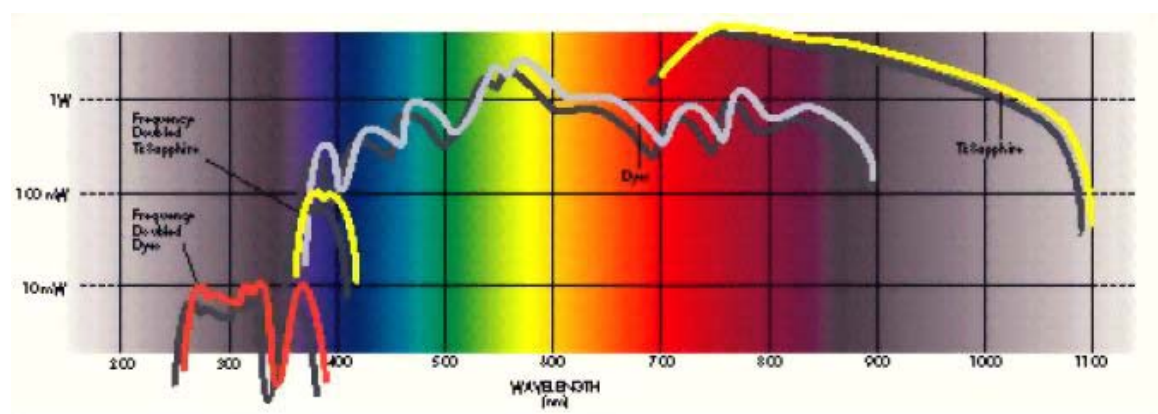


Figure 3.12 Ring laser tuning curves

The relative ease of alignment of a CW laser depends critically upon the pumping geometry. This is especially true of Ti:S configurations, which require collinear pumping. The lateral and angular positions of the pump beam, as well as the position of the pump beam waist, must precisely match that of the resonator. The 899 Ring Laser has separate, orthogonal controls for angular, lateral, and waist positions of the pump beam to provide faster, more consistent alignment.

The Ring Laser optical mount is fitted with a stable orthogonal control. Precision translation stages and high-resolution wedge-drive angular adjustments are used throughout for smooth, hysteresis-free motion. The range and sensitivity of each control are optimized for fast, consistent alignment.

The dye-jet assembly is equipped with high-resolution orthogonal adjustments for precise, repeatable positioning. The precision-formed, hardened stainless-steel dye jet produces an interferometrically-flat laminar stream for stable, low-noise operation. Some of the available tuning ranges and configurations are listed in table 3.1.

<i>Ring Dye configuration</i>	Rhodamine 6G	560-620 nm
	Kiton Red	600-650 nm
	DCM	630-700 nm
<i>Titan-Sapphire configuration</i>	Short Wave	700-830 nm
	Mid Wave	790-910 nm
	Long Wave	900-1000 nm

Table 3.1 Available tuning ranges and configurations for the ring laser system

The ability to change the mirror focal lengths of the 899 resonator adds a degree of flexibility found in no other cw laser system. Optimal resonator spot sizes for maximum power extraction and best mode depend on pump power and gain. Threshold and efficiency are determined, in large part, by ratio of the spot sizes of the resonator beam waist and pump beam waist. The 899's variable focus resonator provides convenient optimization of the laser for a range of pump powers. In the Ti:S configuration, two fold mirrors and the final pump mirror are mounted on translation stages, while the dye configurations have the pump mirror mounted on translation stages. These adjustments allow the resonator to be refocused and to accommodate cavity mirrors of varying focal lengths. This variable focus resonator thus delivers high efficiency from lower gain dyes or lower power pump lasers, and maximum output in high power configurations (for more details see appendix 2).

3.5 Controlling experimental conditions

There are several parameters of the laser system and the source which need to be stabilized in order to obtain good quality spectra. One difficult parameter to control is the gas pressure in the slit during the absorption measurement. The intensity of the gas pulse is changing in time, due to slow deformation of the valve poppet as well as possible rotation of the valve elements, while the length of electrical pulse opening the valve is kept constant. Variable gas amount leads to different conditions in the plasma and thus variations in the ring-down time. The average pressure in the vacuum chamber is related to the amount of gas in a single pulse, and consequently stabilizing this pressure will stabilize the effective backing pressure. This is achieved by measuring continuously the pressure in the vacuum chamber (crdst program) and changing the opening time of the valve by a monitoring program shm.tcl running on pc-104crd computer. A simple PID control algorithm is used.

The potential applied to electrodes is controlled by setting an HV pulse amplitude on a IGBT HV pulse generator (1500 V / 1 Amps). Resistors of 2.2 k Ω are used to limit the maximum current. The main source of instability is a short circuit in the slit (graphite deposition) which result in a temporarily lower voltage between the electrodes and sparking. This can be avoided by careful cleaning and by not using too high pressures and voltages in Ne or Ar expansion. A He expansion is more stable, when the backing pressure equals 8–11 bar and acetylene concentration does not exceed 0.5% the discharge is stable for many hours even at -1200 V.

The quality of the measured spectrum depends on the relative delays of the valve opening, discharge and the probing laser beam. To achieve highest possible concentration of molecules, the measurement is done at the top of the gas pulse, which comes 900-1600 μ s after the electric pulse opening the valve. The discharge is set to fire about 100-200 μ s before the laser and to continue at least until the end of the ring down. In this way the least possible amount of gas is used and measurements are performed during nearly stationary expansion conditions.

A number of improvements to our previous setup (12) have been made.

(1)-before, several signals (photodetector, pressure gauges, voltage applied to the piezo) were recorded by the same data acquisition card, which switched between different channels. The switching resulted in spikes in the ring-down signal. Now two data acquisition cards are used, one for the ring-down signal (see Fig 3.13), the other for

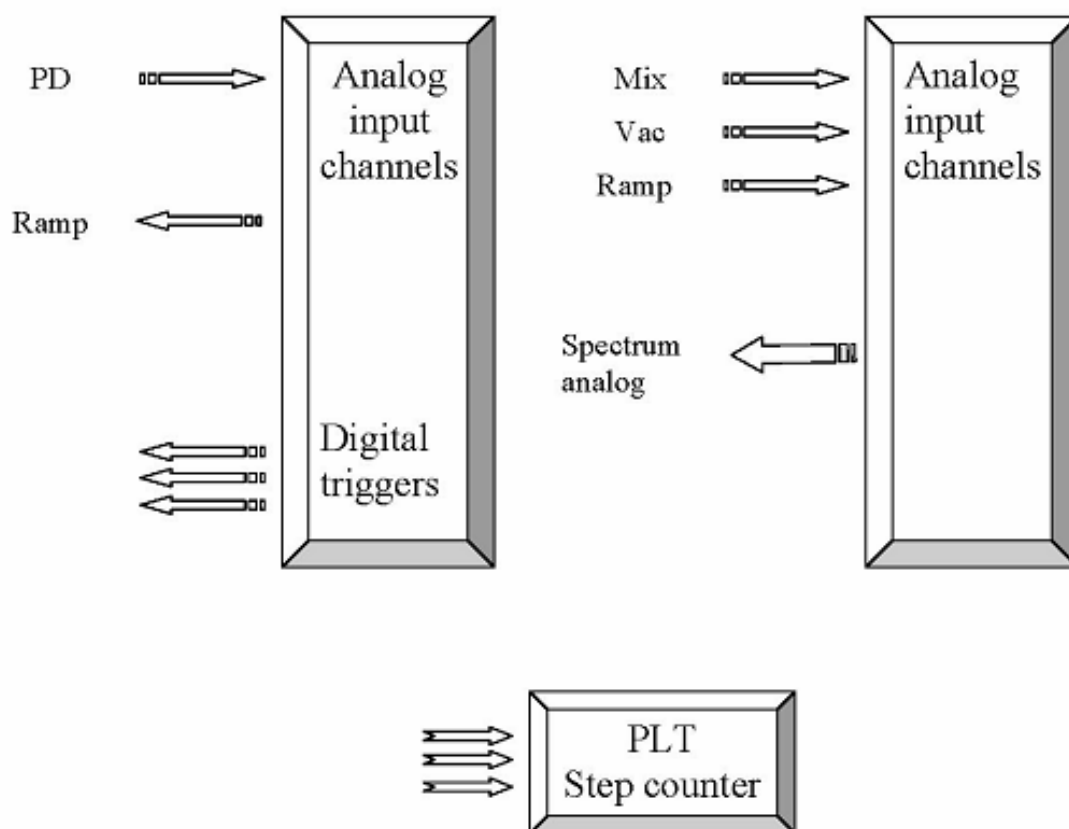


Figure 3.13 Data card acquisition system. One is used to control the analog channels and to send analog spectrum to the autoscan computer via network and the second one just to receive the data from the photodiode (small spikes) and to generate the ramp voltage. By this means the noise coming from the valves can be avoided

all other signals, so there are no spikes.

(2) The algorithm for triggering the gas and HV pulses has been changed. The delays for activating the valve and discharge are measured from the first resonance on the ascending voltage ramp (Fig. 3.14),

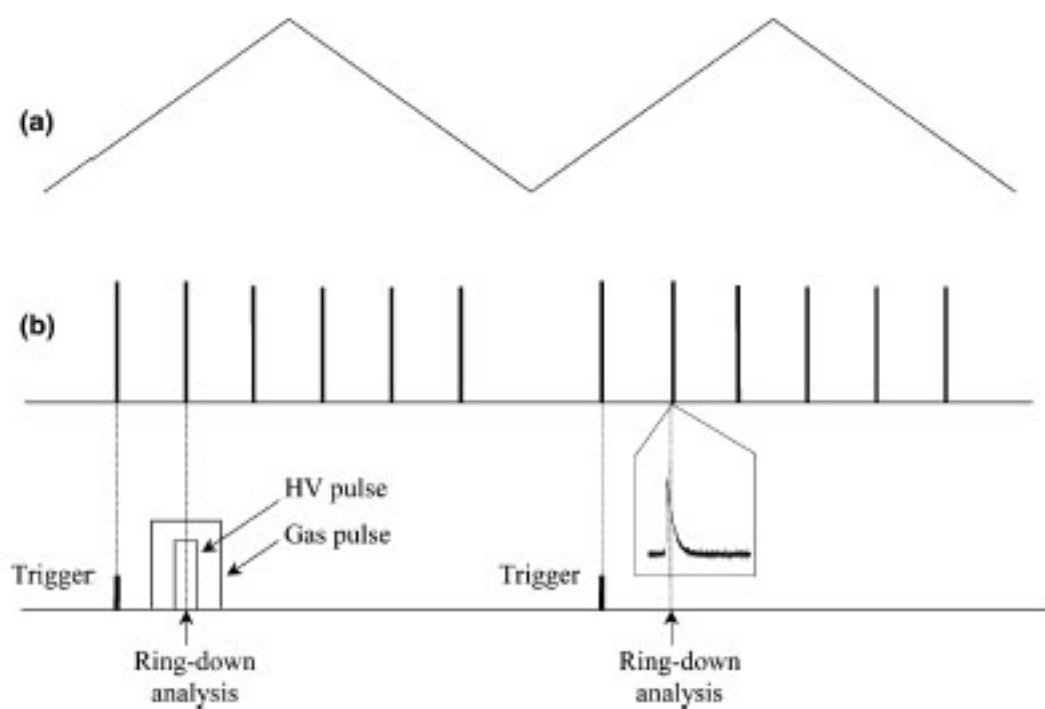


Figure 3.14. Relative timing of the piezo ramp voltage, cavity resonances, valve opening, and high voltage pulse applied to the slit electrodes. (a) Ramp voltage applied to the piezo. (b) Signal on the photodetector

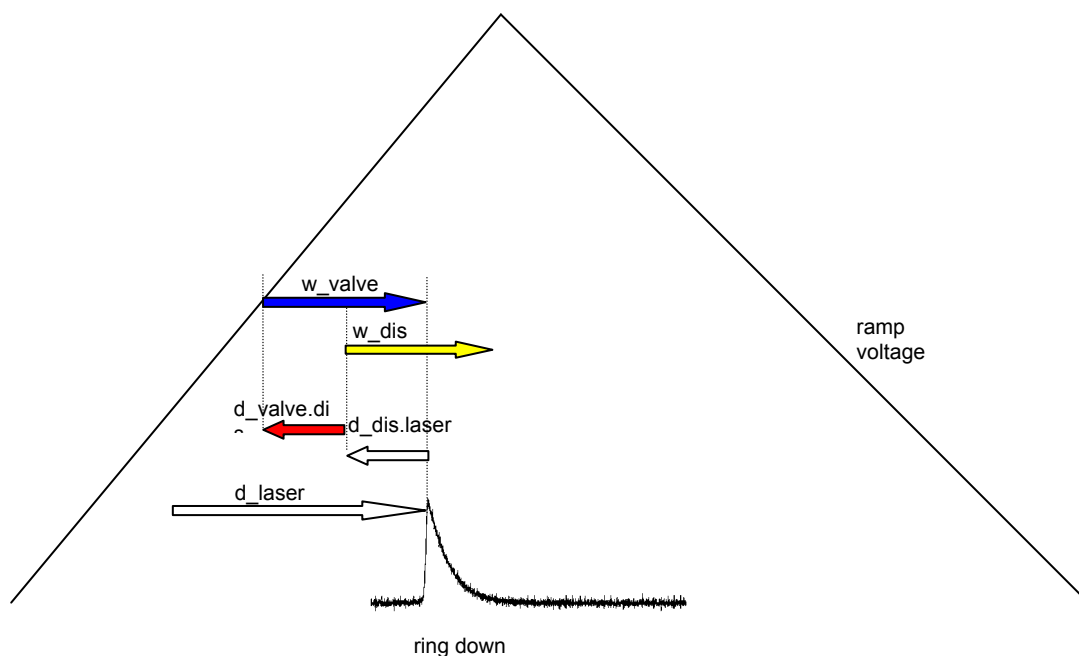


Figure 3.15 Parameters used to control delays. The labels on the arrows are the parameters used in the data acquisition program and correspond to the next parameters from the shm.tcl panel: d_laser – laser delay, d_dis_laser – discharge –

laser delay, w_{dis} – discharge length, d_{valve_dis} – valve discharge delay, w_{valve} – valve opening rather than from the analysed ring-down in the last period of the triangular-wave voltage. This algorithm is more robust and allows for larger steps in the laser scan. Non-linear response of the piezo element to the applied voltage results in slightly different delays between the first and second resonances depending on their positions with respect to the voltage ramp (see figure 3.16).

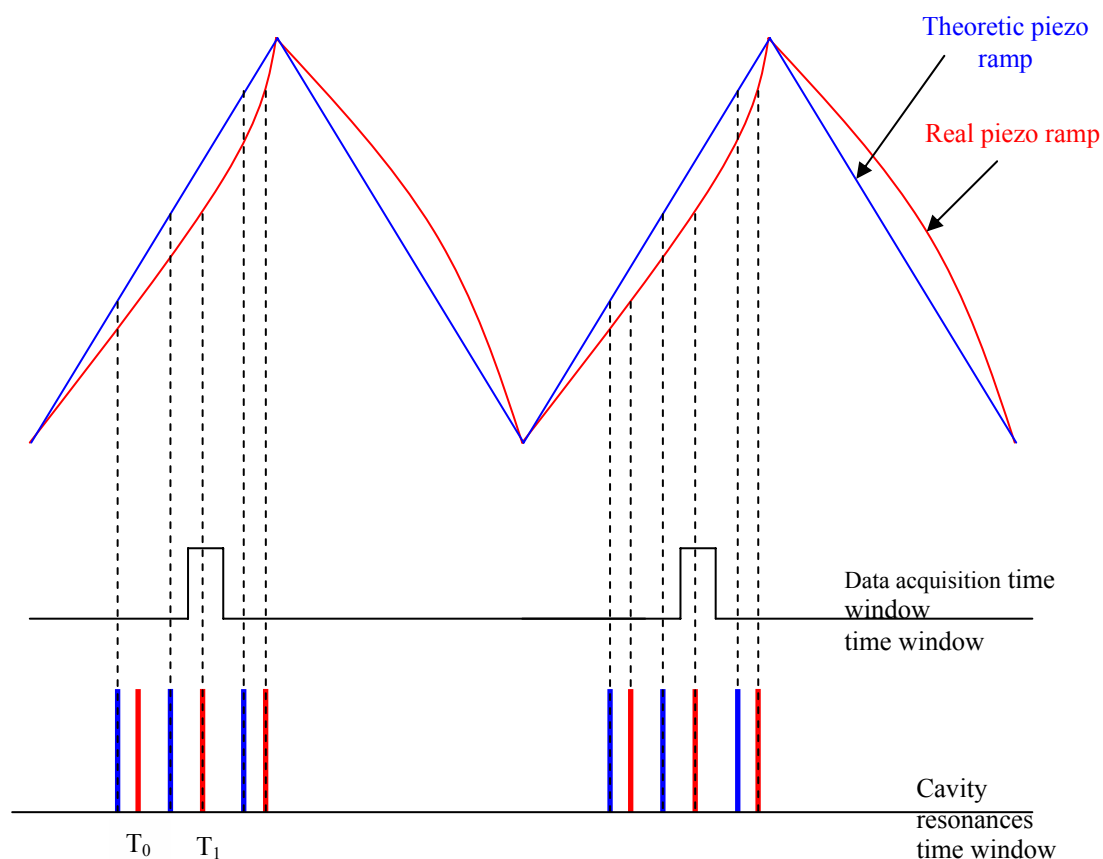


Figure 3.16 Nonlinearity of the piezo element

This leads to the changes in relative timing of the HV pulse and the ring-down event as the laser is scanned and the resonances move relative to the ramp. To preserve this relative timing, the delay between the first resonance and the HV pulse is adjusted taking into account piezo nonlinearity. (3) The triangular-wave voltage for the piezo element is generated now by the data acquisition card instead of the stand-alone function generator. After all these changes, the signal-to-noise ratio improved 2.5 times. The achieved sensitivity was of order 10^{-7} - 10^{-8} cm^{-1} .

Trigger signals are generated by real-time Linux module `crdst-rt.o`. It is running on top of Linux kernel 2.2.19-rtl3.1-ext3-2. It allows to generate trigger pulses with accuracy of 1 μ s and to react to external signals with latency below 40 μ s. The communication of `crdst-rt.o` with other programs is done using shared memory (`mbuffer` version 0.7.2). Bulk data transfer is implemented using circular buffers written and read by National Instruments DAQ cards (PCI-MIO-16E-1 and PCI-6024E) using direct memory access (DMA).

The trigger adjustment is done by `shm.tcl` which uses the same shared memory to communicate with `crdst-rt.o`. `crd.tcl` adjusts finding ring downs, while `shm.tcl` adjusts the exact pulse sequence and timing. `shm.tcl` is also implementing temperature control (see Figure 3.17).

laser delay	1814
discharge-laser delay	-738
discharge length	516
valve-discharge delay	-139
valve opening	382.42796
set pressure	0.160
heater0 duty cycle	0.0
set temperature	80
heater1 duty cycle	0.0
set temperature	85
valve A	34
valve B	70
valve C	66
backing pressure	0.76
gas A ratio	0.4590
gas B ratio	0.0000
-3.987066 0.000000 300.269965 158116 60.030235 0	

Figure 3.17 User interface (`shm.tcl`) used for tuning `crdst-rt.o` RTLinux trigger generator.

The orange color marks the active signals, the signals marked green are disabled at a time . When the trigger is stopped, yellow indicates 'ready to use' and grey disabled. The 'EXIT' button quits only the shm.tcl application leaving the trigger running. The 'BREAK' button is an emergency switch and causes all the applications to stop and terminate. The small buttons on the right side of the 'valve opening ', switches the program to the manual control of the valve opening time, the some role is playing the small buttons on the side of the 'set temperature', switching the program to manual control of the heater.

3.6 Data acquisition

The software is split into three functional parts: data acquisition, laser (scan) control and the trigger (Fig. 3.18). The photodiode signal is measured (12 bit resolution) continuously with rate of 1.25 MS/sec. The data is transferred via DMA to 1Mb circular buffer. The current position of DMA pointer is monitored by `crdst-rt.o` and correlated with the high resolution system clock. The data acquisition runs synchronously with the ramp generator (both photodiode input and ramp output buffer cycle time is 400 ms). After the trigger sequence is finished, `main_loop` function (`rt_interp` thread of `crdst-rt.o`) searches for peaks higher than defines threshold. When found, CRD events are copied to the array for later processing by `crd-fitter`. The area where CRD events are expected is displayed by `crd.tcl` (Fig. 3.18).

`Crd.tcl` is a user interface to control some variables (Table 3.2) in the shared memory and to display some data from that memory block. It also reads the ring downs curves and displays them. The real control is done by `crdst.c` (compiled into `crdst-rt.o` real time kernel module) which accesses the same shared memory block.

Source	Program	Function
<code>crdst.c</code>	<code>crdst-rt.o</code>	real time control and measurement
<code>crd-fitter.c</code>	<code>crd-fitter</code>	fitting exponential decays, rejecting outliers, calculating averaged absorption, outputting absorption to <code>scan.tcl</code> and autoscan computer
<code>crd.tcl</code>	<code>crd.tcl</code>	control ramp frequency and amplitude, control detection thresholds, display CRD events
<code>shm.tcl</code>	<code>shm.tcl</code>	control trigger signals, stabilize pressure and temperature
<code>scan</code>	<code>scan</code>	record the spectra
<code>crd-watchdog.c</code>	<code>crd-watchdog</code>	supervise real time threads and stop the trigger if the system is overloaded
<code>libcrds-shm.c</code> <code>crds-shm.h</code> <code>crds-shm-config.h</code>	<code>libcrds-shm.so</code>	library with functions to access (“ <code>crdshm</code> ” command) shared memory control and status variables from tcl/tk language
<code>crds-shm.h</code> <code>crds-shm-config.h</code>		definition of data structures in shared memory

Table 3.2 Correspondence between source-program and function

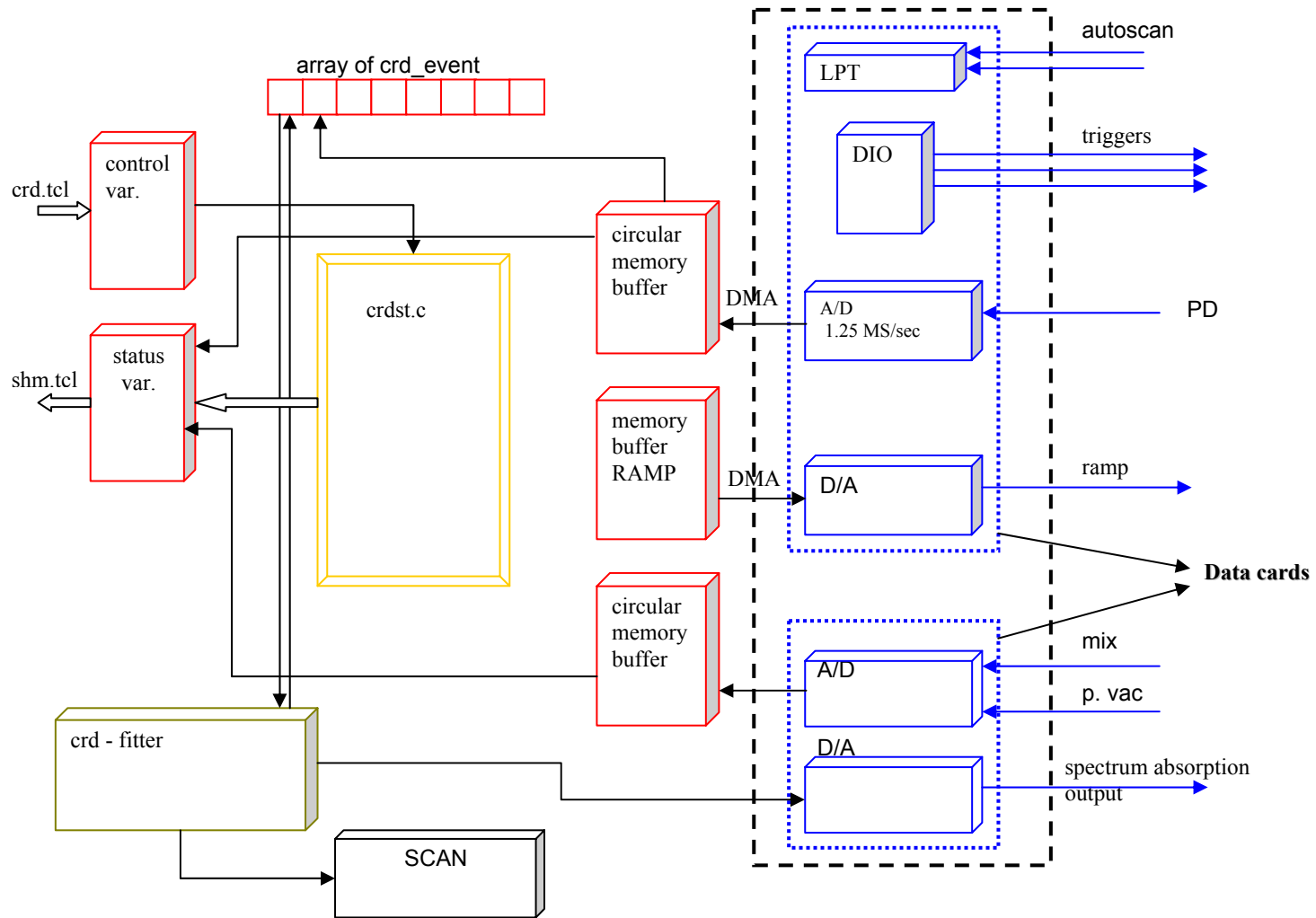


Figure 3.18 Data acquisition. DIO – Digital Input/Output, DMA – Direct Memory Access, crdst.c – multiple real time control threads

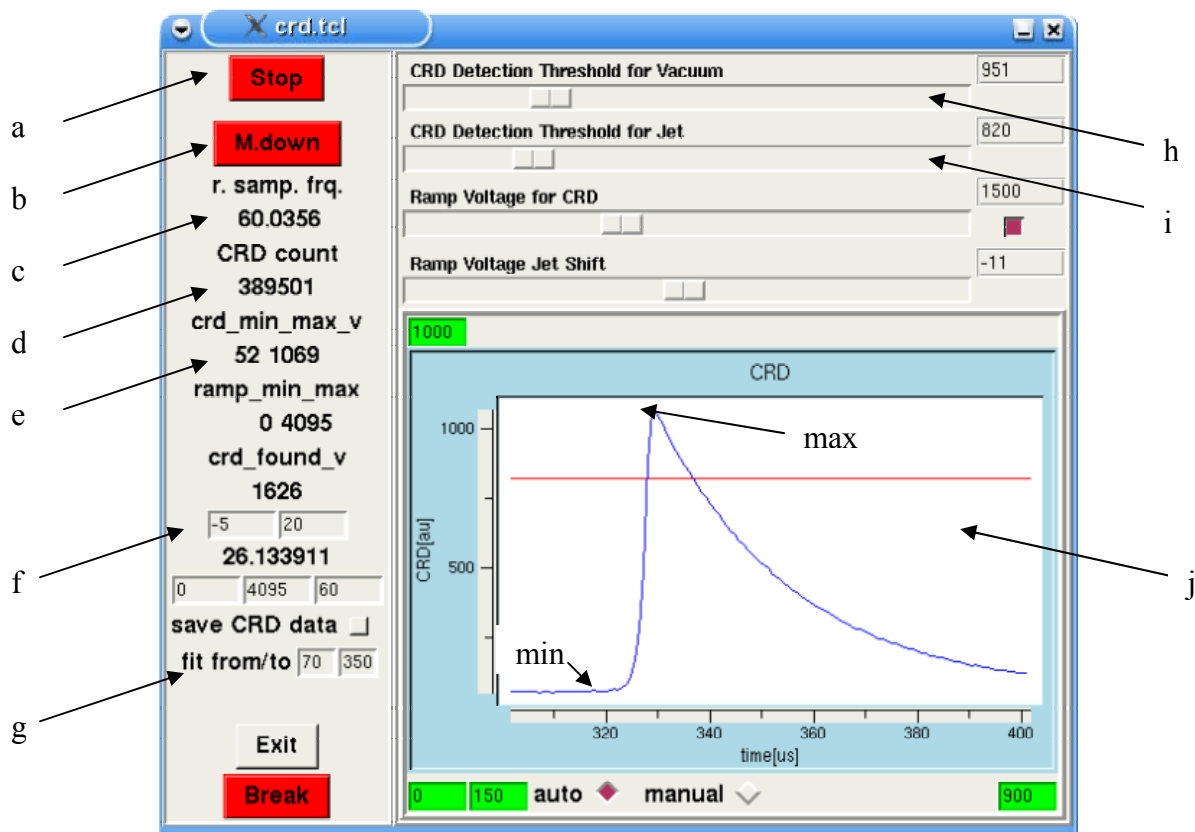


Figure 3.19 User interface (crd.tcl) used for tuning crdst-rt.o RTLinux trigger generator a – run/stop the program, b – measure the ring down on the ramp up or down, c – frequency of the ramp samples, d – counter of the ring downs, e – the minimum and maximum of the ring down, f – minimum and maximum absorption used for scaling analog absorption output, g – define the number of points to fit of samples to fit $b \cdot \exp(-a \cdot t) + c$ function, h – detection threshold for vacuum (blue), i – detection threshold for jet (red), j – ring down events

CRD events copied by crdst-rt.o are subsequently processed by crd-fitter process. It is fitting the 3 parameter function.

$$f(t) = A \exp(-Bt) + C$$

where: A – is amplitude, B – decay rate, C – offset.

The procedure is iterative and based on the fact that once the decay rate is fixed, amplitude and offset can be calculated fast using linear regression. In this way only single variable optimization using Brent method is needed [27]. The decay rate is calculated using this iterative method, while amplitude and offset come from linear regression.

Crd-fitter performs also several steps of data filtering (eliminating noisy measurements and outliers). CRD curve is rejected as too noisy when the ratio of

noise amplitude to the total signal is greater than 0.05. Results of the fit are accumulated in an array until the signal “next frequency” comes from Autoscan or until 100 events. CRD events are then evaluated inside of subsets marked by conditions during ring down (presence of JET, DISCHARGE). For each subset outliers (ring down time further than 1.5 standard deviation of the subset) are removed. Outlier removal is repeated 3 times. Typically 20% of all data points are discarded. In this way rare CRD distorted by *e.g.* strong sparking or wrong timing do not count against the final averaged absorption. The (possibly frequency and time dependant) cavity losses are compensated by subtracting the decay rate without the discharge from the decay rate with plasma present in the cavity. Final absorption is output in units of $(\text{ms})^{-1}$ and is sent together with the current wavelength step and segment count to the “scan” program (Fig. 3.20).

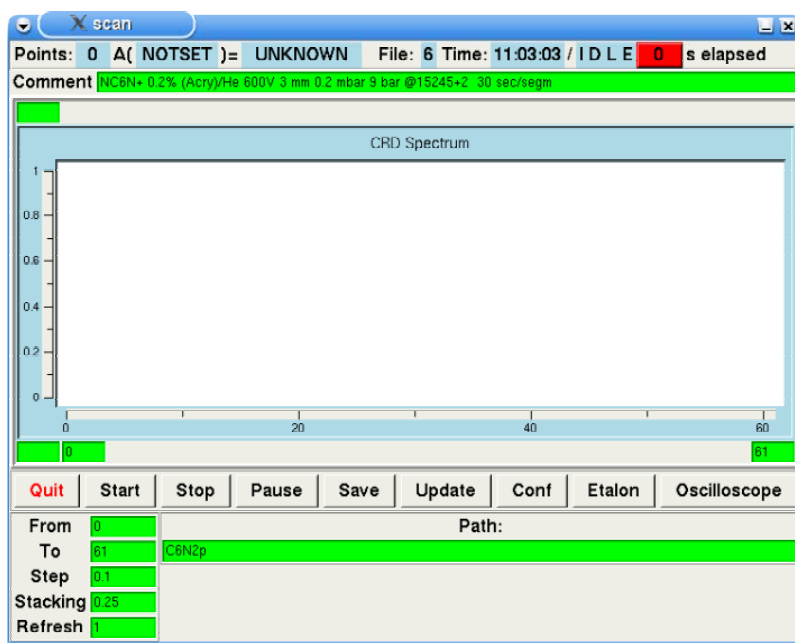


Figure 3.20 User interface (scan) used for recording spectra.

Then the data are plotted and saved to the disk² in a standard ASCII multicolumn TAB separated format. The first six lines contain extensive information about experimental conditions which should be entered by the operator before the scan finished.

² crd:/home/exp/data/YYYY/Month/datDDMMYY.NAME.NN

3.7 Results

In Fig. 2.5 the rotationally resolved origin band of the $\tilde{A}^2\Pi_g - \tilde{X}^2\Pi_u$ electronic transition of HC_6H^+ is shown. The same transition has been studied in detail before in a liquid N_2 cooled hollow-cathode discharge cell applying frequency-plasma double modulation (FPM) spectroscopy [22] and is shown for comparison in the inset of Fig. 3.16.

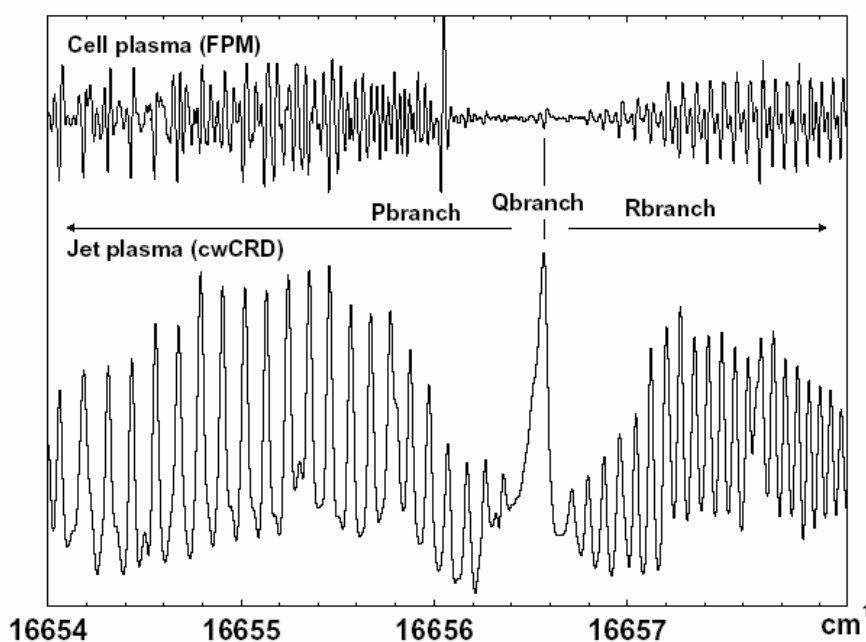


Figure 3.21 The origin band of the $\tilde{A}^2\Pi_g - \tilde{X}^2\Pi_u$ electronic spectrum of triacetylene cation, HC_6H^+ , measured by cw CRD spectroscopy through a supersonic pulsed planar plasma. The inset shows the corresponding spectrum measured in a ‘hot’, *i.e.* liquid N_2 cooled environment with $T_{\text{rot}} \approx 170$ K.

At the high ambient temperature in the cell (approximately 150-200 K) the band system is found to comprise of two partially overlapping, $\tilde{A}^2\Pi_{\frac{3}{2}} - \tilde{X}^2\Pi_{\frac{3}{2}}$ and $\tilde{A}^2\Pi_{\frac{1}{2}} - \tilde{X}^2\Pi_{\frac{1}{2}}$ subbands, separated by the difference in spin-orbit constants in ground and electronically excited state. Both subbands show strong *P*- and *R*-branches, with clear red shaded bandheads and with a weak *Q*-branch. The spectral simplification upon jet cooling is striking: the jet spectrum shown in Fig. 3.21

displays only one single band. It consists of a well-defined *P*- and *R*-branches and a strong *Q*-branch. The 6 lower *J*-levels are markedly stronger and no band head is observed. This is consistent with the low temperature in the supersonic jet. From the relative intensity of subsequent *J*-levels a rotational temperature of the order of 10 to 15 K is derived. The lower temperature favors the population of the low-*J* rotational levels and as the *Q*-line strength is highest for low *J*-values, thus the *Q*-branch is much more pronounced now. The spin-orbit splitting in the ground state is approximately -31 cm⁻¹ and as a consequence only the lower $\left(\Omega = \frac{3}{2}\right)$ spin-orbit component is observable. The best achievable linewidth (FWHM), using a multichannel body, amounts to 450 MHz, two to three times smaller than possible up to now in pulsed laser experiments. This is sufficient to obtain rotational resolution for chains with 10 to 11 carbon atoms, as long as no lifetime broadening is involved. However, 450 MHz is still larger than expected from the bandwidth of the cw laser system which is ≈ 50 MHz. Assuming a Doppler broadened signal, this corresponds to a translational temperature of the order of 125 K which is too high. Indeed, this is due to residual Doppler broadening in the slit expansion, as has been observed also before in frequency production modulation experiments [23]: the use of a slower expansion gas (for example Ar) reduces the achievable linewidth proportional to the speed ratios. Clearly, further modifications in the expansion source are necessary to take full advantage of the small bandwidth of the cw laser used here. A possible improvement might be the use of skimmed planar expansions but to our knowledge such systems have not been reported in literature yet. The signal-to-noise ratio obtained in the present experiment is comparable to that obtained in the previous FPM studies [20], but the cw CRD method is more generally applicable: it works both for very narrow and broad absorption features.

3.8 Conclusion

It has been shown that cw-CRD spectroscopy can be used to study rotationally cold carbon chain radicals that are produced in a pulsed plasma expansion. Passive

mode matching is sufficient to perform the experiments. A reduction in linewidth has been obtained. The limiting factor turns out to be residual Doppler broadening in the expansion along the slit. Future source improvements are necessary to further increase the achievable resolution

References

- [1] M.C. McCarthy, P. Thaddeus, *Chem. Soc. Rev.*, **30**, (2001), 177.
- [2] A.G.G.M. Tielens, T.P. Snow, Eds., *The diffuse interstellar bands*, Dordrecht (1995).
- [3] J.P. Maier, *J. Phys. Chem. A.*, **102**, (1998), 3462.
- [4] D.A. Kirkwood, M. Tulej, M.V. Pachkov, M. Schnaiter, F. Guthe, M. Grutter, M. Wyss, J.P. Maier, G. Fischer, *J. Chem. Phys.* **111**, (1999), 9280
- [5] T. Pino, H.B. Ding, F. Guthe, J.P. Maier, *J. Chem. Phys.* **114** (2001), 2208.
- [6] T. Motylewski, H. Linnartz, O. Vaizert, J.P. Maier, G.A. Galazutdinov, F.A. Musaev, J. Krelowski, G.A.H. Walker, D.A. Bohlender, *Astrophys. J.* **531**, (2000), 312.
- [7] C.D. Ball, M.C. McCarthy, P. Thaddeus, *J. Chem. Phys.* **112**, (2000), 10149.
- [8] J.J. Scherer, P.B. Paul, A. O'Keefe, R.J. Saykally, *Chem. Rev.* **97**, (1997), 25.
- [9] M.D. Wheeler, S.M. Newman, A.J. Orr-Ewing, M.N.R. Ashold, *J. Chem. Soc. Faraday T.*, **94**, (1998), 337.
- [10] G. Berden, R. Peeters, G. Meijer, *Int. Rev. Phys. Chem.*, **19**, (2000), 565.
- [11] A. O'Keefe, D.A.G. Deacon, *Rev. Sci. Instrum.*, **59**, (1988), 2544.
- [12] R. Engeln, G. von Helden, G. Berden, G. Meijer, *Chem. Phys. Lett.*, **262**, (1996), 105.
- [13] D. Romanini, A.A. Kachanov, F. Stoeckel, *Chem. Phys. Lett.*, **270**, (1997), 538.
- [14] D. Romanini, A.A. Kachanov, N. Sadeghi, F. Stoeckel, *Chem. Phys. Lett.*, **264**, (1997), 316.
- [15] B.A. Paldus, C.C. Harb, T.G. Spence, B. Wilke, J. Xie, J.S. Harris, R.N. Zare, *J. Appl. Phys.*, **83**, (1998), 3991.
- [16] Y. He, M. Hippler, M. Quack, *Chem. Phys. Lett.*, **289**, (1998), 527.
- [17] M. Murtz, B. Frech, W. Urban, *Appl. Phys. B.*, **68**, (1999), 243.
- [18] M. Hippler, M. Quack, *Chem. Phys. Lett.*, **314**, (1999), 273
- [19] H. Linnartz, D. Pfluger, O. Vaizert, P. Cias, P. Birza, D. Khoroshev, J.P. Maier, *J. Chem. Phys.*, **116**, (2002), 924.

- [20] D. Pfluger, T. Motylewski, H. Linnartz, W.E. Sinclair, J.P. Maier, Chem. Phys. Lett., **329**, (2000), 29.
- [21] T. Motylewski, H. Linnartz, Rev. Sci. Instrum., **70**, (1999), 1305.
- [22] W.E. Sinclair, D. Pfluger, H. Linnartz, J.P. Maier, J. Chem. Phys **110**, (1999), 296.
- [23] D. Pfluger, W.E. Sinclair, H. Linnartz, J.P. Maier, Chem. Phys. Lett., **313** (1999), 171
- [24] P. Birza, T. Motylewski, D. Khoroshev, A. Chirokolava, H. Linnartz, J.P. Maier, Chem. Phys., **283**, (2002), 119
- [25] A. T. Droege, P. C. Engelking. Chem. Phys. Lett., (1999) , 110-96
- [26] D. T. Anderson, S. Davis, T. S. Zwier, D. J. Nesbitt. Chem. Phys. Lett., (1996), 207-258
- [27] http://sources.redhat.com/gsl/ref/gsl-ref_32.html#SEC439

Appendix 1

Low-voltage piezo actuators are manufactured in a lamination process, where thick-film electrodes are printed on green ceramic foils. The layers of ceramics and electrodes are then pressed together and cofired to form a monolithic block.

Typical layer thicknesses are in the range of 20 to 100 μm . After cutting the individual stacks to size, wire leads are applied.

Both types of piezo actuators can be used for many applications: Low-voltage actuators facilitate drive electronics design, high-voltage types operate to higher temperatures (150 $^{\circ}\text{C}$ compared to 80 $^{\circ}\text{C}$). Due to manufacturing technology, high-voltage ceramics can be designed with larger cross-sections suitable for higher-load applications (up to several tons) than low voltage ceramics.

Material Properties

Since the piezo effect exhibited by natural materials such as quartz, tourmaline, Rochelle salt, etc. is very small, polycrystalline ferroelectric ceramic materials such as barium titanate and lead (*plumbum*) zirconate titanate (PZT) with improved properties have been developed. These ferroelectric ceramics become piezoelectric when poled. PZT ceramics are available in many variations and are still the most widely used materials for actuator applications today. At temperatures below the Curie temperature, PZT crystallites exhibit tetragonal or rhombohedral structure. Due to their permanent electrical and mechanical asymmetry, these types of unit cells exhibit spontaneous polarization and deformation. Groups of unit cells with the same polarization and deformation orientation are called domains. Because of the random distribution of the domain orientations in the ceramic material, a ferroelectric poling process is required to obtain any macroscopic anisotropy and the associated piezoelectric properties (see Fig. 3.10). If heated above the Curie temperature, however, the PZT crystallite unit cells take on cubic centrosymmetric (isotropic) structure. When cooled, the domains reform, but with randomized orientations, and the material does not regain its macroscopic piezoelectric properties.

The asymmetric arrangement of the positive and negative ions imparts permanent electric dipole behavior to the crystals. Before the poling treatment, the domains are randomly oriented in the raw PZT material. During poling, an intense electric field (> 2000 V/mm) is applied to the piezo ceramic. With the field applied, the material expands along the axis of the field and contracts perpendicular to that axis as the domains line up. When the field is removed, the electric dipoles stay roughly, but not completely, in alignment. The material now has a remanent polarization (which can be degraded by exceeding the mechanical, thermal and electrical limits of the material). Subsequently, when a voltage is applied to the poled piezoelectric material, the ions in the unit cells are shifted and, additionally, the domains change their degree of alignment. (see Fig. 3.22). The result is a corresponding change of the dimensions (expansion, contraction) of the PZT material.

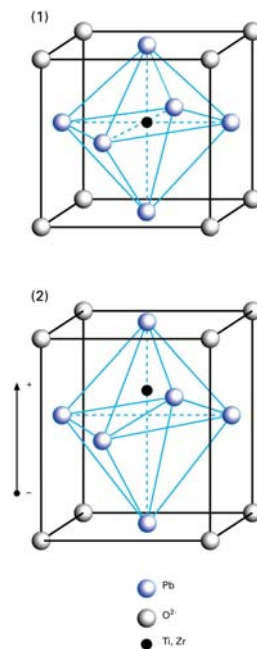


Figure 3.22 PZT unit cell: 1) Perovskite-type lead zirconate titanate (PZT) unit cell in the symmetric cubic state above the Curie temperature. 2) Tetragonally distorted unit cell below the Curie temperature

Resolution

Since the displacement of a piezo actuator is based on ionic shift and orientation of the PZT unit cells, the resolution depends on the electrical field applied and is theoretically unlimited. Infinitesimally small changes in operating voltage are converted to smooth movements. No threshold voltages influence the constant motion. Piezo actuators are used in atomic force microscopes to produce motion less

than the diameter of an atom. Since displacement is proportional to the applied voltage, optimum resolution cannot be achieved with noisy, unstable voltage sources.

Amplifier Noise

As stated above, amplifier noise directly influences the position stability (resolution) of a piezo actuator. Some vendors specify the noise value of their PZT driver electronics in millivolts. This information is of little use without spectral information. If the noise occurs in a frequency band far beyond the resonant frequency of the mechanical system, its influence on mechanical resolution and stability can be neglected. If it coincides with the resonant frequency, it will have a more significant influence on the system stability. Therefore, meaningful data can only be acquired if resolution of the complete system—piezo actuator and drive electronics—is measured in terms of nanometers rather than millivolts

Appendix 2

Intracavity Etalon Assembly

Single-frequency operation in 899-05, -21, and -29 Ring Lasers is ensured with a pair of moderate finesse etalons mounted in a rugged, pre-aligned assembly. Both the thick (10.0 mm) and thin (0.5 mm) etalons have hard dielectric coatings that produce nearly constant finesse from 370 nm to 1500 nm, with minimum absorption loss. The thin etalon is mounted on a galvo drive that controls its tip angle. Coherent's patented, thicketalon design uses a pair of Brewster-cut Littrow prisms. This allows the etalon to be PZT-tuned while still maintaining the advantages of an optically solid etalon, e.g., no AR-coated surfaces, low walk-off losses, and fast response. An independent servo circuit in the 899 Ring Laser Control Unit keeps the thick etalon aligned with the laser cavity mode during scanning.

Vertex-Mounted Brewster Plate

The 899-21 has a linear, controlled-scanning range of 30 GHz. The cavity mode frequency is scanned by rotating a single galvodriven Brewster plate, mounted at the vertex of the ring, through a small angle, thus producing an optical path-length change and continuous tuning. This design minimizes power modulation and beam movement in the cavity during the scan.

899 Ring Laser Control Unit

The 899 Ring Laser Control Unit provides precise and flexible operation and a convenient interface to other experimental equipment. Its outstanding reliability ensures years of trouble-free use. The 899 Ring Laser Control Unit includes:

- Precision digital controls for scan selection—center frequency and scan width are variable in 10 MHz increments.
- Switch-Selectable Free-Run (servo off) or actively stabilized operation.
- Single-sweep mode. The internal sweep is activated once—without retrace—or can be manually controlled from the front panel.

- External Scan enables the laser scan to be controlled by an external input voltage.
- Panel display of laser power, thicketalon offset, scanning Brewsterplate position, or any external applied signal.

Titanium: sapphire is a birefringent optical material, and the operation of the laser is very sensitive to the orientation of the Ti:S crystal with respect to the cavity beam. The *C* axis of the crystal must be aligned in the plane of incidence, and the Brewster surface must be maintained perpendicular to the plane of incidence. Otherwise, the birefringence of the Ti:S crystal will combine with that of the birefringent filter, resulting in uneven tuning and increased optical loss. The Ti:S crystal in the 899 Ring Laser is mounted in a special holder that provides precisely adjustable rotation about the normal-to-the-Brewster surface. This adjustment ensures optimal alignment of the *C* axis of the Ti:S crystal for smooth tuning, while maintaining alignment of the Brewster surface for low loss and maximum tuning range. The 899 Ring Laser is guaranteed to tune smoothly across its entire specified tuning range, without skips or gaps

The 899-29 AUTOSCAN II provides computer control of the complete laser system for the rapid accumulation of calibrated, high-resolution spectral data. Integrating a full-function 899-21 Ring Laser with a unique wavelength meter and computer control of the laser filter stack, the 899-29 continuously controls, monitors and optimizes the laser system while recording multiple channels of experimental data.

Fully automated scans of any length

Synchronous monitoring of wavelength meter channels and 899-21 functions allows the AUTOSCAN II to stack a large number of short scans that provide wavelength-labeled seamless spectra over any desired length, all from a few simple keyboard commands. The AUTOSCAN II system reduces the time required to perform high-resolution wide scan laser spectroscopy to the point that measurements once considered impractical or too time-consuming can be performed routinely. Data taken during a scan can be monitored in near real-time on the computer screen or dumped directly onto disk for later analysis. Because data collection is synchronized

to the laser scan, data is calibrated to the accuracy of the wavelength meter, providing unambiguous spectral assignments.

200 MHz absolute wavelength accuracy

The 899-29 AUTOSCAN II System consists of the most accurate wavelength meter commercially available, integrated with an 899-21 Ring Laser with extended control systems and interface electronics. The wavelength meter is mounted directly on the laser for stability and ease of alignment. Two optical components are used to determine the precise wavelength of the laser. The first, called the Optical Activity Monochromator (OAM), uses the optical activity of quartz to make a coarse wavelength measurement. A Vernier Etalon (VET) is then used to further refine the accuracy of measurement. This provides a specified absolute accuracy of ± 200 MHz and a specified precision of ± 50 MHz over the 450 to 900 nm operating range of the wavelength meter.

PC-Compatible computer control with advanced software

The AUTOSCAN II program features a menu-driven format for easy command entry. To collect data, the operator defines the necessary scan parameters, such as scan width and resolution, using menu commands. Then the complete set of parameters can be stored for later retrieval. The program also supports user-defined macros that allow the automatic execution of a sequence of commands, useful for applications requiring signal averaging or background subtraction. Extensive diagnostic routines provide performance checks and control of individual hardware components of the laser during alignment. An error-detection handler, built into the main program, checks the validity of all sensor signals and ensures that the operator knows when to perform routine maintenance on the system. AUTOSCAN II uses a dedicated and proprietary version of a DOS compatible computer system.

Chapter 4 High resolution spectroscopy with cw-CRD spectrometer

4.1 Lifetime broadening in the gas phase $\tilde{B}^2\Pi \leftarrow \tilde{X}^2\Pi$ electronic spectrum of C_8H

4.1.1 Abstract¹

The origin band of the $\tilde{B}^2\Pi_3 \leftarrow \tilde{X}^2\Pi_3$ electronic transition of linear C_8H was recorded in a planar supersonic expansion by a cw-CRD spectrometer. The C_8H radical was produced using a discharge through a C_2H_2/He mixture inside a pulsed slit nozzle. Despite the fact that the resolution of the spectrometer is 350 MHz, which is 3-4 times higher than the separation of rotational lines in this band, the rotational structure was not resolved. It is concluded that the rotational lines are broadened by rapid radiationless transitions from the excited electronic state. Simulations of the spectrum give an estimate of 0.8 cm^{-1} Lorentzian linewidth which corresponds to ~ 7 ps lifetime in the excited $\tilde{B}^2\Pi_3$ electronic state.

4.1.2 Introduction

Electronic spectra of carbon chains are especially of interest from the astrophysical point of view. Linear hydrocarbon chains C_nH play an important role in the interstellar chemistry. They were detected in the envelopes of evolved stars and

¹ This chapter is a slightly modified from the article published in: P. Birza, *et al.*, Chem. Phys. Lett. 382 (2003) 245-248

interstellar dark and translucent clouds by radio astronomy [1-3]. These species were extensively studied in the laboratory by microwave [4,5] and electronic spectroscopies [6,7]. Recent progress in experimental techniques made the measurement of rotationally resolved absorption spectra of electronic transitions in shorter carbon chains possible [8-12]. The origin band of the $\tilde{B}^2\Pi \leftarrow \tilde{X}^2\Pi$ electronic transition of the $C_{2n}H$ ($n=3-5$) radicals was observed in the gas phase using a combination of pulsed laser CRD with the slit-nozzle expansion of the discharge-generated species [8-13]. Whereas the spectrum of C_6H was rotationally resolved, the ones of C_8H and $C_{10}H$ were not. The reason was not clear. We attempted to resolve the rotational structure in the stronger ($\Omega=3/2$) component of the $\tilde{B}^2\Pi \leftarrow \tilde{X}^2\Pi$ origin band of C_8H using a new cw-CRD spectrometer setup with resolution of 350 MHz.

4.1.3 Experimental approach

The main features of the experiment have been described previously (12 and chapter 3). It is based on the passive cavity mode locking scheme for cw-CRD spectrometer [14]. A piezo moves back and forth one of the mirrors of the cavity. When the cavity comes into resonance with the laser frequency and intensity on the photodetector behind the cavity increases to a certain threshold, the laser beam is interrupted by switching off the acousto-optic modulator. The light intensity in the cavity and on the photodetector then decays exponentially with time. Due to spatial filtering and mode matching of the laser beam, only TEM_{00} cavity modes have significant intensity. The timing of the valve opening and high voltage pulse is calculated so as to coincide with the ring down.

The carbon chain species were generated by applying a high voltage pulse (-1000 V, 150 mA) to a 0.2% gas mixture of acetylene in helium expanding through the slit nozzle (3 cm \times 200 μ m) with the backing pressure of 11 bar. The pressure in the vacuum chamber was 0.23 mbar. The laser beam crossed the jet at 10 mm downstream the expansion. The number density of C_8H species in this region was estimated using a theoretical oscillator strength (3.4×10^{-3}) for this electronic

transition [15]. In the 5 K neon matrix spectrum, the integrated absorption of the origin band is approximately equal to that of the other vibronic bands in the $\tilde{B}^2\Pi \leftarrow \tilde{X}^2\Pi$ system [6]. Because only the origin band was measured in our experiment, the oscillator strength was reduced accordingly and leads to an estimate of the C_8H number density in the discharge plasma of $6 \times 10^8 \text{ cm}^{-3}$.

4.1.4 Results and discussion

The recorded spectrum is shown in Fig. 4.1. The two broad features are the P – and R – branches of the origin band of the $\tilde{B}^2\Pi_{3/2} \leftarrow \tilde{X}^2\Pi_{3/2}$ electronic transition of C_8H . This band was first observed in 5 K neon matrix using mass-selected deposition [6]. It was assigned in the gas phase [13] on the basis of the known gas phase - neon matrix shifts [16] for similar hydrocarbon chains. This assignment was confirmed by equal frequency shifts resulting from deuterium substitution in the neon matrix [17] and in the supersonic jet experiment [13].

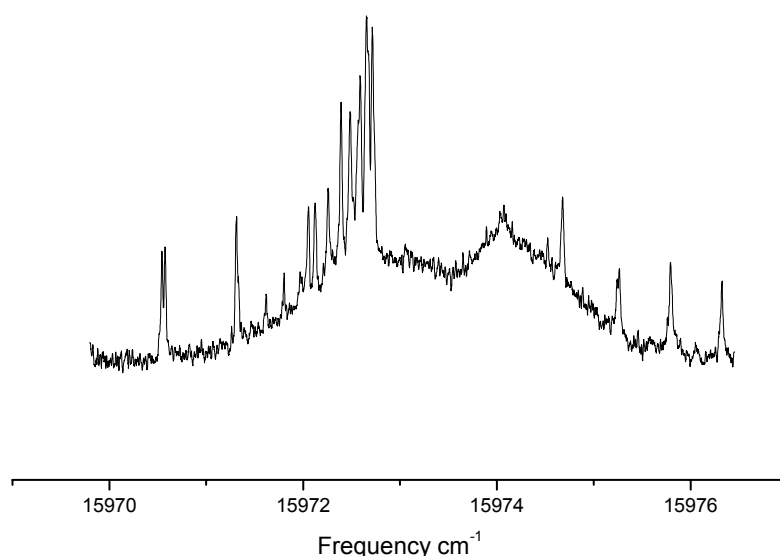


Figure 4.1 Experimental spectra of the origin band in the $\tilde{B}^2\Pi_{3/2} \leftarrow \tilde{X}^2\Pi_{3/2}$ electronic transition of C_8H .

The large narrow peaks belong to another carrier, propadienylidene (H_2CCC). They are much stronger in this spectrum compared to the earlier measurement [13] because a slightly different nozzle design [12] has been used. The latter minimizes Doppler broadening but at the same time increases the production of shorter carbon chains. Although overlap with the features of another carrier complicates the spectrum, one can see that the rotational structure of C_8H remains unresolved.

The distance between the lines in the P and R branches is expected to be about 0.04 cm^{-1} (1.2 GHz). Our resolution, estimated by the width of the narrowest feature (FWHM) in the spectrum, was at least 350 MHz. It should be more than sufficient to resolve the rotational structure of the C_8H band. One can compare this spectrum to the origin band in the $\tilde{\text{A}}^2\Pi_{3/2} \leftarrow \tilde{\text{X}}^2\Pi_{3/2}$ transition of the isoelectronic linear tetraacetylene cation, HC_8H^+ , recorded under similar conditions with a laser linewidth of $\sim 900\text{ MHz}$ (see Figure 4.2). There the P branch is well resolved; the R branch is partially resolved.

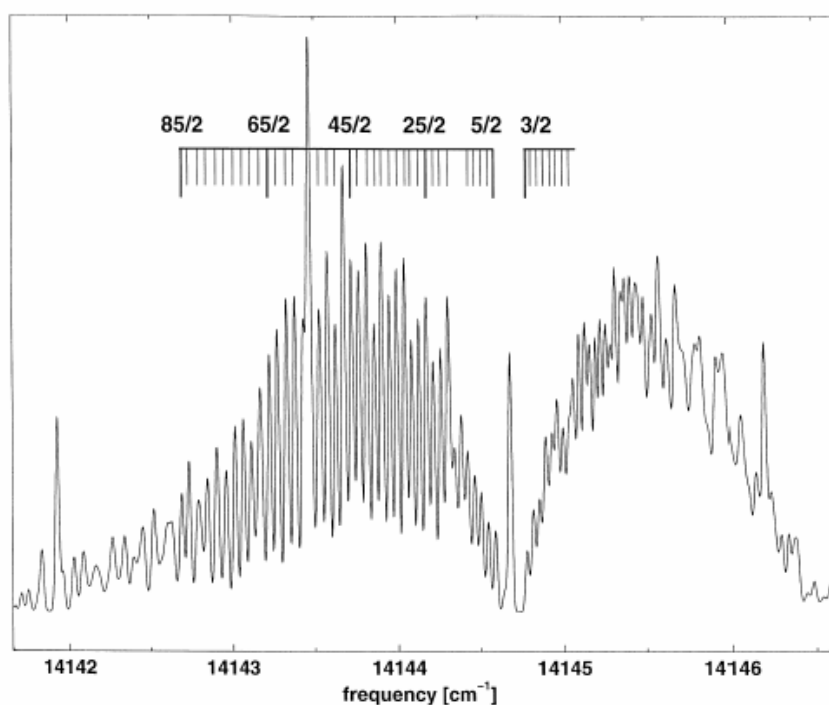


Figure 4.2 Rotationally resolved CRD absorption spectrum of the ${}^2\Pi_{3/2} \leftarrow {}^2\Pi_{3/2}$ electronic origin band transition of HC_8H^+ , recorded through a supersonic planar plasma $T_{\text{rot}} \approx 15\text{ K}$.

The rotational level broadening in the upper $\tilde{\mathbf{B}}^2\Pi$ electronic state of C_8H is caused by rapid radiationless transitions from this electronic state. Nonradiative relaxation of the $\tilde{\mathbf{B}}^2\Pi$ electronic state is present in other members of the C_{2n}H series as well. It manifests itself as a two-component fluorescence decay in C_4H with excited state lifetime estimate of 20 ns [18]. In the case of C_6H (8), the $\tilde{\mathbf{B}}^2\Pi_{3/2} \leftarrow \tilde{\mathbf{X}}^2\Pi_{3/2}$ electronic absorption spectrum is best simulated when a Lorentzian broadening of $\sim 0.055 \text{ cm}^{-1}$ is introduced in addition to a Gaussian linewidth of 0.037 cm^{-1} resulting from the laser linewidth and Doppler broadening. This corresponds to an excited state lifetime of order 0.1 ns. The spectrum was recorded in absorption across a pulsed supersonic slit jet using a cw – CRD approach. The two broad features are the *P* and *R* branches of this electronic transition. The narrow peaks belong to propadienylidene H_2CCC .

We simulated the observed broadening in the $\tilde{\mathbf{B}}^2\Pi_{3/2} \leftarrow \tilde{\mathbf{X}}^2\Pi_{3/2}$ origin band of C_8H (Figure 4.3) by varying three parameters: upper state rotational constant B' , rotational temperature T_{rot} , and Lorentzian linewidth Δv_{lor} . B'' was fixed to the value of $0.019589011 \text{ cm}^{-1}$ taken from Ref. [4]. The obtained values are $B'=0.0195\pm 0.0001 \text{ cm}^{-1}$, $T_{\text{rot}}=15\pm 2 \text{ K}$, and $\Delta v_{\text{lor}}=0.8\pm 0.1 \text{ cm}^{-1}$ (24 GHz), respectively where the values and errors were determined by try and error with visual check between observed and simulated rotational profiles. Thus, the ratio B'/B'' for C_8H is 0.995 ± 0.005 , which is close to the value of 0.99 for isoelectronic species [9-11].

Upper state rotational constant for the simulated spectrum in Figure 4.3 is $B' = 0.0195 \text{ cm}^{-1}$, other constants are fixed to the ground state values (4). Rotational temperature is $T_{\text{rot}} = 15 \text{ K}$, Lorentzian broadening $\Delta v_{\text{lor}} = 0.8 \text{ cm}^{-1}$ (24 GHz). The simulated spectrum is slightly shifted down with respect to the experimental one.

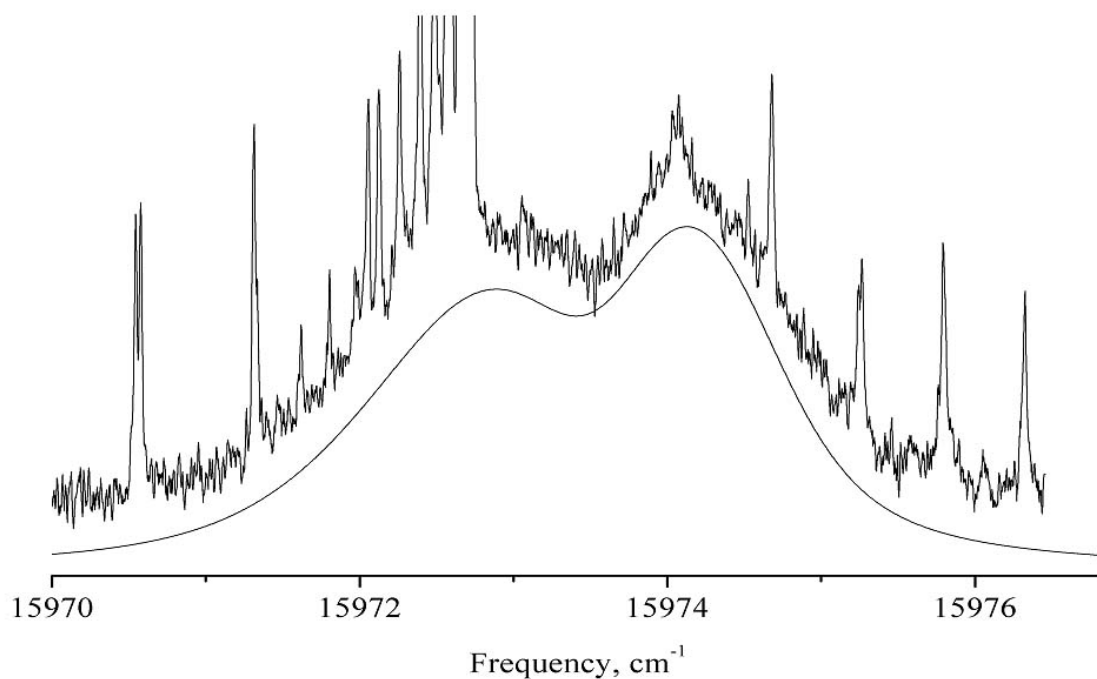


Figure 4.3. Experimental and simulated spectra of the origin band in the $\tilde{B}^2\Pi_3 \leftarrow \tilde{X}^2\Pi_3$ electronic transition of C_8H .

In contrast to C_8H , the rotational structure is well resolved for the corresponding $\tilde{A}^2\Pi \leftarrow \tilde{X}^2\Pi$ electronic origin bands of the isoelectronic linear cations HC_8H^+ [9], HC_7N^+ [10], and NC_6N^+ [11]. Apparently, the presence of an additional low-lying $^2\Sigma^+$ excited electronic state in the C_6H and C_8H radicals [15,19-21] enhances vibronic interactions between the $\tilde{B}^2\Pi$ and lower electronic states and accelerates internal conversion. This broadening caused by intramolecular processes is one of the reasons why carbon chains attracted attention in connection with the diffuse interstellar bands [22].

4.2 Rotationally resolved electronic spectrum of propadienylidene

4.2.1 Abstract²

The rotationally resolved electronic spectrum of a vibrational band in the \tilde{A}^1A_2 - \tilde{X}^1A_1 transition of the cumulene carbon chain C_3H_2 was measured in the 625 nm region in a supersonic discharge using cw cavity ring down spectroscopy. The rotational structure was analysed using a conventional Hamiltonian for an asymmetric top molecule, and the constants A' , B' and C' in the upper state were determined. The observed band is assigned to a combination of a_1 and b_2 vibrations with the frequency around 2000 cm^{-1} . The geometries in the 1A_1 , 1A_2 , 1B_1 states and the intersection point between the latter two were obtained using *ab initio* calculations. The effective structure in the measured vibrational level of the 1A_2 state was inferred from the determined constants.

4.2.2 Introduction

High resolution gas-phase spectra of cumulene carbenes $H_2C(=C)_n$, highly polar molecules, are of interest from the viewpoint of astrochemistry, combustion, discharges, and molecular spectroscopy. A number of cumulene carbenes have been observed in the interstellar medium by radioastronomy [23,24]. The smallest member of this family, propadienylidene $CCCH_2$, was first detected in an argon matrix by IR spectroscopy [25]. After its gas-phase rotational spectrum was recorded in the laboratory [26], this molecule was discovered in the Taurus molecular cloud [27]. Its cyclic isomer, cyclopropenylidene, is widespread in space [28].

² This chapter is a slightly modified from the article published in: P. Birza, *et al.*, J. Mol. Spec. (2004)

Cumulene carbenes may be relevant to the problem of the diffuse interstellar bands (DIBs). The electronic spectrum of CCCH_2 was recorded in argon [29,30] and neon [30] matrices. It consists of a strong band system ($\tilde{\text{C}}^1\text{A}_1 \leftarrow \tilde{\text{X}}^1\text{A}_1$) with a vibrational progression in the 256 to 212 nm region and a number of weaker features in the 403-716 nm range assigned to $\tilde{\text{B}}^1\text{B}_1 \leftarrow \tilde{\text{X}}^1\text{A}_1$ and $\tilde{\text{A}}^1\text{A}_2 \leftarrow \tilde{\text{X}}^1\text{A}_1$ electronic transitions. On the basis of its electronic spectrum in a neon matrix, propadienylidene cannot be excluded as a DIB carrier [31] although many models suggest that such small molecules cannot survive in the radiation field of the diffuse cloud environment [32].

The strong $^1\text{A}_1 \leftarrow \tilde{\text{X}}^1\text{A}_1$ electronic transition of cumulene carbenes shifts to longer wavelengths with increase in chain length. It is predicted to be in the 400 – 860 nm DIB range for the 13 – 34 carbon chains [35]. The species of this size are expected to be stable to photodissociation. It is interesting to note that in some chemical models of interstellar clouds the molecules with C_nH_2 formula, both polyynes and cumulene carbenes, are especially abundant [33].

The structure of propadienylidene in the ground electronic state was determined from microwave studies of the four isotopomers [26,36]. It is a near prolate top with C_{2v} symmetry. Rotational constants B'' and C'' were determined to one part in 10^6 or better. However, the uncertainty for A'' was much higher because $\Delta K_a=2$ transitions could not be detected, and also due to a high correlation of A'' with some centrifugal distortion constants.

The photochemistry of C_3H_2 isomers was also studied in argon and neon matrices using IR and electronic spectroscopy [25,29]. The interconversion of cyclopropenylidene (c-CCHCH), propargylene (HCCCH) and propadienylidene was observed under various irradiation conditions. Singlet cyclopropenylidene is at the global minimum of the H_2C_3 potential energy surface according to theoretical calculations, singlet propadienylidene lies 0.4–0.6 eV, and triplet propargylene 0.6–0.95 eV higher than cyclopropenylidene [29,37,38].

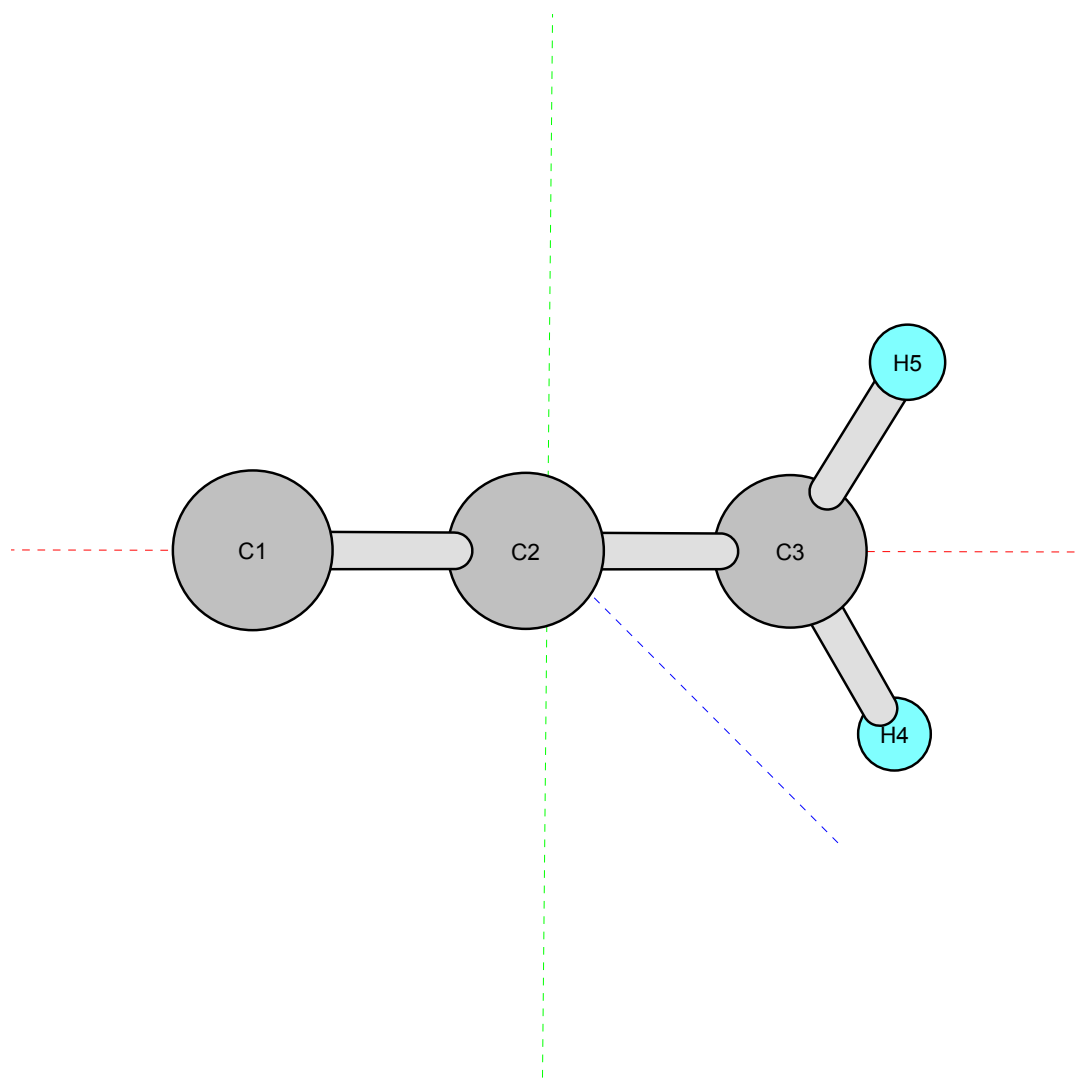


Figure 4.4 Structure of CCCH₂ using rotational constants from the ground state.

In this paper the gas-phase electronic spectrum of propadienylidene recorded in the 624.6-625.8 nm region is reported. The spectrum was observed when measuring an electronic transition of the C₈H radical [39].

4.2.3 Experiment

The spectrum was recorded using a cw cavity ring down (CRD) spectrometer sampling a supersonic expansion of a discharge plasma from a slit nozzle. The details have been given [39]. CCCH_2 was produced by a discharge (-800 V, 120 mA) through a gas mixture of 0.2% acetylene in helium with a backing pressure of 11 bar. The laser beam crossed the supersonic jet 7 mm downstream.

The light of a single mode ring dye laser, pumped by a 6 W solid state laser, is guided through an acousto-optical modulator (AOM). The first order deflection is focused into the ring down cavity via a lens so that the incoming laser light matches a TEM_{00} cavity mode. The CRD mirrors (1m plano-concave, $R > 99.995\%$) are mounted in a mechanically stable holder at a distance of 32 cm. One of the mirrors is on a piezo to which a periodic 60 Hz triangularly shaped voltage is applied. The cavity length is thus modulated and a strong transmission occurs only when it is resonant with the laser wavelength [40]. The light intensity after the cavity is monitored using a Si-photodiode and when it reaches a certain threshold, a trigger signal is generated that switches off the AOM. The laser beam is then interrupted, a ring down event initiated and fitted to an exponential. A spectrum is produced as a function of the ring down time versus laser frequency. The resolution of the recorded spectrum is 0.01 cm^{-1} (FWHM) as estimated by the narrowest lines. The linewidth is due to Doppler and lifetime broadenings while the 500 kHz contribution of the laser is negligible. The absorption spectrum of iodine in a cell was recorded concurrently for frequency calibration.

4.2.4. Results and discussion

4.2.4.1 Rotational analysis

Approximately 90 lines including blended ones were recorded in the 16000 cm^{-1} region and the spectrum is shown in Fig. 4.5 (lower trace). Initial rotational assignments were made using pattern recognition and polynomial fits of the lines in the P -, Q -, and R - branches. The spectrum was attributed to c -type transitions of a near-prolate top with $K_a = 0\leftarrow 1$, $K_a = 1\leftarrow 0$, and $K_a = 2\leftarrow 1$ subbands, where the choice for c - rather than b -type is indicated by the combination defects in the $K_a = 0\leftarrow 1$ and $K_a = 1\leftarrow 0$ subbands. When deuterated acetylene was used as a precursor, the present spectrum was not observed, so the carrier contains hydrogen atoms. By comparing the sum $B''+C''$ obtained from the polynomial fit with known rotational constants of various candidate molecules it was concluded that the spectrum belongs to propadienylidene. Propargylene (HCCCH) has similar rotational constants according to *ab initio* calculations [41] but its spectrum in an argon matrix shows no absorption in the 400-700 nm range [29].

A least-squares fit of the parameters with a conventional rotational Hamiltonian for an asymmetric top molecule without centrifugal distortion terms was made using the program WANG [42] to the frequencies of the 86 lines listed in Table 4.1. The upper state levels with $J = 2-4$ in the $K_a = 0$ manifold and the transitions to these levels in the $K_a = 0\leftarrow 1$ subband are split by a perturbation into doublets. They were included in the fit using the positions of hypothetically unperturbed rovibronic transitions determined by the weighted intensity of the doublet components. The obtained ground state constants A'' , B'' and C'' (Fit I, Table 4.2) coincide, within the accuracy of the fit, with the values derived from the microwave data [26], confirming the assignment of the transitions to propadienylidene. The ground-state rotational constants B'' and C'' were fixed to the values of Ref. [26] during the second fit because these have been accurately determined by microwave spectroscopy. The measured line frequencies and the ones generated by Fit II together

with their assignments are listed in Table 4.1. Because the transitions to the levels with three different values of

Table 4.1 Frequencies of the observed rovibronic lines in the $\tilde{A}^1A_2 \leftarrow \tilde{X}^1A_1$ transition of C_3H_2

J'_{KaKc}	J''_{KaKc}	$\nu_{\text{obs}} (\text{cm}^{-1})$	o-c (cm^{-1}) ^a
7 ₀₇ - 8 ₁₇		15966.2910	-0.0092
6 ₀₆ - 7 ₁₆		15967.2044	-0.0055
5 ₀₅ - 6 ₁₅		15968.0871	-0.0025
4 ₀₄ - 5 ₁₄		15968.9394 ^b	0.0000
3 ₀₃ - 4 ₁₃		15969.7606 ^b	0.0017
2 ₀₂ - 3 ₁₂		15970.5523 ^b	0.0037
1 ₀₁ - 2 ₁₁		15971.3132	0.0049
0 ₀₀ - 1 ₁₀		15972.0436	0.0055
11 ₀₁₁ - 11 ₁₁₁		15971.5965	0.0021
10 ₀₁₀ - 10 ₁₁₀		15971.7817	-0.0041
9 ₀₉ - 9 ₁₉		15971.9601	0.0000
8 ₀₈ - 8 ₁₈		15972.1034	-0.0124
7 ₀₇ - 7 ₁₇		15972.2419	-0.0125
6 ₀₆ - 6 ₁₆		15972.3749	-0.0000
5 ₀₅ - 5 ₁₅		15972.4730	-0.0062
4 ₀₄ - 4 ₁₄		15972.5771 ^b	0.0116
3 ₀₃ - 3 ₁₃		15972.6392 ^b	0.0046
2 ₀₂ - 2 ₁₂		15972.6992 ^b	0.0129
1 ₀₁ - 1 ₁₁		15972.7294	0.0086
2 ₀₂ - 1 ₁₀		15974.0480 ^b	0.0000
3 ₀₃ - 2 ₁₁		15974.6657 ^b	0.0075
4 ₀₄ - 3 ₁₂		15975.2384 ^b	0.0000
5 ₀₅ - 4 ₁₃		15975.7814	-0.0068
6 ₀₆ - 5 ₁₄		15976.3111	0.0027
7 ₀₇ - 6 ₁₅		15976.7972	-0.0010
8 ₀₈ - 7 ₁₆		15977.2509	-0.0071
9 ₀₉ - 8 ₁₇		15977.6908	0.0034
10 ₀₁₀ - 9 ₁₈		15978.0843	-0.0021
7 ₁₆ - 8 ₀₈		15985.5124	0.0054

$J'_{K_a K_c}$	$J''_{K_a K_c}$	$\nu_{\text{obs}} (\text{cm}^{-1})$	$\text{o-c} (\text{cm}^{-1})^{\text{a}}$
6 ₁₅ - 7 ₀₇		15986.3203	-0.0000
5 ₁₄ - 6 ₀₆		15987.1107	-0.0073
4 ₁₃ - 5 ₀₅		15987.8910	-0.0068
3 ₁₂ - 4 ₀₄		15988.6604	-0.0000
2 ₁₁ - 3 ₀₃		15989.3987	-0.0073
1 ₁₀ - 2 ₀₂		15990.1317	-0.0025
7 ₁₇ - 7 ₀₇		15990.7170	0.0113
6 ₁₆ - 6 ₀₆		15990.9129	-0.0000
5 ₁₅ - 5 ₀₅		15991.0887	-0.0034
4 ₁₄ - 4 ₀₄		15991.2533	0.0124
3 ₁₃ - 3 ₀₃		15991.3697	0.0097
2 ₁₂ - 2 ₀₂		15991.4584	0.0091
1 ₁₁ - 1 ₀₁		15991.4988	-0.0100
1 ₁₀ - 0 ₀₀		15992.2032	-0.0117
2 ₁₁ - 1 ₀₁		15992.8683	-0.0054
3 ₁₂ - 2 ₀₂		15993.5075	-0.0077
4 ₁₃ - 3 ₀₃		15994.1368	-0.0026
5 ₁₄ - 4 ₀₄		15994.7428	-0.0035
6 ₁₅ - 5 ₀₅		15995.3405	0.0045
7 ₁₆ - 6 ₀₆		15995.9200	0.0116
8 ₁₇ - 7 ₀₇		15996.4696	0.0059
<hr/>			
8 ₂₆ - 9 ₁₈		16003.3733	-0.0000
8 ₂₇ - 9 ₁₉		16003.9429	0.0000
7 ₂₅ - 8 ₁₇		16004.3120	0.0000
7 ₂₆ - 8 ₁₈		16004.7682	0.0012
6 ₂₄ - 7 ₁₆		16005.2210	0.0000
6 ₂₅ - 7 ₁₇		16005.5762	0.0015
5 ₂₃ - 6 ₁₅		16006.1004	0.0013
5 ₂₄ - 6 ₁₆		16006.3670	0.0019
4 ₂₂ - 5 ₁₄		16006.9500	0.0017
4 ₂₃ - 5 ₁₅		16007.1405	0.0021

$J'_{K_a K_c}$	$J''_{K_a K_c}$	$\nu_{\text{obs}} (\text{cm}^{-1})$	$\text{o-c} (\text{cm}^{-1})^{\text{a}}$
3 _{2 2}	- 4 _{1 4}	16007.8968	0.0023
2 _{2 1}	- 3 _{1 3}	16008.6358	0.0025
10 _{2 9}	- 10 _{1 9}	16009.1059	0.0040
9 _{2 8}	- 9 _{1 8}	16009.4046	0.0037
10 _{2 8}	- 10 _{1 10}	16009.8162	0.0104
7 _{2 6}	- 7 _{1 6}	16009.9105	0.0013
9 _{2 7}	- 9 _{1 9}	16009.9731	-0.0026
8 _{2 6}	- 8 _{1 8}	16010.1219	-0.0073
5 _{2 4}	- 5 _{1 4}	16010.2906	-0.0073
6 _{2 4}	- 6 _{1 6}	16010.3894	0.0036
4 _{2 3}	- 4 _{1 3}	16010.4468	-0.0000
5 _{2 3}	- 5 _{1 5}	16010.4859	-0.0027
4 _{2 2}	- 4 _{1 4}	16010.5733	-0.0012
3 _{2 1}	- 3 _{1 3}	16010.6487	0.0054
2 _{2 0}	- 2 _{1 2}	16010.6944	-0.0000
2 _{2 1}	- 1 _{1 1}	16012.0599	-0.0094
3 _{2 1}	- 2 _{1 1}	16012.6642	-0.0026
3 _{2 2}	- 2 _{1 2}	16012.7029	-0.0019
4 _{2 2}	- 3 _{1 2}	16013.2454	-0.0017
4 _{2 3}	- 3 _{1 3}	16013.3168	-0.0063
6 _{2 4}	- 5 _{1 4}	16014.3160	-0.0026
6 _{2 5}	- 5 _{1 5}	16014.5078	-0.0000
7 _{2 5}	- 6 _{1 5}	16014.8083	-0.0015

^a Fit II in Table 4.2.

^b These were included in the fit using the positions of hypothetical unperturbed rovibronic transitions determined by the weighted intensity of the doublet components.

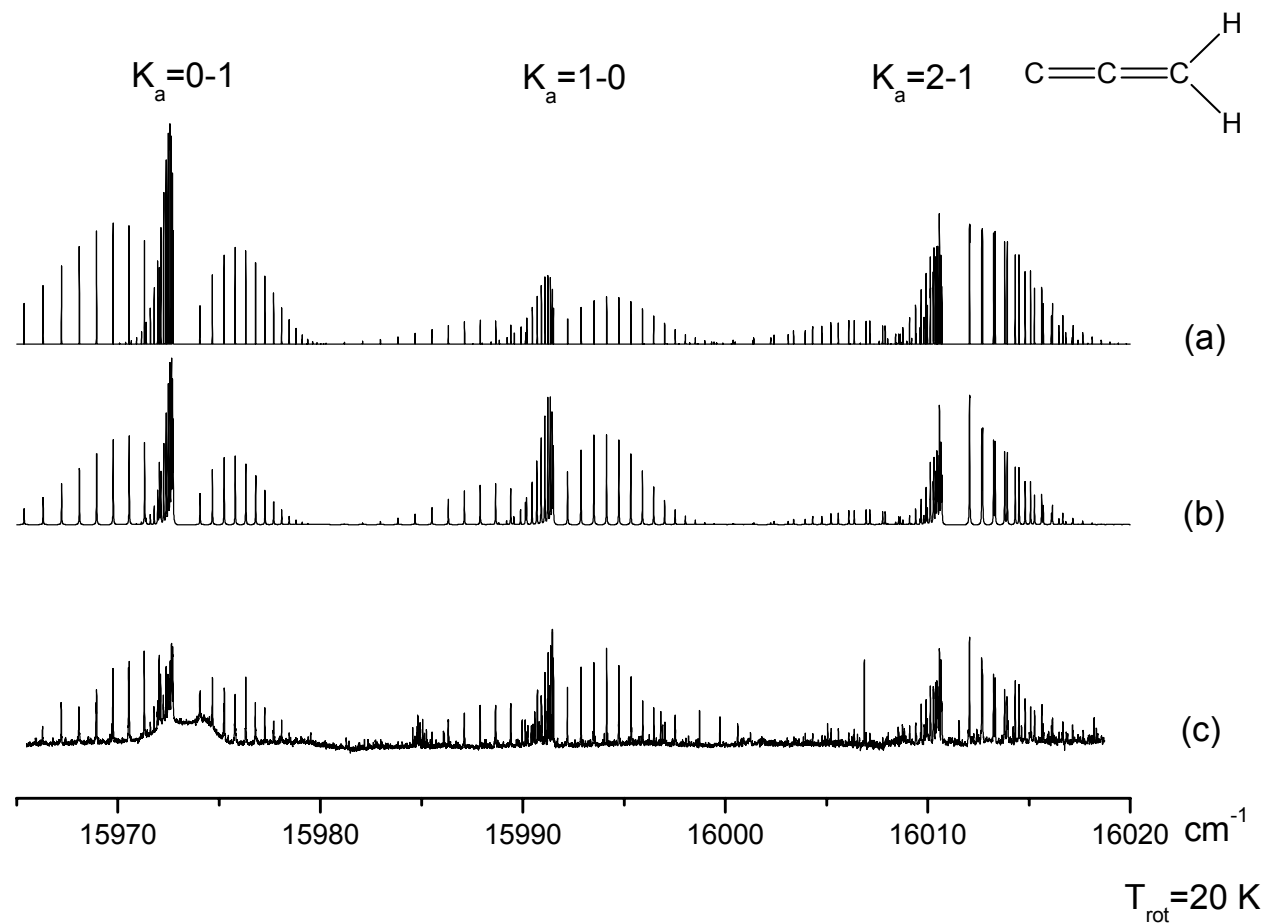


Figure 4.5 Rotationally-resolved spectrum of C_3H_2 (trace **c**) in comparison with the simulated ones: trace **a** using the independent Boltzmann population model, trace **b** a single Boltzmann population for the two nuclear spin isomers (spin statistical weights ee:eo:oe:oo=1:1:3:3). The broad structure around 15970 cm^{-1} is the origin band of the $\tilde{B}^2\Pi_{3/2} - \tilde{X}^2\Pi_{3/2}$ transition of C_8H

upper state K_a were included, it was possible to determine the rotational constants A'' and A' (Table 4.2) with higher accuracy than for A'' in the microwave study [36]. Using the determined molecular constants (Fit II, Table 4.2) the rotational profiles were simulated with the program WANG to compare with the observed spectrum as shown in Fig. 4.5. It was modified in order to consider independent Boltzmann populations (hereafter IBP) between ortho and para nuclear spin isomers, because the spectrum was observed at the low temperature of 20 K and propadienylidene is a light molecule.

Table 4.2 Molecular constants (cm^{-1})^a of C_3H_2

	Constants	Fit I	Fit II	Ref. [4]
	A''	9.6453(17)	9.6451(17)	9.6328(11)
\tilde{X}^1A_1	B''	0.353117(84)	0.353198 ^b	0.353198(67)
	C''	0.340435 (79)	0.340367 ^b	0.340367(67)
	A'	9.83716(42)	9.83717(46)	
\tilde{A}^1A_2	B'	0.34121(11)	0.341217(86)	
	C'	0.32876(12)	0.328764(91)	
	ν	15982.0366(15) ^c	15982.0367(16) ^c	
	rms	0.0058	0.0060	

^a Values in parentheses denote the standard deviation and apply to the last digits of the constants.

^b Fixed to the value of Ref. [26].

^c The error is from the least-squares fitting, and uncertainty of the calibration is 0.01 cm^{-1} .

However the relative intensities of the simulated spectrum with the IBP model (trace *a* in Fig. 4.5) are not entirely consistent with the observation (trace *c*), *i.e.* relative intensity of the $K_a = 1 \leftarrow 0$ subband in the simulation is weaker. Thus the spectrum was simulated with a single Boltzmann population for the two nuclear spin isomers as shown in trace *b*, which agrees well with the observed relative line intensities. In order to explain the difference to the IBP simulation, two reasons can be

offered: (1) full collisional equilibration is not achieved 7 mm downstream from the slit nozzle and (2) the intensities are affected by vibronic interaction with the nearby 1B_1 state. In connection with this the study of the 1A_1 - $\tilde{X}{}^1A_1$ electronic transition of H_2CO is relevant [54]. The observed rotational line intensities using a seeded helium free jet (fig 1b of ref. 54) can be reproduced well using the IBP model. However, in the spectrum with Ar as carrier gas (fig. 1c of ref.54) the relative intensities of the $K_a = 1 \leftarrow 0$ subband are several times stronger than the simulated one produced by the modified WANG program with IBP. This indicates that collisional relaxation depends on the discharge conditions.

4.2.4.2. Ab initio calculations

In order to obtain electronic and vibrational assignments for the recorded band *ab initio* calculations using the Molpro program [43, 44] with cc-pVTZ basis set were carried out. The adiabatic transition energies and geometry optimization of $CCCH_2$ were computed using the CASPT3 (RSPT3) [45,46] and MRCI [47,48] methods with Davidson correction MRCI+D. Two active spaces CAS6 and CAS10 including 6 and 10 orbitals, respectively, were used for the CASPT3 calculation, and CAS6 for the MRCI one. The active space CAS6 includes all 5 π -orbitals of the molecule and the C atom lone-pair orbital $a_1, b_1, b_2, a_2 = 1, 3, 2, 0$ (C_{2v} point group) with 6 electrons. CAS10 includes additionally two bonding and two antibonding C-H σ -orbitals: $a_1, b_1, b_2, a_2 = 3, 3, 4, 0$ with 10 electrons. During all the calculations the core orbitals were treated uncorrelated.

The adiabatic transition energies calculated with the various methods [31,38,49-51] and the electronic excitation energies from the absorption spectrum of $CCCH_2$ in neon matrix [31] are listed in Table 4.3. The theoretical and experimental values are in good agreement, somewhat better than with the previous MRCI [38] and CASPT2 [49] results, and significantly than those of single-reference methods [50,51]. Therefore, the present band (1.98 eV) is assigned to a vibronic transition within the $\tilde{A}{}^1A_2$ - $\tilde{X}{}^1A_1$ electronic band system.

Table 4.3 Adiabatic transition energies (eV) of C₃H₂

Method	$\tilde{A}^1A_2 \leftarrow \tilde{X}^1A_1$	$\tilde{B}^1B_1 \leftarrow \tilde{X}^1A_1$
Ne-matrix ^{a,b}	≤ 1.733	2.036
RSPT3, CAS10	1.737	2.023
RSPT3, CAS6	1.730	1.985
MRCI+D, CAS6	1.752	2.015
MRCI+D ^c	1.77	2.05
CASPT2 ^d	1.69	1.93
CCSD ^e	1.91	2.49
CC3 ^f	1.80	2.14
CCSD/CC3 ^g	1.75	1.97

^a 13975 cm⁻¹ for the lowest observed band of the $\tilde{A}^1A_2 \leftarrow \tilde{X}^1A_1$ transition and 16426 cm⁻¹ for the origin of the $\tilde{B}^1B_1 \leftarrow \tilde{X}^1A_1$ transition.

^b Ref. [31].

^c 8 orbitals with 8 electrons in the active space and ANObasis set C: 4s3p2d, H:3s2p, Ref. [38].

^d Ref. [49].

^e Ref. [50].

^f Ref. [51].

^g Estimation of excitation energy: $E = E_{\text{CCSD}} + 3/2 (E_{\text{CC3}} - E_{\text{CCSD}})$ Ref. [9].

The observed transition around 15982 cm⁻¹ is probably related to one of the two vibronic bands observed in the neon matrix [31] at 16161 cm⁻¹ and 15813 cm⁻¹. The ¹A₂ state corresponds to a $\pi^* \leftarrow \pi$ excitation, for which a red solvatochromic shift is usually observed in matrices. However, the matrix-gas shifts make the correspondence between the spectra uncertain.

Because the observed band is of *c*-type, its vibrational component should belong to b₂ symmetry e.g., a combination of a₁ and b₂ modes. It should have a vibrational frequency about 2000 cm⁻¹. Calculation of the vibrational frequencies for the ¹A₂ state was carried out using the CASSCF method with 10 active orbitals (Table 4.4). There are two combination levels consistent with the observed frequency and symmetry: (i) $\omega_4(a_1) + \omega_8(b_2)$: 1983 cm⁻¹, and (ii) $\omega_2(a_1) + \omega_9(b_2)$: 1869 cm⁻¹.

Table 4.4 Calculated vibrational frequencies (cm⁻¹) of C₃H₂

Mode	\tilde{X}^1A_1		\tilde{A}^1A_2		
	Experimental ^a	CAS(10)	CAS(10)		
a ₁	ω_1		3010	3022	C-H symmetric stretching
	ω_2	1952	2066	1707	C-C asymmetric stretching
	ω_3	1446	1501	1436	H-C-H symmetric bending
	ω_4		1154	1042	C-C symmetric stretching
b ₁	ω_5		975	530	C-C-H out of plane bending
	ω_6		254	337	C-C-C out of plane bending
b ₂	ω_7		3085	3113	C-H asymmetric stretching
	ω_8	1002	1072	941	H-C-H asymmetric bending
	ω_9		236	162	C-C-C asymmetric bending

^a Ref. [26,29] .

4.2.5 Molecular structure

The equilibrium structure and rotational constants for the 1A_1 , 1A_2 and 1B_1 states have been calculated (Table 4.5). These predict a decrease of all rotational constants upon electronic excitation. Although the experimentally determined rotational constants B and C decrease upon excitation, A becomes larger. This discrepancy could be caused by vibronic coupling between the 1A_2 and 1B_1 states [31] or an anharmonic force field [52], neither of which were taken into account in the calculations.

The bond length C3-H does not change according to the calculated geometries of the 1A_1 , 1A_2 and 1B_1 states (Table 4.5). Thus it can be fixed in the determination of the molecular structure. Using a least-squares fit, the structure of the vibrationally excited molecule in the 1A_2 electronic state is determined from the observed rotational constants to be

$$r(\text{C1-C3}) = 2.6618(24) \text{ \AA} \text{ and } \theta(\text{C2-C3-H}) = 121.5511(35)^\circ$$

where $r(\text{C3-H})$ was fixed to the 1.082 Å value in the 1A_1 state from the *ab initio* calculations. Increase in the bond length $r(\text{C1-C3})$ and angle $\theta(\text{C2-C3-H})$ upon excitation is indicated (Table 4.5). The errors (1σ in the least-squares fit) may be due to the effects of vibration. An independent determination of the bond lengths $r(\text{C1-C2})$ and $r(\text{C2-C3})$ was not possible in spite of using the two rotational constants B' and C' because carbon atom C2 is almost at the molecular center of mass. Spectra of ${}^{13}\text{C}$ isotopic species of this molecule might provide the independent information for the determination of the four structural parameters.

The energies of the 1A_2 and 1B_1 states are rather close to each other, about 0.30 eV (Table 4.3), but the calculated equilibrium geometries differ significantly (Table 4.5). The C1–C2 bond length changes by 0.11 Å and that of C2–C3 by –0.06 Å. Therefore, it is not surprising that root flipping between these states is predicted by the calculations. At the equilibrium geometry of the 1B_1 state, the energy of the 1A_2 state is 0.15 - 0.17 eV higher than of 1B_1 one as shown in Table 4.6. Differences in the geometry parameters between the equilibrium geometries of A_2 and B_1 states can be gathered in the vector Δ_{geo} :

$$\Delta_{geo} = ({}^1A_2 \text{ equilibrium geometry}) - ({}^1B_1 \text{ equilibrium geometry})$$

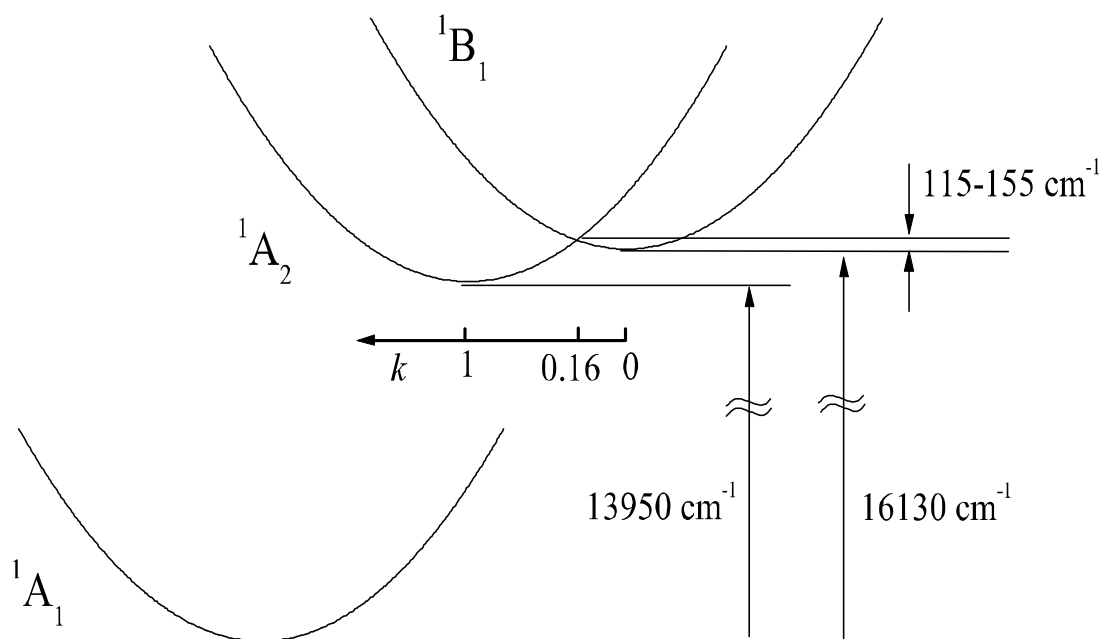


Figure 4.6 Schematic potentials of the 1A_2 and 1B_1 states and the intersection point. The parameter k is used to define the intersection point between the states.

The Δ_{geo} vector and k parameter were introduced to find the intersection point of the potential energy surfaces within the linear interpolation model. To generate intermediate geometries a proportionality constant k defined by:

$$(\text{intermediate geometry}) = (^1B_1 \text{ equilibrium geometry}) + k \times \Delta_{geo}$$

was used. The parameter k indicates the position of the intersection point between the B_1 and A_1 equilibrium geometry; at $k = 0$ the intersection point is in the B_1 geometry, with $k = 1$ the A_1 geometry. The intersection point of the 1A_2 and the 1B_1 states was found to lie close to the equilibrium of the 1B_1 state ($k = 0.15 - 0.18$), and only $115\text{-}155 \text{ cm}^{-1}$ above the minimum of the potential energy surface of the 1B_1 state (Fig. 4.6, Table 4.6).

4.2.6 Conclusion

The absorption spectrum of a vibronic band within the \tilde{A}^1A_2 - \tilde{X}^1A_1 electronic transition for the short cumulene carbene C_3H_2 was rotationally resolved by cw-CRD absorption spectroscopy. A conventional rotational Hamiltonian for an asymmetric top without centrifugal distortion terms was used to analyze the data. A least-square fit for the 86 lines gave accurate rotational constants for the excited state. The geometrical relation between the 1B_1 and 1A_1 states was demonstrated by the *ab initio* calculations. Furthermore, the effective molecular structure of the upper state was calculated using the obtained rotational constants.

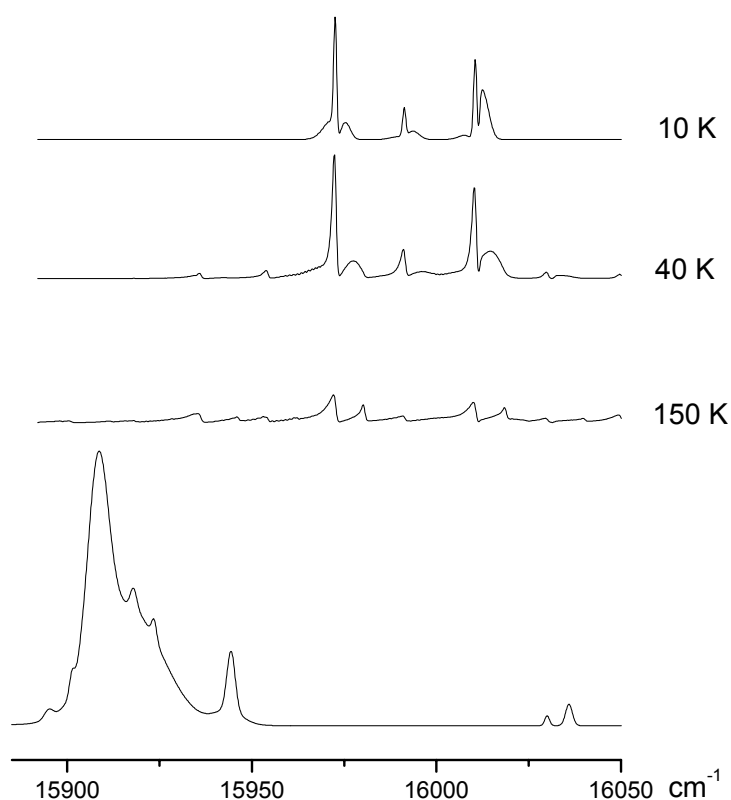


Figure 4.7 Diffuse interstellar bands in the 628 nm region (lowest trace) taken from ref. 33 and the simulated C_3H_2 spectrum obtained using the independent Boltzmann population model for 10, 40 and 150 K (upper three traces) using 0.2 cm^{-1} (FWHM) for the rotational lines.

The optical spectrum obtained allows a comparison with the list of diffuse interstellar band positions [55]. Using the determined spectroscopic constants, the absorption spectrum of the C_3H_2 was predicted at the three temperatures 10, 40 and 150 K with resolution typical in astronomical measurements $\sim 0.2 \text{ cm}^{-1}$. This is shown in fig. 4.7. As can be seen there are no DIB's seen at these wavelengths. However, it should be pointed out that the transition being compared has a small oscillator strength (vibronically induced transition) and thus any corresponding DIB would be very weak. Clearly a better comparison will be with the origin band of the $\tilde{B}^1B_1 \leftarrow \tilde{X}^1A_1$ system near 609 nm once this has been measured in the gas phase.

Table 4.5 Molecular structure and rotational constants of C₃H₂^a

State	Method	Bond length (Å)				Angle (°)	<i>A</i>	<i>B</i>	<i>C</i>
		C1–C2	C2–C3	C1–C3	C3–H	C2–C3–H	(cm ⁻¹)	(cm ⁻¹)	(cm ⁻¹)
<i>X</i> ¹ A ₁	Experimental ^b	1.291	1.324	2.615	1.098	118.8	9.6328(11) ^c	0.353198(67) ^c	0.340367(67) ^c
	RSPT3, CAS10	1.290	1.330	2.620	1.085	121.35	9.744	0.351	0.339
<i>A</i> ¹ A ₂	Experimental ^d	1.28707(79)	1.324 ^e	2.61107(79)	1.098 ^e	121.9969(12)	9.83717(46)	0.341217(86)	0.328764(91)
	RSPT3, CAS10	1.321	1.367	2.688	1.082	120.34	9.597	0.335	0.324
<i>B</i> ¹ B ₁	RSPT3, CAS10	1.213	1.429	2.642	1.077	119.96	9.598	0.345	0.333

^a Values in parentheses denote the standard deviation and apply to the last digits of the

^b Constants from Ref. [36].

^c Constants from Ref. [26].

^d This work.

^e Fixed to the value of Ref. [36].

Table 4.6 Computed relative energies for the 1A_2 , 1B_1 and intersection point, and the geometry of the intersection point.

Method	$E(^1B_1) - E(^1A_2)^a$	$E_{\text{intersect.}} - E(^1B_1)^b$	k^c	Bond length [\AA]			Angle [$^\circ$]
	(cm^{-1})	(cm^{-1})	%	C1-C2	C2-C3	C3-H	C2-C3-H
RSPT3, CAS10	-1180(-0.146 eV)	115	15.2%	1.229	1.420	1.078	120.02
RSPT3, CAS6	-1360(-0.168)	155	17.9%	1.232	1.421	1.077	119.97
MRCI+D, CAS6	-1240(-0.154)	130	16.6%	1.234	1.420	1.078	119.97

^a Energy difference of the 1B_1 and 1A_2 states at the equilibrium geometry of the 1B_1 state.

^b Energy difference of the 1B_1 and intersection point.

^c The parameter k is defined by the relation: (geometry of the intersection point) = (1B_1 equilibrium geometry) + $k \times \Delta_{\text{geo}}$.

References

- [1] M. Guelin, J. Cernicharo, M.J. Travers, M.C. McCarthy, C.A. Gottlieb, P. Thaddeus, M. Ohishi, S. Saito, S. Yamamoto, *Astron. Astrophys.* **317**, (1997), L1.
- [2] M.B. Bell, P.A. Feldman, J.K.G. Watson, M.C. McCarthy, M.J. Travers, C.A. Gottlieb, P. Thaddeus, *Astrophys. J.* **518**, (1999), 740.
- [3] B.E. Turner, E. Herbst, R. Terzieva, *Astrophys. J., Suppl. Ser.* **126**, (2000), 427.
- [4] M.C. McCarthy, M.J. Travers, A. Kovacs, C.A. Gottlieb, P. Thaddeus, *Astrophys. J., Suppl. Ser.* **113**, (1997), 105.
- [5] C.A. Gottlieb, M.C. McCarthy, M.J. Travers, J.U. Grabow, P. Thaddeus, *J. Chem. Phys.* **109**, (1998), 5433.
- [6] P. Freivogel, J. Fulara, M. Jakobi, D. Forney, J.P. Maier, *J. Chem. Phys.* **103**, (1995), 54.
- [7] H. Ding, T. Pino, F. Guthe, J.P. Maier, *J. Chem. Phys.* **117**, (2002), 8362.
- [8] H. Linnartz, T. Motylewski, O. Vaizert, J.P. Maier, A.J. Apponi, M.C. McCarthy, C.A. Gottlieb, P. Thaddeus, *J. Mol. Spectrosc.* **197**, (1999), 1.
- [9] D. Pfluger, T. Motylewski, H. Linnartz, W.E. Sinclair, J.P. Maier, *Chem. Phys. Lett.* **329**, (2000), 29.
- [10] W.E. Sinclair, D. Pfluger, D. Verdes, J.P. Maier, *J. Chem. Phys.* **112**, (2000), 8899.
- [11] H. Linnartz, D. Pfluger, O. Vaizert, P. Cias, P. Birza, D. Khoroshev, J.P. Maier, *J. Chem. Phys.* **116**, (2002), 924.
- [12] P. Birza, T. Motylewski, D. Khoroshev, A. Chirokolava, H. Linnartz, J.P. Maier, *Chem. Phys.* **283**, (2002), 119.
- [13] H. Linnartz, T. Motylewski, J.P. Maier, *J. Chem. Phys.* **109**, (1998), 3819.
- [14] M. Hippler, M. Quack, *Chem. Phys. Lett.* **314**, (1999), 273.
- [15] A.L. Sobolewski, L. Adamowicz, *J. Chem. Phys.* **102**, (1995), 394.
- [16] J.P. Maier, *J. Phys. Chem. A* **102**, (1998), 3462.
- [17] P. Freivogel, Ph.D. dissertation, University of Basel, Basel, (1997).

- [18] K. Hoshina, H. Kohguchi, Y. Ohshima, Y. Endo, *J. Chem. Phys.* **108**, (1998), 3465.
- [19] T.R. Taylor, C. Xu, D.M. Neumark, *J. Chem. Phys.* **108**, (1998), 10018.
- [20] J. Myung Lee, L. Adamowicz, *Spectrochim. Acta, Part A* **57A**, (2001), 897.
- [21] Z. Cao, S.D. Peyerimhoff, *Phys. Chem. Chem. Phys.* **3**, (2001), 1403.
- [22] A.E. Douglas, *Nature* **269**, (1977), 130.
- [23] P. Thaddeus, M. C. McCarthy, M. J. Travers, C. A. Gottlieb, W. Chen, *Faraday Discussions* **109**, (1998), 121.
- [24] W. D. Langer, T. Velusamy, T. B. H. Kuiper, R. Peng, M. C. McCarthy, M. J. Travers, A. Kovacs, C. A. Gottlieb, P. Thaddeus, *Astrophys. J.* **480**, (1997), L63.
- [25] G. Maier, H. P. Reisenauer, W. Schwab, P. Carsky, B. A. Hess, L. J. Schaad, *J. Am. Chem. Soc.* **109**, (1987), 5183.
- [26] J. M. Vrtilik, C. A. Gottlieb, E. W. Gottlieb, T. C. Killian, P. Thaddeus, *Astrophys. J.* **364**, (1990), L53.
- [27] J. Cernicharo, C. A. Gottlieb, M. Guelin, T. C. Killian, G. Paubert, P. Thaddeus, J. M. Vrtilik, *Astrophys. J.* **368**, (1991), L39.
- [28] P. Thaddeus, C. A. Gottlieb, R. Mollaaghbabab, J. M. Vrtilik, *J. Chem. Soc., Faraday Trans.* **89**, (1993), 2125.
- [29] R. A. Seburg, E. V. Patterson, J. F. Stanton, R. J. McMahon, *J. Am. Chem. Soc.* **119**, (1997), 5847.
- [30] J. F. Stanton, J. T. Depinto, R. A. Seburg, J. A. Hodges, R. J. McMahon, *J. Am. Chem. Soc.* **119**, (1997), 429.
- [31] J. A. Hodges, R. J. McMahon, J. F. Stanton, K. W. Sattelmeyer, *Astrophys. J.* **544**, (2000), 838.
- [32] P. Hall, D. A. Williams, *Astrophys. Space Sci.* **229**, (1995), 49.
- [33] R. P. A. Bettens, E. Herbst, *Astrophys. J.* **468**, (1996), 686.
- [34] S. D. Taylor, W. W. Duley, *Mon. Not. R. Astron. Soc.* **286**, (1997), 344.
- [35] G. Fischer, J. P. Maier, *Chem. Phys.* **223**, (1997), 149.
- [36] C. A. Gottlieb, T. C. Killian, P. Thaddeus, P. Botschwina, J. Fluegge, M. Oswald, *J. Chem. Phys.* **98**, (1993), 4478.

- [37] C. D. Sherrill, C. G. Brandow, W. D. Allen, H. F. Schaefer, *J. Am. Chem. Soc.* **118**, (1996), 7158.
- [38] A. M. Mebel, W. M. Jackson, A. H. H. Chang, S. H. Lin, *J. Am. Chem. Soc.* **120**, (1998), 5751.
- [39] P. Birza, D. Khoroshev, A. Chirokolava, T. Motylewski, J. P. Maier, *Chem. Phys. Lett.* **382**, (2003), 245.
- [40] M. Hippler, M. Quack, *Chem. Phys. Lett.* **314**, (1999), 273.
- [41] J. T. A. K. Yamashita, *J. Chem. Phys.* **104**, (1996), 6613.
- [42] D. Luckhaus, M. Quack, *Mol. Phys.* **63**, (1989) 745-758.
- [43] MOLPRO a package of ab initio programs designed by H.J. Werner and P.J. Knowles, version 2002.1, with contribution from others, see www.molpro.net
- [44] R. Lindh, U. Ryu, B. Liu, *J. Chem. Phys.* **95**, (1991), 5889.
- [45] H.-J. Werner, *Mol. Phys.* **89**, (1996), 645.
- [46] P. Celani, H.-J. Werner, *J. Chem. Phys.* **112**, (2000), 5546.
- [47] H. J. Werner, P. J. Knowles, *J. Chem. Phys.* **89**, (1988), 5803.
- [48] P. J. Knowles, H. J. Werner, *Chem. Phys. Lett.* **145**, (1988), 514.
- [49] M. Rubio, J. Stålring, A. Bernhardsson, R. Lindh, B. O. Roos, *Theoretical Chemistry Accounts* **105**, (2000), 15.
- [50] O. Christiansen, H. Koch, P. Jørgensen, *J. Chem. Phys.* **103**, (1995), 7429.
- [51] J. F. Stanton, R. J. Bartlett, *J. Chem. Phys.* **98**, (1993), 7029.
- [52] J. Gauss, J. F. Stanton, *J. Mol. Struct.* **485-486**, (1999), 43.
- [53] C. A. Gottlieb, T. C. Killian, P. Thaddeus, P. Botschwina, J. Fluegge, M. Oswald, *J. Chem. Phys.* **98**, (1993), 4478.
- [54] W. E. Henke, H. L. Selzle, T. R. Hays, E. W. Schlag, S. H. Lin, *J. Chem. Phys.* **76**, (1982), 1327-1334
- [55] P. Jenniskens, F. -X Desert, *Astron. & Astrophys, Supplement Series*, **106**, (1994), 39-78.

Appendix 1 Sensitivity

After the first pass through the CRD, the laser pulse initial intensity I_{in} , is attenuated to $I_0 = T^2 \exp(-\alpha l) I_{in}$, where T is the mirror transmittivity, α is the frequency dependent absorption coefficient of the gas sample inside the cell, and l is the cell length. For each subsequent round trip, the intensity decreases by an additional factor $R^2 \exp(-2\alpha l)$, where R is the reflectivity of the mirrors. Therefore, after n round trips, the pulse intensity at the PD is $I_n = [R \times \exp(-\alpha l)]^{2n} I_0$. Diffraction losses and Rayleigh scattering by the gas can be included in the mirror losses L , which are linked to the transmittivity and the reflectivity by the conservation of energy $T+L+R=1$. For very high quality dielectric mirrors $L \approx T < 100$ ppm. Therefore

$$I_n = I_0 \exp[2n(\ln R - \alpha l)] \approx I_0 \exp[-2n(T+L+\alpha l)]$$

Since the PD output signal is filtered with a time constant that gives only the intensity envelope of the pulse train, we can change from the discrete variable n to the continuous time variable $t = 2nl/c$,

$$I(t) = I_0 \exp\left(\frac{t}{\tau} - c\alpha t\right)$$

where we introduced the empty cavity decay time $\tau = l/c(T+L)$.

The experimental noise level of the signal S is $2\sigma_s \sim 0.005$. Incidentally, if it is considered that this noise is due mostly to the integration over window A (where the decay signal is much weaker), then this figure means that we are able to observe a 1% variation in A ,

$$2\sigma_s = \left| \frac{\partial S}{\partial A} \right| 2\sigma_A = \frac{2\sigma_A}{A} = 0.5\%$$

The sensitivity limit is obtained dividing σ_s by the effective path length

$$2\sigma \approx \frac{0.005}{1 \text{ km}} \approx 5 \times 10^{-8} / \text{cm} \times 32 \text{ cm} / \text{round} \cdot \text{trip} = 1.6 \times 10^{-6} / \text{round trip}$$

i.e. 0.016 ppm per round trip.

Appendix 2 Shot noise limit

Here, the decay signal is digitized in a time interval $[0, T]$ and then its logarithm is least squares fitted to a straight line to extract the slope $a = -1/\tau$. In the following, instead of summing over data points, it will be convenient to use integrals. The signal is in this case $S(t) = \ln I(t) = \ln I_0 - t/\tau$ with a noise level $\sigma_s^2(t) = (\partial S / \partial I)^2 \sigma_I^2(t) = 1/I(t)$.

The least-squares fit involves minimizing

$$F(a, b) = \int_0^T [S(t) - at - b]^2 dt$$

with respect to a and b , from which

$$a = \frac{12}{T^3} \int_0^T t S(t) dt - \frac{6}{T^2} \int_0^T S(t) dt \rightarrow \frac{\partial a}{\partial S(t)} = \frac{12}{T^3} t - \frac{6}{T^2}$$

This allows us to calculate the noise level of a ,

$$\begin{aligned} \sigma_a^2(T) &= \int_0^T \left[\frac{\partial a}{\partial S(t)} \right]^2 \sigma_s^2(t) dt \\ &= \frac{36}{I_0 \tau^3} \frac{(x^2 - 4x + 8)e^x - x^2 - 4x - 8}{x^6}, \end{aligned}$$

$$x = \frac{T}{\tau},$$

which should be minimized to find the optimal experimental conditions

$$T_{\min} \cong 3.52\tau \rightarrow \left. \frac{\sigma_a}{a} \right|_{\min} = \left. \frac{\sigma_s}{S} \right|_{\min} = \frac{1.84}{\sqrt{I_0 \tau}}$$

It might seem puzzling that T_{\min} is actually finite. This implies that one should record and fit only a finite portion of the ring-down decay signal. The problem is that a nonweighted least squares fit is used here, and the shot noise on the logarithm of the ring-down signal increases exponentially with T . If all times are equally weighted, then the fit becomes more and more affected by the shot noise as T is increased beyond T_{\min} .

Observed spectroscopic transitions

What happens if the fit to $S(t)$ is weighted with the inverse square of the shot noise? We find that in this case, the minimum noise occurs for $T \rightarrow \infty$,

$$\frac{\sigma_\tau}{\tau} = \frac{1}{\sqrt{I_0 \tau}}$$

The experimental initial intensity $I_{in}=5.2 \mu\text{W}$. From here we can estimate

$$I_0(\text{photon/sec}) = I_{in} / \left(\frac{2\pi c}{\lambda} h \right) = 1.66 \times 10^{12} \text{ photon/sec}$$

In this case we can estimate the relative noise:

$$\frac{\sigma_\tau}{\tau} = \frac{1}{\sqrt{I_0 \tau}} = \frac{1}{\sqrt{1.66 \times 10^{12} \times 7 \times 10^{-6}}} = 0.00029$$

Chapter 5 Concluding remarks and outlook

This chapter briefly summarizes general aspects of the results obtained. In particular, a comparison is made between the results for HC_6H^+ obtained before and after a series of improvements concerning the source and data acquisition program. With these modifications, we achieved higher resolution and a better S/N ratio. Conclusions concerning the cw-CRD spectrometer are not repeated here but can be found in the relevant sections. Finally, the outlook for future investigations is presented.

5.1 Concluding remarks

The initial measurement of the $A^2\Pi_g \leftarrow X^2\Pi_u$ ($\Omega=3/2$) transition of HC_6H^+ gave results comparable to data obtained with the frequency modulation method (one of the most sensitive methods at that time), with a resolution of about 500 MHz and high sensitivity ($\sim 10^{-6} \text{ cm}^{-1}$). Modifications of the spectrometer were then carried out. The discharge source was built with a multi-channel body which permitted a reduction of Doppler broadening. A new algorithm was used for fitting the ring down and two new data acquisition cards were used to improve control of the conditions. The spectrum of C_3H_2 , recorded after these modifications, showed very high resolution (around 350 MHz) and a lowest detection limit of approximately 10^6 cm^{-3} . The signal/noise ratio was improved by a factor of 2.5, giving a S/N ratio of 50 for C_3H_2 . In addition, the sensitivity was increased by a factor of 10, to around 10^{-7} cm^{-1} .

Such changes will enable further studies of new and exciting species of astrophysical interest.

5.2 Outlook

The results described in this thesis demonstrate that the cw-CRD spectrometer is a very powerful tool for gas phase spectroscopy measurements. With the present experimental setup, it is now possible to acquire high-resolution spectra of the best possible quality. With these developments we have made a new step towards studies of transient molecules in the gas phase and future investigations will continue in this direction.

The search for new and interesting transitions is now possible following the extension of the scanning range to the ultraviolet region, achieved by doubling the laser wavelength. In addition, the data acquisition system has been upgraded and improved, allowing more precise data fitting and evaluation.

Further modifications can still be introduced into the experimental setup. Firstly, different ion sources may be implemented in the present apparatus, including ones based on laser desorption-ionization and electrospray ionization. Additionally, a photomultiplier could be used instead of a photodiode, to increase the acquisition speed. More efficient data fitting procedures can also be envisaged, to account for different statistical weights of the collected data.

5.3 Publication in journals during Ph. D. studies

Rotationally resolved $A^2\Pi_u \leftarrow X^2\Pi_g$ electronic transition of NC_6N^+

H. Linnartz,^{a)} D. Pfluger, O. Vaizert, P. Cias, P. Birza, D. Khoroshev, and J. P. Maier
Institute for Physical Chemistry, Klingelbergstrasse 80, CH-4056 Basel, Switzerland

(Received 17 August 2001; accepted 23 October 2001)

The rotationally resolved $A^2\Pi_u \leftarrow X^2\Pi_g$ electronic origin band spectrum of dicyanodiacetylene cation, NC_6N^+ , has been recorded in the gas phase using frequency-production double modulation spectroscopy in a liquid nitrogen cooled hollow cathode discharge and cavity ring down spectroscopy in a supersonic plasma. The analysis of the complementary results provides accurate molecular parameters for the two spin-orbit components in both electronic states. © 2002 American Institute of Physics. [DOI: 10.1063/1.1427710]

I. INTRODUCTION

In recent years several cyanopolyacetylene radicals (HC_nN) have been studied by Fourier transform microwave spectroscopy^{1,2} and, following their laboratory detection, species as large as HC_{11}N have been identified by radio astronomy in the interstellar medium.³ The dicyano derivatives (NC_nN) may be comparably abundant in space, but are unsuitable for microwave detection due to absence of a dipole moment. In this case accurate spectroscopic information can be obtained from high resolution studies of vibrational or electronic transitions in the gas phase. The latter are available for a series of carbon chain radicals. Examples are the nonpolar NC_5N (Ref. 4) and HC_7H ,^{5,6} as well as chains that were already detected in dense interstellar clouds such as HC_6N (Ref. 6) and C_6H .⁷ These species are formed in ion-molecule reactions and consequently spectroscopic information on carbon chain ions is needed as well, but high resolution data are rare and pure rotational spectra are limited to a few species.⁸

This is particularly true for the (di)cyanopolyacetylene cations. Electronic spectra have been recorded in neon matrices for NC_{2n}N^+ ($n=2-6$) and $\text{HC}_{2n+1}\text{N}^+$ ($n=2-6$).⁹⁻¹² Following these and low resolution emission studies¹³⁻¹⁵ the rotationally resolved electronic gas phase spectrum of the cyanodiacetylene (HC_5N^+) and dicyanoacetylene (NC_4N^+)¹⁶ as well as the cyanotriacetylene (HC_7N^+)¹⁷ were reported. In the present work the rotationally resolved spectrum of the next larger member in the dicyano-series, NC_6N^+ , is presented. The results are compared with the results of density functional theory calculations¹⁸ and the spectroscopic parameters available for the iso-electronic chains HC_7N^+ (Ref. 17) and HC_8H^+ .¹⁹

II. EXPERIMENT

The spectra are recorded using two complementary experimental approaches. These are frequency production double modulation (FPM) spectroscopy of a static plasma generated in a discharge cell ($T_{\text{rot}} \sim 150$ K) and cavity ring-down (CRD) spectroscopy sampling a supersonic planar

plasma ($T_{\text{rot}} = 15$ K), yielding spectra with significantly different rotational profiles. Both experimental techniques have been described. In the FPM experiment²⁰ mixtures of 0.5%–0.6% cyanogen/He are discharged in a liquid nitrogen cooled hollow cathode incorporated into a White-type multiple reflection cell ($L_{\text{tot}} \sim 100$ m). Production modulation is obtained by applying a rectified 17 kHz ac voltage (–500 to 700 V). The laser beam is electro-optically modulated at a radio frequency of 192 MHz and detected by a fast photodiode. Subsequent phase sensitive demodulation of the high frequency portion of the signal during a production cycle gives absorption bands that have a derivativelike shape. The resolution is Doppler limited and typically of the order of 550 MHz.

In the CRD setup²¹ the NC_6N^+ radicals are formed by a discharge through a high pressure gas pulse (typically 100 mA at –1000 V for a 12 bar backing pressure) of an 0.2% cyanogen/He mixture in the throat of a 3 cm × 300 μm multilayer slit nozzle device. A standard CRD spectrometer is used to detect the signals in direct absorption. The resolution is limited by the bandwidth of the laser to ~ 0.035 cm^{-1} . In both experiments iodine spectra are used for an absolute frequency calibration.

III. RESULTS AND DISCUSSION

An overview scan of the $A^2\Pi_u \leftarrow X^2\Pi_g$ electronic origin band transition of NC_6N^+ recorded by FPM in the discharge cell is shown in Fig. 1. In the range 15 240–15 248 cm^{-1} approximately 200 individual absorption lines are resolved. These transitions belong to the P -, Q - and R -branches of two subbands corresponding to the parallel $A^2\Pi_{3/2} \leftarrow X^2\Pi_{3/2}$ and $A^2\Pi_{1/2} \leftarrow X^2\Pi_{1/2}$ electronic transitions. The intensity ratio of the two bands is determined by the “spin-orbit temperature” and the value of the spin-orbit splitting (A'') in the ground state. The latter is estimated from previous studies to be of the order of $-40(5)$ cm^{-1} ,¹⁶ the minus indicating that the $\Omega = \frac{3}{2}$ spin-orbit component is lower in energy than the $\Omega = \frac{1}{2}$. At the high ambient temperature in the cell both spin-orbit components are equally intense. The rotational population is distributed over many levels and the intensity of both Q -branches and transitions starting from low J -levels is low. Clear band heads, however, are missing. Moreover, the spin-

^{a)}Electronic mail: Henricus.Linnartz@unibas.ch

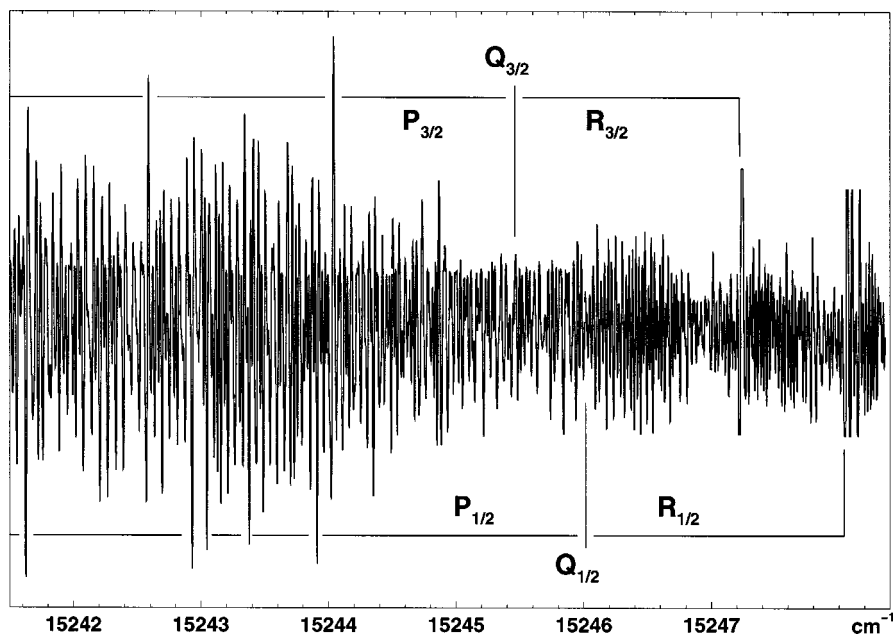


FIG. 1. Rotationally resolved frequency production double modulation absorption spectrum of the $A^2\Pi_u \leftarrow X^2\Pi_g$ electronic origin band of NC_6N^+ measured in a liquid-nitrogen cooled hollow cathode discharge ($T_{\text{rot}} \sim 150$ K). The P -, Q - and R -branches of the $A^2\Pi_{3/2} \leftarrow X^2\Pi_{3/2}$ and $A^2\Pi_{1/2} \leftarrow X^2\Pi_{1/2}$ subbands are indicated.

orbit components overlap as the difference in spin-orbit splittings in ground and excited state, ΔA , appears to be small. All these factors together lead to ambiguity in the assignment of the rotational lines. What is missing is a clearly defined starting point. This is provided by the jet spectrum.

In Fig. 2 part of the spectral region of Fig. 1 is shown. The spectrum is recorded by CRD in the plasma expansion. Only the lower subband, $A^2\Pi_{3/2} \leftarrow X^2\Pi_{3/2}$, is clearly visible now, as the population of the upper spin-orbit component is low. Besides unresolved P - and R -branches,²² a clear Q -branch is observed starting at $15245.46(3)$ cm^{-1} . This branch is not visible in Fig. 1, but the CRD position allows the assignment of transitions belonging to the $A^2\Pi_{3/2} \leftarrow X^2\Pi_{3/2}$ subband within ± 1 J quantum numbering in the FPM spectrum. The band gap is $\sim 10B$ [with $B \sim 0.019$ cm^{-1} (Ref. 18)] reflecting that the lowest rotational transitions cor-

respond to $P(\frac{5}{2})$ and $R(\frac{3}{2})$. Adjacent transitions are separated by $\sim 2B$. In this way more than 80(40) transitions have been assigned in $P(R)$ -branch of the $A^2\Pi_{3/2} \leftarrow X^2\Pi_{3/2}$ band with J -values up to 90.5.²³ These values are then fitted with PGopher²⁴ using ν_0 , B''_0 , B'_0 , D''_0 and D'_0 as variables yielding a rms of 0.002 cm^{-1} . The resulting constants are listed in Table I. The value for $B''_0 = 0.0187533(55)$ cm^{-1} is close to the B_e -value of 0.01867 cm^{-1} as obtained from density functional calculations.¹⁸ A simulation using these constants proves that the stronger feature in Fig. 1 at $15247.23(3)$ cm^{-1} corresponds to the R -branch band head of the $A^2\Pi_{3/2} \leftarrow X^2\Pi_{3/2}$ system. A similar feature is observed at 15247.85 cm^{-1} and is tentatively assigned to the R -branch band head of the second spin-orbit system.

The lines that are left over are mainly due to the $\Omega = \frac{1}{2}$

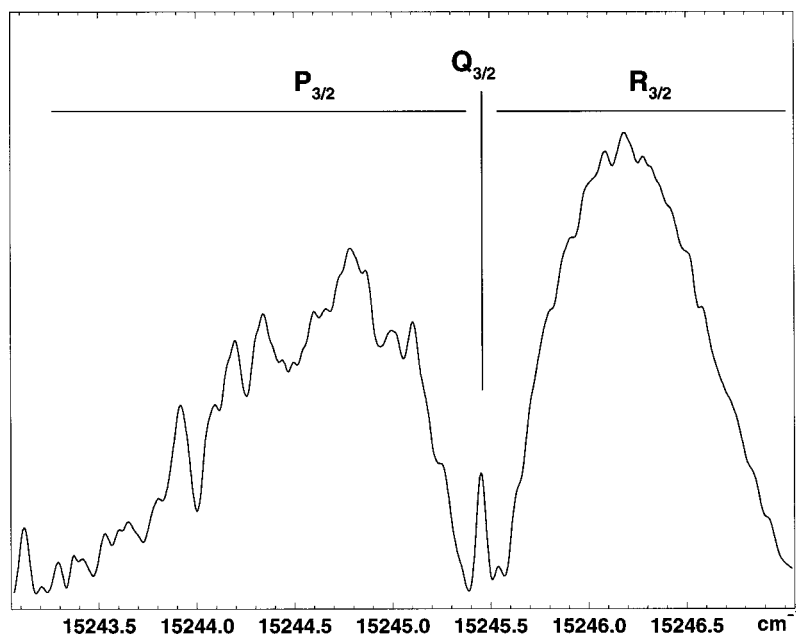


FIG. 2. Cavity ring down absorption spectrum of the $A^2\Pi_{3/2} \leftarrow X^2\Pi_{3/2}$ electronic origin band of NC_6N^+ , recorded through a supersonic plasma. The second spin-orbit component is not visible at the low temperature in the jet ($T_{\text{rot}} \sim 15$ K). The Q -branch position is used to assign the FPM spectrum.

TABLE I. Molecular constants (in cm^{-1}) for the $A^2\Pi_{3/2}-X^2\Pi_{3/2}$ and for the $A^2\Pi_{1/2}-X^2\Pi_{1/2}$ electronic origin band transition of NC_6N^+ . The molecular parameters for the $A^2\Pi_u-X^2\Pi_g$ electronic origin band transition of the iso-electronic HC_7N^+ (Ref. 17) and HC_8H^+ (Ref. 19) species are listed for comparison.

	NC_6N^+		HC_7N^+	HC_8H^+
	$\Omega=3/2$	$\Omega=1/2$	$\Omega=3/2$	$\Omega=3/2$ and $1/2$
B_0''	0.018 753 3(55)	0.018 707(19)	0.018 966 5(71)	0.019 077 9(93)
D_0''	$6.7(15)\cdot 10^{-9}$	$6.2(38)\cdot 10^{-9}$		
B_0'	0.018 558 5(56)	0.018 565(19)	0.018 773 1(72)	0.018 867 3(94)
D_0'	$7.1(16)\cdot 10^{-9}$	$8.3(39)\cdot 10^{-9}$		
ΔB	-0.00019	-0.00014	-0.00019	-0.00021
ΔA	+ 0.56		-2.04	-3.00
ν_0	15 245.737(1)		14 925.423(4)	14 143.1815(5)

component. The rotational assignment is problematic now as information on the Q -branch of the $A^2\Pi_{1/2}-X^2\Pi_{1/2}$ band is missing. The difference between the band heads, however, indicates that the $Q_{1/2}$ -branch is expected around $15\,246.1\text{ cm}^{-1}$. In addition, only minor differences between the rotational constants for the two spin-orbit systems are expected. In previous studies transitions originating from different spin-orbit components were fitted with one single set of rotational parameters.^{7,16,19} In the present experiment this turns out not to be possible. However, as long as the effect of spin uncoupling is small, i.e., $2BJ \ll |A|$, B is best replaced by effective parameters $B_{\text{eff}}(^2\Pi_{1/2})$ and $B_{\text{eff}}(^2\Pi_{3/2})$. In second order perturbation theory the difference ΔB_{eff} is given by

$$\Delta B_{\text{eff}} = \frac{2B^2}{\bar{A}}, \quad (1)$$

where $\bar{A} = A - 2B$.²⁵ \bar{A} is expected to be of the order of $-40(5)\text{ cm}^{-1}$ (Ref. 16) which puts an additional constraint to the fit. The line positions and most likely assignment for

transitions belonging to the $A^2\Pi_{1/2}-X^2\Pi_{1/2}$ system are available from (Ref. 26). The resulting molecular parameters are given in Table I. The quality of the fit will be worse as only a few transitions share a common level (rms $\sim 0.004\text{ cm}^{-1}$).²⁶ Nevertheless, using Eq. (1) an A'' -value between -15 and -32 cm^{-1} is calculated.²⁷ The simulation confirms that the band head position coincides with the feature at $15\,247.85\text{ cm}^{-1}$.

The spectral features of NC_6N^+ are expected to be qualitatively similar to those of the iso-electronic cyanotriacetylene cation¹⁷ and tetraacetylene cation.¹⁹ The molecular parameters of the $A^2\Pi_u-X^2\Pi_g$ electronic origin bands of these two ions are listed in Table I as well. These bands are shifted to lower energy, by 320 cm^{-1} for HC_7N^+ and by 1103 cm^{-1} for HC_8H^+ . The ΔA value of HC_7N^+ (-2.04 cm^{-1}) is comparable to that of HC_8H^+ (-3.00 cm^{-1}), but the corresponding value for NC_6N^+ is significantly smaller and, moreover, is positive ($+0.56\text{ cm}^{-1}$). This value, however, is very close to the $\Delta A = +0.53\text{ cm}^{-1}$ found for NC_4N^+ .¹⁶ There it was concluded that this anomaly is due to a spin-orbit induced interaction of the upper $A^2\Pi_{1/2}$ electronic state with another low lying electronic state, presumably of $^2\Sigma$ character, whereas the $A^2\Pi_{3/2}$ state is not affected. This becomes clear from the different values for $\Delta B = B_0' - B_0''$: for the $\Omega = \frac{3}{2}$ component a value of $0.000\,19\text{ cm}^{-1}$ is found, similar to the values determined for HC_7N^+ ($0.000\,19\text{ cm}^{-1}$) and HC_8H^+ ($0.000\,21\text{ cm}^{-1}$), but for $\Omega = \frac{1}{2}$ the value decreases to $0.000\,14\text{ cm}^{-1}$. The second-order spin-orbit contribution to the rotational constant for a Π state is given by^{28,29}

$$B^{(2)} = \sum_{n \neq 0} \frac{4B^2}{E_0^0 - E_n^0}. \quad (2)$$

With $|\Delta E| = 40\text{ cm}^{-1}$ this gives $B^{(2)} \sim 0.000\,04\text{ cm}^{-1}$, i.e., an unperturbed value for ΔB of $0.000\,18\text{ cm}^{-1}$, close to the value of the other spin-orbit component.

In the case of NC_4N^+ it was also found that the $^2\Sigma-^2\Pi$ interaction removes the degeneracy of the e - and

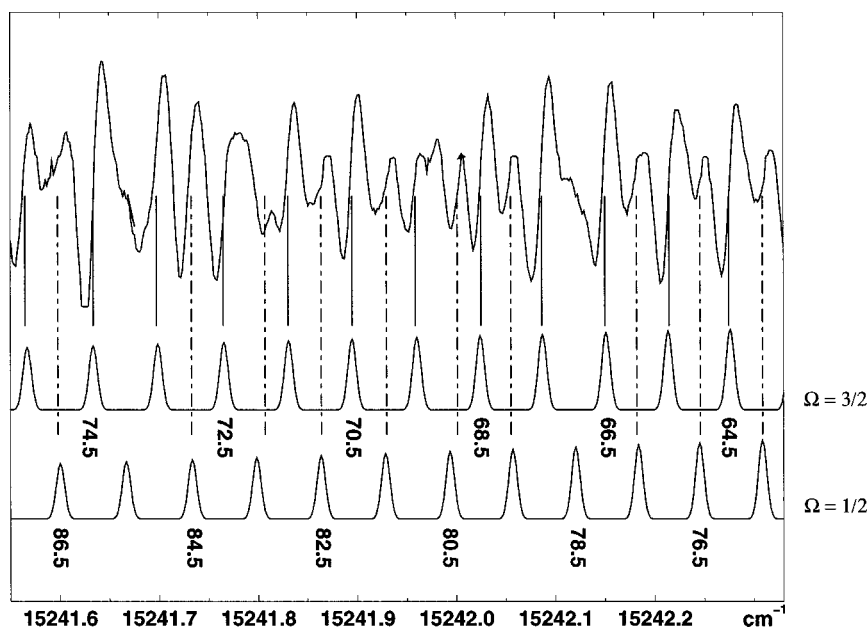


FIG. 3. High J -level transitions with their typical $1f$ derivative line shapes recorded in the FPM experiment. The simulated spectrum is shown for both spin-orbit components. There is no evidence for Λ -doubling (see the text).

f -symmetry, resulting in a resolvable Λ -doubling. This effect is not observed here. In Fig. 3 part of the P -branch range for high J -levels in both spin-orbit components is shown. The simulated spectrum is given as well. Clearly, there is no evidence for Λ -doubling within the experimental resolution: the size of the splitting would have been J -dependent and the expected 2:1 spin-statistical alternation is lacking. This is also expected: the rotational constant of NC_6N^+ is 2.5 times smaller than that of NC_4N^+ ($\sim 0.044 \text{ cm}^{-1}$) and since the Λ -type doubling constants p and q are proportional to B and B^2 , respectively, splittings will be considerably smaller.

ACKNOWLEDGMENTS

This work has been supported by the Swiss National Science Foundation, Project No. 20-63459.00. One of the authors (H.L.) also acknowledges support from FOM (Fundamenteel Onderzoek der Materie).

- ¹M. C. McCarthy, J. U. Grabow, M. J. Travers, W. Chen, C. A. Gottlieb, and P. Thaddeus, *Astrophys. J.* **494**, L231 (1998).
- ²M. C. McCarthy and P. Thaddeus, *Chem. Soc. Rev.* **30**, 177 (2001).
- ³M. B. Bell, P. A. Feldman, M. J. Travers, M. C. McCarthy, C. A. Gottlieb, and P. Thaddeus, *Astrophys. J.* **483**, L61 (1997).
- ⁴H. Linnartz, O. Vaizert, P. Cias, L. Grüter, and J. P. Maier, *Chem. Phys. Lett.* **345**, 89 (2001).
- ⁵C. D. Ball, M. C. McCarthy, and P. Thaddeus, *J. Chem. Phys.* **112**, 10149 (2000).
- ⁶O. Vaizert, T. Motylewski, M. Wyss, E. Riaplov, H. Linnartz, and J. P. Maier, *J. Chem. Phys.* **114**, 7918 (2001).
- ⁷H. Linnartz, T. Motylewski, O. Vaizert, J. P. Maier, A. J. Apponi, M. C. McCarthy, C. A. Gottlieb, and P. Thaddeus, *J. Mol. Spectrosc.* **197**, 1 (1999).
- ⁸C. A. Gottlieb, A. J. Apponi, M. C. McCarthy, P. Thaddeus, and H. Linnartz, *J. Chem. Phys.* **113**, 1910 (2000).

- ⁹J. Agreiter, A. M. Smith, M. Härtle, and V. Bondybey, *Chem. Phys. Lett.* **225**, 87 (1994).
- ¹⁰D. Forney, P. Freivogel, J. Fulara, and J. P. Maier, *J. Phys. Chem.* **102**, 1510 (1995).
- ¹¹J. Agreiter, A. M. Smith, and V. Bondybey, *Chem. Phys. Lett.* **241**, 317 (1995).
- ¹²A. M. Smith, J. Agreiter, and V. Bondybey, *Chem. Phys. Lett.* **244**, 379 (1995).
- ¹³E. Kloster-Jensen, J. P. Maier, O. Marthaler, and M. Mohraz, *J. Chem. Phys.* **71**, 3125 (1979).
- ¹⁴G. Bieri, E. Kloster-Jensen, S. Kvisle, J. P. Maier, and O. Mathaler, *J. Chem. Soc., Faraday Trans.* **76**, 676 (1980).
- ¹⁵J. P. Maier, L. Misev, and F. Thommen, *J. Phys. Chem.* **86**, 54 (1982).
- ¹⁶W. E. Sinclair, D. Pfluger, and J. P. Maier, *J. Chem. Phys.* **111**, 9600 (1999).
- ¹⁷W. E. Sinclair, D. Pfluger, D. Verdes, and J. P. Maier, *J. Chem. Phys.* **112**, 8899 (2000).
- ¹⁸S. Lee, *J. Phys. Chem.* **100**, 13959 (1996).
- ¹⁹D. Pfluger, T. Motylewski, H. Linnartz, W. E. Sinclair, and J. P. Maier, *Chem. Phys. Lett.* **329**, 29 (2000).
- ²⁰W. E. Sinclair, D. Pfluger, H. Linnartz, and J. P. Maier, *J. Chem. Phys.* **110**, 296 (2000).
- ²¹T. Motylewski and H. Linnartz, *Rev. Sci. Instrum.* **70**, 1305 (1999).
- ²²No rotational resolution has been obtained, presumably because of residual Doppler broadening.
- ²³See EPAPS Document No. E-JCPSA6-116-004204 for a list with line positions and observed-calculated values. This document may be retrieved via the EPAPS homepage (<http://www.aip.org/pubserv/epaps.html>) or from <ftp.aip.org> in the director /epaps/. See the EPAPS homepage for more information.
- ²⁴C. M. Western, School of Chemistry, University of Bristol, UK, PGOPHER, 1994 and 1998.
- ²⁵H. W. Kroto, *Molecular Rotation Spectra* (Wiley, New York, 1975), p. 232.
- ²⁶See Ref. 23.
- ²⁷Shifting the rotational assignment by $\pm 1 J$ gives values of -7 and -115 cm^{-1} .
- ²⁸J. H. van Vleck, *Rev. Mod. Phys.* **23**, 213 (1951).
- ²⁹R. F. Curl, *Mod. Phys.* **9**, 585 (1965).

Cw cavity ring down spectroscopy in a pulsed planar plasma expansion

P. Birza, T. Motylewski, D. Khoroshev, A. Chirokolava, H. Linnartz, J.P. Maier*

Institute for Physical Chemistry, University of Basel, Klingelbergstrasse 80, CH-4056 Basel, Switzerland

Received 24 January 2002; accepted 15 February 2002

Abstract

A cw cavity ring down spectrometer has been constructed with the aim to record electronic spectra of rotationally cold carbon chain radicals at high spectral resolution in direct absorption. The radicals are generated in a discharge of a high pressure gas pulse of acetylene in helium in a multilayer slit nozzle. A passive cavity mode locking scheme is used to handle refractive index changes inside the cavity caused by gas pulse and plasma fluctuations. The performance is demonstrated on the rotationally resolved origin band spectrum of the $A^2\Pi_g - X^2\Pi_u$ electronic transition of the triacetylene cation, HC_6H^+ , around 16654.7 cm^{-1} . © 2002 Elsevier Science B.V. All rights reserved.

1. Introduction

High resolution spectra of unsaturated carbon chain radicals are of interest in view of their role in interstellar hydrocarbon chemistry. Species of the form C_nH , C_nN , $HC_{2n+1}N$ and H_2C_n , with chains containing as many as 11 carbon atoms, have been identified in the dense interstellar medium with the aid of laboratory Fourier transform microwave spectroscopy [1]. It has been argued that electronic transitions of such chains may be among the carriers of unidentified absorption features in diffuse interstellar clouds [2]. The first experimental indication of this came from observations of the electronic absorption spectra of mass-selected carbon

species in neon matrices [3], but owing to solvation effects, the absorption bands exhibit a shift relative to the corresponding gas phase spectra. The latter are now available from a series of experiments on supersonic plasma expansions, using photo-detachment [4], REMPI-TOF [5], and cavity ring down (CRD) [6] spectroscopy with pulsed laser systems. The frequency resolution in these experiments is typically of the order of 0.035 cm^{-1} or worse. In a single-mode cw laser experiment a much higher resolution can be obtained and with this aim a cw cavity ring down setup has been constructed.

Cavity ring down spectroscopy has become a powerful tool for the study of the structural and dynamical properties of molecules in the gas phase. In a series of recent review articles [7–9] a number of useful applications is listed. One of the reasons for this success is the conceptual simplicity

* Corresponding author. Fax: +41-61-267-38-55.

E-mail address: j.p.maier@unibas.ch (J.P. Maier).

of a CRD experiment [10]. A small fraction of laser light is coupled into an optical cavity of length L consisting of two mirrors with a reflectivity $R \sim 99.99\%$ or better. The rate of light leaking out of the cavity has an envelope which is simply a first order exponential decay, $\exp(-t/\tau)$. The ring down time τ is given by $L/[c(1 - R + \alpha l)]$, where c is the speed of light and αl reflects the absorbance for a sample present in the cavity with absorption coefficient α and length l . That is, the ring down time reflects the rate of absorption rather than its magnitude and as such it is independent of power fluctuations. In addition, very long absorption pathlengths are obtained by confining light tens of microseconds to the cavity. This increases the sensitivity considerably and absorption values as small as 10^{-6} per pass have been detected.

In conventional CRD experiments pulsed lasers are used; each light pulse induces a ring down event. In cw experiments this is not the case and more complicated detection schemes must be applied; either by measuring the phase retardation of an amplitude modulated cw laser [11] or by analysing the exponential decay after switching off the laser beam with a fast optical switch [12–17]. In addition, the cavity has to be in resonance with the laser wavelength, because the bandwidth is generally too narrow to excite more than one cavity mode at a time. For this reason several active tracking schemes have been developed [13,14,16], but in a pulsed jet experiment – as it is the case here – such schemes do not work: the gas pulse changes the refraction index, effectively changing the optical length of the cavity, pushing it out of resonance. This effect is further enhanced when plasma fluctuations cause additional instabilities. In this case a passive scheme for mode locking must be used, as it was introduced by Quack and coworkers [15,17].

In this contribution the experimental details are described of a cw CRD setup capable of detecting unstable carbon chains generated in a pulsed supersonic planar plasma expansion. The performance is discussed on the example of a rotationally resolved electronic spectrum of the triacetylene cation, HC_6H^+ .

2. Experimental

The carbon chain radicals are generated by applying a 500 μs high voltage pulse (-600 V, 100 mA) to a 1 ms high pressure gas pulse of a 0.5% HCCH/He mixture that is expanded through a 3 cm \times 200 μm slit with a backing pressure of 10 to 12 bar. The system has been used in other studies (see e.g. [18]) and combines high molecular densities and relatively large absorption path lengths with an effective adiabatical cooling. In addition, the effective resolution is increased compared to pinhole expansions due to a reduced Doppler broadening parallel to the slit. A further reduction is obtained by using a multichannel body. A 3D picture of the nozzle is shown in Fig. 1 together with a short description of its operation. More details are available in [19].

Fig. 2 shows the whole experimental setup. The light of a single mode ring dye laser (Coherent, cw-899 autoscan), pumped by a 6 W solid state laser, is guided through an acousto-optical modulator (AOM). The first order deflection is focused into the ring down cavity via a lens that matches a TEM_{00} cavity mode, where it crosses the planar plasma expansion 6 mm downstream. The CRD mirrors (1 m plano/convex, $R > 99.995\%$) are mounted in a mechanically stable holder at a distance of $L = 32$ cm. A system of internal diaphragms facilitates the alignment and He-curtains protect the mirrors during jet operation from pollution.

A strong transmission occurs only when cavity and laser wavelength are mode matched. To achieve this a passive mode locking system has been used, similar to the method described in [15,17], with several small modifications. One of the mirrors is mounted on a piezo element and by applying a periodical (30 Hz) triangular shaped voltage to the element the cavity length is modulated. The amplitude is chosen in such a way that it corresponds to at least two free spectral ranges of the laser frequency, i.e. the cavity is at least four times in resonance with the laser during one period (Fig. 3). A resonance results in a maximum of transmitted light intensity after the cavity and is monitored using an oscilloscope. When the intensity reaches a certain threshold, a trigger signal is

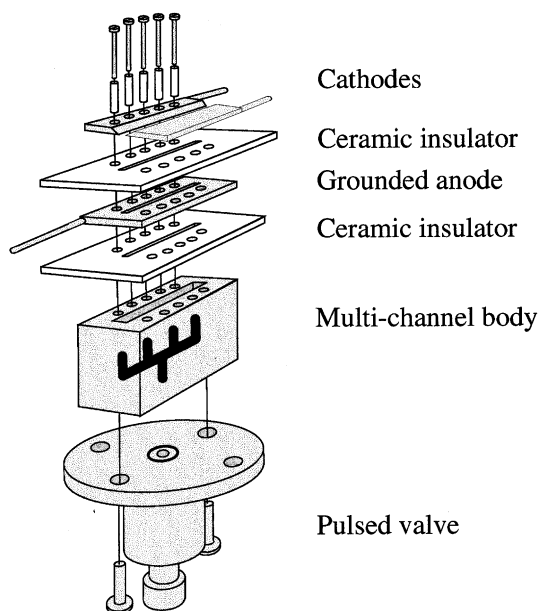


Fig. 1. Artist's view of the high pressure slit nozzle discharge. The orifice consists of two sharp stainless steel jaws (that form the actual slit), a ceramic insulator, a slotted metal plate (grounded) and a second ceramic insulator. Both insulators and metal parts are mounted to the body of the nozzle using electrically isolated screws. A pulsed negative high voltage is applied to the jaws via ballast resistors at the moment that a high pressure gas pulse expands through the channel. The discharge strikes to the grounded plate, localising the reaction zone to a region upstream of the expansion. The body is floating and connected to an electromagnetic driven pulsed valve. A multi-channel system inside the nozzle regulates the gas flow towards the slit and allows a further reduction of the Doppler broadening.

generated that switches off the AOM; the laser beam is interrupted and a ring down event is initiated.

The following detection scheme is used to guarantee that plasma pulse and ring down event coincide (Fig. 3). The data acquisition programme chooses via a simple algorithm the transmission that is strongest and closest to the middle of the ramp voltage. This defines t_0 . The exact ramp voltage at which this cavity resonance occurs is used to define a 300 μs time window at the same ramp voltage in the next cycle. (In order to minimise hysteresis effects of the piezo element, only transmissions on positive or negative ramps are used.) It also defines a delay at which gas and

discharge pulse are activated, in such a way that the plasma expansion coincides with the time window: when a ring down event occurs it automatically samples the plasma. The new resonance defines t_1 and is used to predict the next resonance around t_2 , etc., effectively chasing the resonance. To further increase the sensitivity, only every second cycle is used to trigger gas and discharge pulse. The plasma free ring down event ($\tau_{\text{reference}}$) is then used for background subtraction. This means that with a 30 Hz periodic modulation, 15 ring down events with plasma and 15 ring down events without plasma are measured. The major part of the predicted resonances is within the 300 μs time window, but due to external instabilities the procedure might fail. In this case the data acquisition programme checks the whole ramp, defines a new t_0 and restarts predicting the position of the next resonance. During this short time (3 cycles) only a few data points are lost.

The transmission after the ring-down cavity is focused via a narrow band pass filter onto a broad wavelength band Si-photodiode and recorded in real-time linux using a 12 bit ADC card and a COMEDI driver [20]. The complete decay curve is fitted to an exponential defining τ . The CRD spectrum is obtained by recording $(1/\tau_{\text{plasma}} - 1/\tau_{\text{reference}})$ while scanning the laser. Typical ring down times are $\tau = 27 \mu\text{s}$. This is equivalent to approximately 25'000 passes through the plasma or an effective absorption pathlength of 760 m.

3. Results

In the lower trace of Fig. 4 the rotationally resolved origin band of the $A^2\Pi_g - X^2\Pi_u$ electronic transition of HC_6H^+ is shown. The same transition has been studied in detail before in a liquid nitrogen cooled hollow-cathode discharge cell applying frequency-plasma double modulation (FPM) spectroscopy [21] and is shown for comparison in the upper trace of Fig. 4. At the high ambient temperature in the cell (approximately 150–200 K) the band system is found to comprise the two $A^2\Pi_{3/2} - X^2\Pi_{3/2}$ and $A^2\Pi_{1/2} - X^2\Pi_{1/2}$ subbands, partially overlapping and separated by the difference in spin-orbit constants in ground and elec-

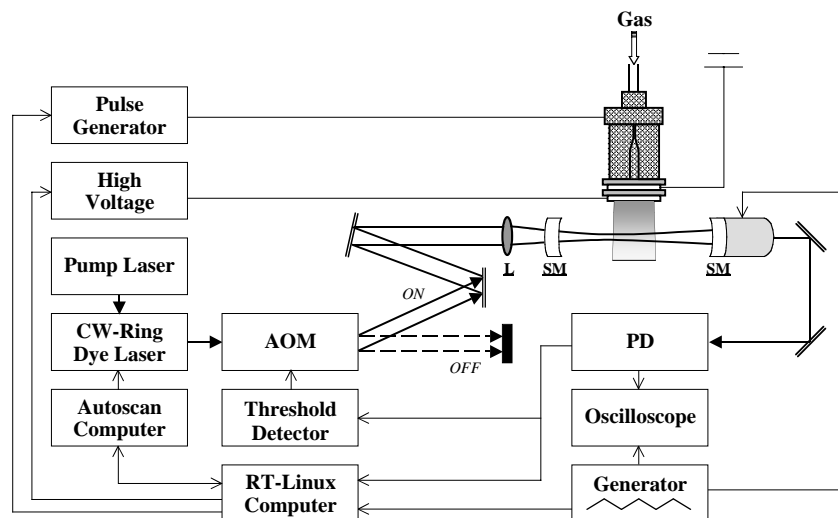


Fig. 2. Schematic of the experimental setup. Details are given in the text.

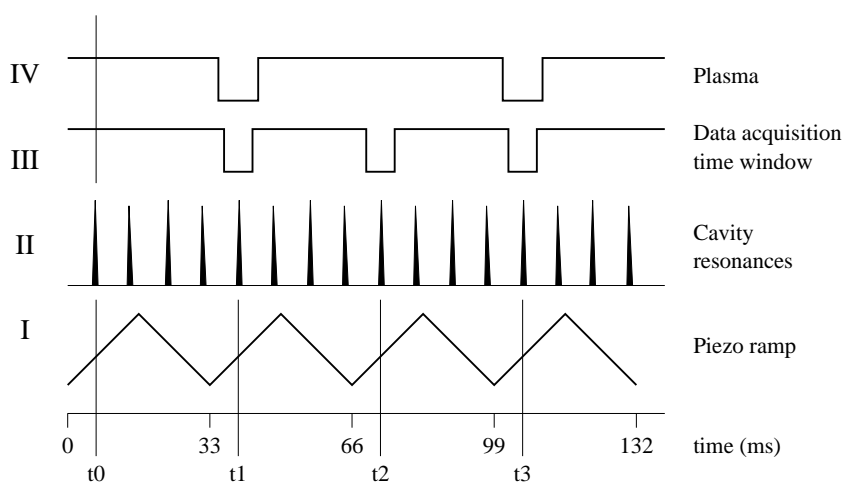


Fig. 3. Timing and triggering scheme. (I) A 30 Hz ramp is applied to a piezo element. (II) The photo diode shows when cavity resonances occur. The data-acquisition programme chooses the transmission closest to the middle of the ramp, defining t_0 and the ramp voltage for which the resonance occurs. When the transmission intensity exceeds a certain threshold, the AOM is switched off and a ring down event is induced. (III) The programme defines a 300 μ s time window in which the next resonance is expected. In order to circumvent hysteresis effects only signals on positive or negative ramps are taken. The example is shown for a positive ramp. (IV) t_0 is also used to trigger the gas and discharge pulse every second ramp. The plasma free ring down event is used for background subtraction.

tronically excited state. Both subbands show strong P- and R-branches, with clear red shaded bandheads and with a weak Q-branch. The spectral simplification upon jet cooling is striking: the jet spectrum displays only one single band. It

consists of well-defined P- and R-branches and a strong Q-branch (Fig. 4). The lower J -levels are markedly stronger and no band head is observed. This is consistent with the low temperature in the supersonic jet. From the relative intensity of

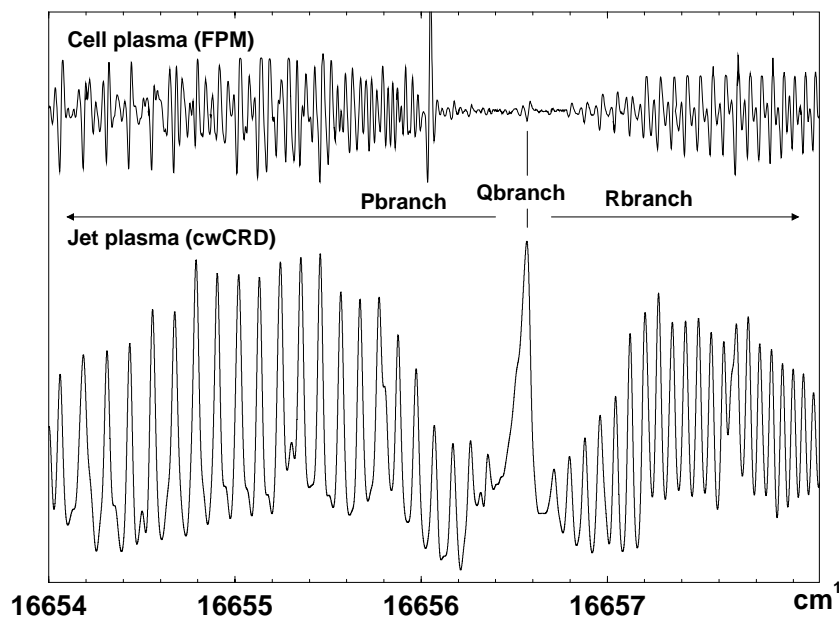


Fig. 4. The origin band of the $A^2\Pi_g - X^2\Pi_u$ electronic spectrum of triacetylene cation, HC_6H^+ , measured by cw CRD spectroscopy through a supersonic pulsed planar plasma with $T_{rot} \sim 15$ K (lower trace). The upper trace shows the corresponding cell spectrum using frequency-plasma double modulation spectroscopy with $T_{rot} \sim 170$ K [21].

subsequent J -levels a rotational temperature of the order of 10 to 15 K is derived. The lower temperature favours the population of the low- J rotational levels and as the Q-line strength is highest for low J -values the Q-branch is now much more pronounced. The spin-orbit splitting in the ground state is about -31 cm^{-1} and as a consequence only the lower ($\Omega = \frac{3}{2}$) spin-orbit component is observed.

The best achievable linewidth (FWHM), using a multichannel body was 450 MHz, two to three times smaller than possible up to now in pulsed laser experiments. This is sufficient to obtain rotational resolution for linear chains with 10 to 11 carbon atoms, as long as no lifetime broadening is involved. However, 450 MHz is still considerably larger than expected from the few MHz bandwidth of the cw laser system. Assuming a Doppler-broadened signal, this corresponds to a translational temperature of the order of 125 K. Indeed, this is due to residual Doppler broadening in the slit expansion, as has been observed before in FPM experiments [22]: the use of a slower expansion gas (for example Ar) reduces the achievable

linewidth proportional to the speed ratios. Clearly, further modifications in the expansion source are necessary to take advantage of the small bandwidth of the cw laser used. A possible improvement could be the use of skimmed planar expansions but such systems have not been reported in the literature yet. Furthermore, it might well be possible that molecular ions diffuse out of the expansion because of charge effects.

The present technique is an extension of previous work in which the same discharge source has been used in combination with a pulsed CRD [19] and a cw frequency-plasma double modulation [23] detection scheme. All three techniques – pulsed CRD, cw-CRD and FPM – have their own advantages and disadvantages.

The pulsed CRD is particularly suited for fast scans. A spectrum comparable to the one shown in Fig. 4 takes less than 20 min to record, whereas the two cw techniques need at least 1.5 h. In addition, special boxcar integration schemes are necessary to compensate for the low duty cycle that is typical when combining a cw detection with a pulsed production technique. The achievable resolution,

on the other hand, is substantially higher in the cw experiments and at this stage only limited by residual Doppler broadening in the expansion. The CRD experiments are generally applicable, whereas the application of the FPM experiment is restricted to absorption lines that are not broadened beyond the modulation amplitude (~ 400 MHz). The resulting line shape is a $1f$ derivative as shown in the upper trace of Fig. 4.

The best achievable S/N ratios are comparable for the three methods. This is achieved by *noise reduction* in the FPM experiment – both laser and plasma noise are reduced in a phase sensitive detection scheme – and by *signal improvement* in the CRD experiments – here the effective absorption path length is increased.

4. Conclusion

It has been shown that cw CRD spectroscopy is a sensitive and generally applicable method to study rotationally cold carbon chain radicals that are produced in a pulsed plasma expansion. The method will be particularly useful in the study of long species with small rotational constants. Passive mode matching is sufficient to perform the experiments. A reduction in linewidth has been obtained. The limiting factor turns out to be residual Doppler broadening in the expansion along the slit.

Acknowledgements

We thank Dr. M. Hippler and Prof. M. Quack for generously sharing their expertise in cw CRD. This work has been supported by the Swiss National Science Foundation, grant 20.63459.00. One of the authors (H.L.) also acknowledges support from FOM (Fundamenteel Onderzoek der Materie).

References

- [1] M.C. McCarthy, P. Thaddeus, Chem. Soc. Rev. 30 (2001) 177, and references therein.
- [2] A.G.G.M. Tielens and T.P. Snow, (Eds.), The diffuse interstellar bands, Dordrecht, 1995, pp. 175–238.
- [3] J.P. Maier, J. Phys. Chem. A. 102 (1998) 3462.
- [4] D.A. Kirkwood, M. Tulej, M.V. Pachkov, M. Schnaiter, F. Guthe, M. Grutter, M. Wyss, J.P. Maier, G. Fischer, J. Chem. Phys. 111 (1999) 9280.
- [5] T. Pino, H.B. Ding, F. Guthe, J.P. Maier, J. Chem. Phys. 114 (2001) 2208.
- [6] T. Motylewski, H. Linnartz, O. Vaizert, J.P. Maier, G.A. Galazutdinov, F.A. Musaev, J. Krelowski, G.A.H. Walker, D.A. Bohlender, Astrophys. J. 531 (2000) 312.
- [7] J.J. Scherer, P.B. Paul, A. O'Keefe, R.J. Saykally, Chem. Rev. 97 (1997) 25.
- [8] M.D. Wheeler, S.M. Newman, A.J. Orr-Ewing, M.N.R. Ashold, J. Chem. Soc. Faraday Trans. 94 (1998) 337.
- [9] G. Berden, R. Peeters, G. Meijer, Int. Rev. Phys. Chem. 19 (2000) 565.
- [10] A. O'Keefe, D.A.G. Deacon, Rev. Sci. Instrum. 59 (1988) 2544.
- [11] R. Engeln, G. von Helden, G. Berden, G. Meijer, Chem. Phys. Lett. 262 (1996) 105.
- [12] D. Romanini, A.A. Kachanov, N. Sadeghi, F. Stoeckel, Chem. Phys. Lett. 264 (1997) 316.
- [13] D. Romanini, A.A. Kachanov, F. Stoeckel, Chem. Phys. Lett. 270 (1997) 538.
- [14] B.A. Paldus, C.C. Harb, T.G. Spence, B. Wilke, J. Xie, J.S. Harris, R.N. Zare, J. Appl. Phys. 83 (1998) 3991.
- [15] Y. He, M. Hippler, M. Quack, Chem. Phys. Lett. 289 (1998) 527.
- [16] M. Murtz, B. Frech, W. Urban, Appl. Phys. B. 68 (1999) 243.
- [17] M. Hippler, M. Quack, Chem. Phys. Lett. 314 (1999) 273.
- [18] H. Linnartz, D. Pfluger, O. Vaizert, P. Cias, P. Birza, D. Khoroshev, J.P. Maier, J. Chem. Phys. 116 (2002) 924, and references therein.
- [19] T. Motylewski, H. Linnartz, Rev. Sci. Instrum. 70 (1999) 1305.
- [20] See D. Schleef, Linux Control and Measurement Device Interface, <ftp://stm.lbl.gov/pub/comedi/>.
- [21] W.E. Sinclair, D. Pfluger, H. Linnartz, J.P. Maier, J. Chem. Phys. 110 (1999) 296.
- [22] D. Pfluger, W.E. Sinclair, H. Linnartz, J.P. Maier, Chem. Phys. Lett. 313 (1999) 171.
- [23] D. Pfluger, T. Motylewski, H. Linnartz, W.E. Sinclair, J.P. Maier, Chem. Phys. Lett. 329 (2000) 29.



Lifetime broadening in the gas phase $\tilde{B}^2\Pi \leftarrow \tilde{X}^2\Pi$ electronic spectrum of C_8H

Petre Birza, Dmitriy Khoroshev, Andrei Chirokolava,
Tomasz Motylewski, John P. Maier *

Department of Chemistry, University of Basel, Klingelbergstr. 80, CH4056 Basel, Switzerland

Received 9 October 2003; in final form 20 October 2003

Abstract

The origin band of the $\tilde{B}^2\Pi_{3/2} \leftarrow \tilde{X}^2\Pi_{3/2}$ electronic transition of linear C_8H was recorded in a planar supersonic expansion by a cw cavity ring-down spectrometer. The C_8H radical was produced using a discharge through a C_2H_2/He mixture inside a pulsed slit nozzle. Despite the fact that the resolution of the spectrometer is 350 MHz, which is 3–4 times higher than the separation of rotational lines in this band, the rotational structure was not resolved. It is concluded that the rotational lines are broadened by rapid radiationless transitions from the excited electronic state. Simulations of the spectrum give an estimate of 0.8 cm^{-1} Lorentzian linewidth which corresponds to ~ 7 ps lifetime in the excited $\tilde{B}^2\Pi_{3/2}$ electronic state.

© 2003 Elsevier B.V. All rights reserved.

1. Introduction

Electronic spectra of carbon chains are especially of interest from the astrophysical point of view. Linear hydrocarbon chains C_nH play an important role in the interstellar chemistry. They were detected in the envelopes of evolved stars and interstellar dark and translucent clouds by radio astronomy [1–3]. These species were extensively studied in the laboratory by microwave [4,5] and electronic spectroscopies [6,7]. Recent

progress in experimental techniques made the measurement of rotationally resolved absorption spectra of electronic transitions in shorter carbon chains possible [8–12]. The origin band of the $\tilde{B}^2\Pi \leftarrow \tilde{X}^2\Pi$ electronic transition of the $C_{2n}H$ ($n = 3 - 5$) radicals was observed in the gas phase using a combination of pulsed laser cavity ring-down spectroscopy (CRDS) with the slit-nozzle expansion of the discharge-generated species [8,13]. Whereas, the spectrum of C_6H was rotationally resolved, the ones of C_8H and $C_{10}H$ were not. The reason was not clear. We attempted to resolve the rotational structure in the stronger ($\Omega = 3/2$) component of the $\tilde{B}^2\Pi \leftarrow \tilde{X}^2\Pi$ origin band of C_8H using a new cw-CRDS setup with resolution of 350 MHz.

* Corresponding author. Fax: +41-61-267-38-55.

E-mail addresses: Andrei.Chirokolava@unibas.ch (A. Chirokolava), J.P.Maier@unibas.ch (J.P. Maier).

2. Experimental approach

The main features of the experiment have been described previously [12]. It is based on the passive cavity mode locking scheme for cw-CRDS [14]. A piezo moves back and forth one of the mirrors of the cavity. When the cavity comes into resonance with the laser frequency and intensity on the photodetector behind the cavity increases to a certain threshold, the laser beam is interrupted by switching off the acousto-optic modulator. The light intensity in the cavity and on the photodetector then decays exponentially with time. Due to spatial filtering and mode matching of the laser beam, only TEM₀₀ cavity modes have significant intensity. The timing of the valve opening and high voltage pulse is calculated so as to coincide with the ring-down.

A number of improvements to our previous setup [12] have been made. (1) Before, several signals (photodetector, pressure gauges, voltage applied to the piezo) were recorded by the same data acquisition card, which switched between different channels. The switching resulted in spikes in the ring-down signal. Now two data acquisition cards are used, one for the ring-down signal, the other for all other signals, so there are no spikes. (2) The algorithm for triggering the gas and HV

pulses has been changed. The delays for activating the valve and discharge are measured from the first resonance on the ascending voltage ramp (Fig. 1), rather than from the analysed ring-down in the last period of the triangular-wave voltage. This algorithm is more robust and allows for larger steps in the laser scan. Non-linear response of the piezo element to the applied voltage results in slightly different delays between the first and the second resonances, depending on their positions with respect to the voltage ramp. This leads to the changes in relative timing of the HV pulse and the ring-down event as the laser is scanned and the resonances move relative to the ramp. To preserve this relative timing, the delay between the first resonance and the HV pulse is adjusted taking into account piezo nonlinearity. (3) The triangular-wave voltage for the piezo element is generated now by the data acquisition card instead of the stand-alone function generator. After all these changes, the signal-to-noise ratio improved 2.5 times. The achieved sensitivity was of order 10^{-7} – 10^{-8} cm⁻¹.

The carbon chain species were generated by applying a high voltage pulse (–1000 V, 150 mA) to a 0.2% gas mixture of acetylene in helium expanding through the slit nozzle (3 cm × 200 μm) with the backing pressure of 11 bar. The pressure

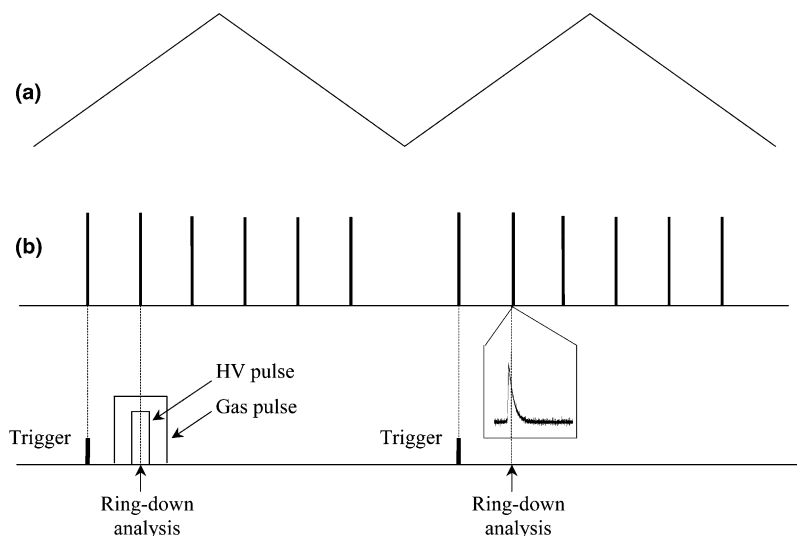


Fig. 1. Relative timing of the piezo ramp voltage, cavity resonances, valve opening, and high voltage pulse applied to the slit electrodes. (a) Ramp voltage applied to the piezo. (b) Signal on the photodetector.

in the vacuum chamber was 0.23 mbar. The laser beam crossed the jet 10 mm downstream the expansion. The number density of C_8H species in this region was estimated using a theoretical oscillator strength (3.4×10^{-3}) for this electronic transition [15]. In the 5 K neon matrix spectrum, the integrated absorption of the origin band is approximately equal to that of the other vibronic bands in the $\tilde{B}^2\Pi \leftarrow \tilde{X}^2\Pi$ system [6]. Because only the origin band was measured in our experiment, the oscillator strength was reduced accordingly and leads to an estimate of the C_8H number density in the discharge plasma of $6 \times 10^8 \text{ cm}^{-3}$.

3. Results and discussion

The recorded spectrum is shown in Fig. 2. The two broad features are the *P* and *R* branches of the origin band of the $\tilde{B}^2\Pi_{3/2} \leftarrow \tilde{X}^2\Pi_{3/2}$ electronic transition of C_8H . This band was first observed in 5 K neon matrix using mass-selected deposition [6]. It was assigned in the gas phase [13] on the basis of the known gas phase – neon matrix shifts [16] for similar hydrocarbon chains. This assignment was confirmed by equal frequency shifts resulting from

deuterium substitution in the neon matrix [17] and in the supersonic jet experiment [13].

The large narrow peaks belong to another carrier, propadienyldiene (H_2CCC). They are much stronger in this spectrum compared to the earlier measurement [13], because a slightly different nozzle design [12] has been used. The latter minimizes Doppler broadening, but at the same time increases the production of shorter carbon chains. Although overlap with the features of another carrier complicates the spectrum, one can see that the rotational structure of C_8H remains unresolved.

The distance between the lines in the *P* and *R* branches is expected to be about 0.04 cm^{-1} (1.2 GHz). Our resolution, estimated by the width of the narrowest feature (FWHM) in the spectrum, was at least 350 MHz. It should be more than sufficient to resolve the rotational structure of the C_8H band. One can compare this spectrum to the origin band in the $\tilde{A}^2\Pi_{3/2} \leftarrow \tilde{X}^2\Pi_{3/2}$ transition of the isoelectronic linear tetraacetylene cation, HC_8H^+ , recorded under similar conditions with a laser linewidth of $\sim 900 \text{ MHz}$ (see Fig. 2 of [9]). There the *P* branch is well resolved; the *R* branch is partially resolved.

The rotational level broadening in the upper $\tilde{B}^2\Pi$ electronic state of C_8H is caused by rapid

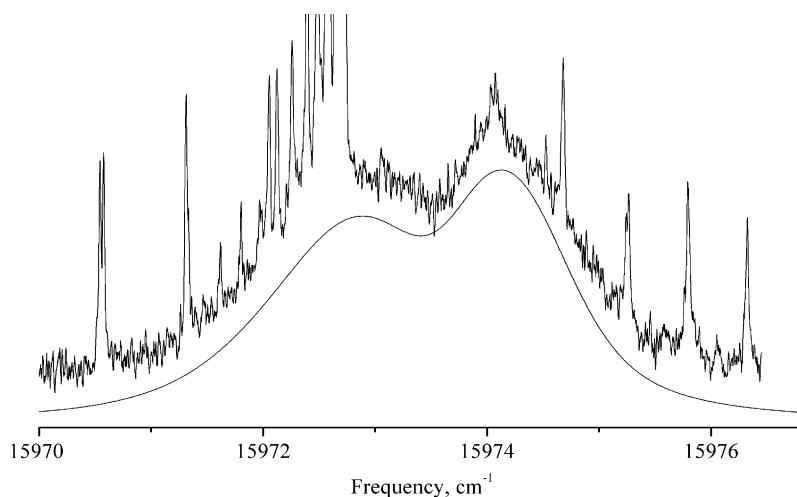


Fig. 2. Experimental and simulated spectra of the origin band in the $\tilde{B}^2\Pi_{3/2} \leftarrow \tilde{X}^2\Pi_{3/2}$ electronic transition of C_8H . The spectrum was recorded in absorption across a pulsed supersonic slit jet using a cw cavity ring-down approach. The two broad features are the *P* and *R* branches of this electronic transition. The narrow peaks belong to propadienyldiene H_2CCC . Upper state rotational constant for the simulated spectrum is $B' = 0.0195 \pm 0.0001 \text{ cm}^{-1}$, other constants are fixed to the ground state values [4]. Rotational temperature is $T_{\text{rot}} = 15 \pm 2 \text{ K}$, Lorentzian broadening $\Delta\nu_{\text{lor}} = 0.8 \pm 0.1 \text{ cm}^{-1}$ (24 GHz). The simulated spectrum is slightly shifted down with respect to the experimental one.

radiationless transitions from this electronic state. Nonradiative relaxation of the $\tilde{B}^2\Pi$ electronic state is present in other members of the $C_{2n}H$ series as well. It manifests itself as a two-component fluorescence decay in C_4H with excited state lifetime estimate of 20 ns [18]. In the case of C_6H [8], the $\tilde{B}^2\Pi_{3/2} \leftarrow \tilde{X}^2\Pi_{3/2}$ electronic absorption spectrum is best simulated when a Lorentzian broadening of $\sim 0.055 \text{ cm}^{-1}$ is introduced in addition to a Gaussian linewidth of 0.037 cm^{-1} resulting from the laser linewidth and Doppler broadening. This corresponds to an excited state lifetime of order 0.1 ns.

We simulated the observed broadening in the $\tilde{B}^2\Pi_{3/2} \leftarrow \tilde{X}^2\Pi_{3/2}$ origin band of C_8H (Fig. 1) by varying three parameters; upper state rotational constant B' , rotational temperature T_{rot} , and Lorentzian linewidth $\Delta\nu_{\text{lor}}$. B'' was fixed to the value of $0.019589011 \text{ cm}^{-1}$ taken from [4]. The obtained values are $B' = 0.0195 \pm 0.0001 \text{ cm}^{-1}$, $T_{\text{rot}} = 15 \pm 2 \text{ K}$, and $\Delta\nu_{\text{lor}} = 0.8 \pm 0.1 \text{ cm}^{-1}$ (24 GHz), respectively. Thus, the ratio B'/B'' for C_8H is 0.995 ± 0.005 , which is close to the value of 0.99 for isoelectronic species [9–11].

In contrast to C_8H , the rotational structure is well resolved for the corresponding $\tilde{A}^2\Pi \leftarrow \tilde{X}^2\Pi$ electronic origin bands of the isoelectronic linear cations HC_8H^+ [9], HC_7N^+ [10] and NC_6N^+ [11]. Apparently, the presence of an additional low-lying $^2\Sigma^+$ excited electronic state in the C_6H and C_8H radicals [15,19–21] enhances vibronic interactions between the $\tilde{B}^2\Pi$ and lower electronic states and accelerates internal conversion. This broadening caused by intramolecular processes is one of the reasons why carbon chains attracted attention in connection with the diffuse interstellar bands [22].

Acknowledgements

This work has been supported by the Swiss National Science Foundation (project 200020-100019).

References

- [1] M. Guelin, J. Cernicharo, M.J. Travers, M.C. McCarthy, C.A. Gottlieb, P. Thaddeus, M. Ohishi, S. Saito, S. Yamamoto, *Astron. Astrophys.* 317 (1997) L1.
- [2] M.B. Bell, P.A. Feldman, J.K.G. Watson, M.C. McCarthy, M.J. Travers, C.A. Gottlieb, P. Thaddeus, *Astrophys. J.* 518 (1999) 740.
- [3] B.E. Turner, E. Herbst, R. Terzieva, *Astrophys. J. Suppl. Ser.* 126 (2000) 427.
- [4] M.C. McCarthy, M.J. Travers, A. Kovacs, C.A. Gottlieb, P. Thaddeus, *Astrophys. J. Suppl. Ser.* 113 (1997) 105.
- [5] C.A. Gottlieb, M.C. McCarthy, M.J. Travers, J.U. Grabow, P. Thaddeus, *J. Chem. Phys.* 109 (1998) 5433.
- [6] P. Freivogel, J. Fulara, M. Jakobi, D. Forney, J.P. Maier, *J. Chem. Phys.* 103 (1995) 54.
- [7] H. Ding, T. Pino, F. Guthe, J.P. Maier, *J. Chem. Phys.* 117 (2002) 8362.
- [8] H. Linnartz, T. Motylewski, O. Vaizert, J.P. Maier, A.J. Apponi, M.C. McCarthy, C.A. Gottlieb, P. Thaddeus, *J. Mol. Spectrosc.* 197 (1999) 1.
- [9] D. Pfluger, T. Motylewski, H. Linnartz, W.E. Sinclair, J.P. Maier, *Chem. Phys. Lett.* 329 (2000) 29.
- [10] W.E. Sinclair, D. Pfluger, D. Verdes, J.P. Maier, *J. Chem. Phys.* 112 (2000) 8899.
- [11] H. Linnartz, D. Pfluger, O. Vaizert, P. Cias, P. Birza, D. Khoroshev, J.P. Maier, *J. Chem. Phys.* 116 (2002) 924.
- [12] P. Birza, T. Motylewski, D. Khoroshev, A. Chirokolava, H. Linnartz, J.P. Maier, *Chem. Phys.* 283 (2002) 119.
- [13] H. Linnartz, T. Motylewski, J.P. Maier, *J. Chem. Phys.* 109 (1998) 3819.
- [14] M. Hippler, M. Quack, *Chem. Phys. Lett.* 314 (1999) 273.
- [15] A.L. Sobolewski, L. Adamowicz, *J. Chem. Phys.* 102 (1995) 394.
- [16] J.P. Maier, *J. Phys. Chem. A* 102 (1998) 3462.
- [17] P. Freivogel, Ph.D. Dissertation, University of Basel, Basel, 1997.
- [18] K. Hoshina, H. Kohguchi, Y. Ohshima, Y. Endo, *J. Chem. Phys.* 108 (1998) 3465.
- [19] T.R. Taylor, C. Xu, D.M. Neumark, *J. Chem. Phys.* 108 (1998) 10018.
- [20] J. Myung Lee, L. Adamowicz, *Spectrochim. Acta. Part A* 57A (2001) 897.
- [21] Z. Cao, S.D. Peyerimhoff, *Phys. Chem. Chem. Phys.* 3 (2001) 1403.
- [22] A.E. Douglas, *Nature* 269 (1977) 130.

Rotationally resolved electronic spectroscopy of a nonlinear carbon chain radical $C_6H_4^+$

Dmitriy Khoroshev, Mitsunori Araki,* Przemyslaw Kolek, Petre Birza,
Andrei Chirokolava, and John P. Maier

Department of Chemistry, University of Basel, Klingelbergstrasse 80, CH-4056 Basel, Switzerland

Received 11 February 2004; in revised form 25 May 2004

Available online 25 June 2004

Abstract

Rotationally resolved electronic spectrum of the origin band in the ${}^2A''-X^2A''$ transition of a nonlinear carbon chain radical $C_6H_4^+$ has been recorded in the 604 nm region using cw cavity ring down spectroscopy. The radical was produced by a discharge through an acetylene–helium mixture in a supersonic planar expansion. The rotational structure has been analysed and $\frac{1}{2}(B+C)$ precisely determined. A band having *a*-type prolate rotational structure has also been observed near 581 nm. By considering the results of ab initio calculations this band is assigned to a transition involving the excitation of the ν_{12} fundamental in the upper ${}^2A''$ electronic state of the same $C_6H_4^+$ isomer.

© 2004 Elsevier Inc. All rights reserved.

Keywords: Nonlinear carbon chain; $C_6H_4^+$; Cavity ring down; Rotational constant

1. Introduction

High resolution spectroscopy of unsaturated carbon chain radicals is interesting from the viewpoint of interstellar hydrocarbon chemistry as well as terrestrial discharges and flames. Electronic transitions of the chain species HC_nH^+ $n = 4, 6, 8, 10$ [1–4] and C_nH [5] with an even number of carbons have been studied so far. Recently, a nonlinear planar carbon chain radical $C_6H_4^+$, $H-C\equiv C-C\equiv C-CH=CH_2^+$ (hereafter “ $C_6H_4^+$ ” indicates this structural isomer, Fig. 1), was detected in a supersonic planar discharge by cavity ring down (CRD) spectroscopy in the 604 nm region [6]. The related $C_4H_4^+$ and $C_8H_4^+$ nonlinear carbon chains were also produced and detected in this plasma [7].

Hydrogenated nonlinear chains can exist in dark interstellar clouds as well as the linear ones, e.g., column densities of C_2O , H_2CCO , and CH_3CHO are of the same order of magnitude in the TMC-1 dark cloud [8].

Therefore, long nonlinear carbon chains having an asymmetric top structure may be present in such clouds with comparable abundance. However, they have not yet been detected by radioastronomy because their pure rotational transitions are too weak compared to those of linear carbon chains. If a sufficiently long integration in the radio observations could be carried out based on an accurate rest frequency, identification may prove possible in the future. Thus laboratory measurements of the pure rotational transitions are necessary, and in turn this requires reasonable a priori knowledge of the ground state rotational constants. A rotationally resolved electronic spectrum can produce such constants both in the ground and excited states. For this reason the ${}^2A''-X^2A''$ origin band of $C_6H_4^+$ (Fig. 1) was recorded using high-resolution cw-CRD spectroscopy as part of this work. Additionally, an unassigned 585.3 nm absorption band, produced by a molecule having the same mass as $C_6H_4^+$, was observed in a 6 K neon-matrix [6]. To identify the carrier, this frequency region was scanned in the gas phase using cw-CRD spectroscopy, and a rotationally resolved band was observed at 581 nm.

* Corresponding author. Fax: +41-61-267-38-55.

E-mail address: mitsunori.araki@unibas.ch (M. Araki).

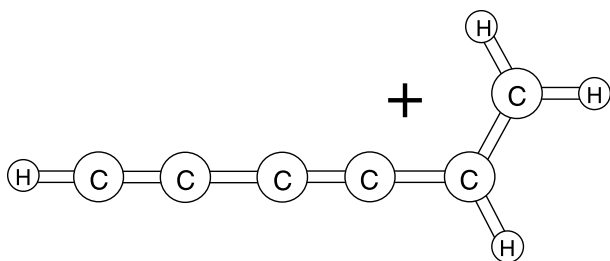


Fig. 1. Geometry of the observed isomer of $C_6H_4^+$.

2. Experimental details

The experimental set-up has been described elsewhere [9]. It consists of a cw-CRD spectrometer sampling a supersonic planar plasma. The plasma was generated by a discharge through a gas pulse (-500 V, 60 Hz repetition rate) of 0.2% acetylene in helium gas mixture with a backing pressure of 10 bar in the throat of a $3\text{ cm} \times 200\text{ }\mu\text{m}$ multilayer slit nozzle. Rotational temperatures of the order 15–40 K are routinely obtained. The nozzle was mounted in an optical cavity where the expansion was intersected ~ 7 mm downstream by a laser.

The light of a single mode ring dye laser, pumped by a 6 W solid state laser, was guided through an acousto-optical modulator (AOM). The first order deflection was focused into the ring down cavity via a lens that matches the TEM_{00} mode, where it crossed the planar plasma

expansion. The CRD mirrors (1 m plano-concave, $R > 99.995\%$) were mounted in a mechanically stable holder separated by a distance of 32 cm. One was mounted on a piezo-element to which a period (60 Hz) triangular shaped voltage was applied. A strong transmission occurs only when the cavity and laser light are mode matched [10]. A resonance results in a maximum of transmitted light intensity after the cavity and is monitored via a Si-photodiode using a data acquisition system. When the intensity reaches a certain threshold a trigger signal is generated that switches off the AOM; the laser beam is interrupted and a ring down event initiated. The light leaking out of the cavity was recorded and the decay curve fitted to an exponential. The absorption spectrum was plotted as a function of the ring-down time τ . The observed spectrum was calibrated by recording simultaneously I_2 absorption in a cell. Although the resolution of the ring dye laser was 500 kHz, the spectra of $C_6H_4^+$ measured show a line width of 0.01 cm^{-1} . This is due to Doppler broadening in the planar discharge as well as lifetime shortening in the excited electronic state of $C_6H_4^+$.

3. Results and discussion

3.1. Origin band

The 604 nm origin band in the ${}^2A''-X^2A''$ electronic transition of $C_6H_4^+$ was observed previously at

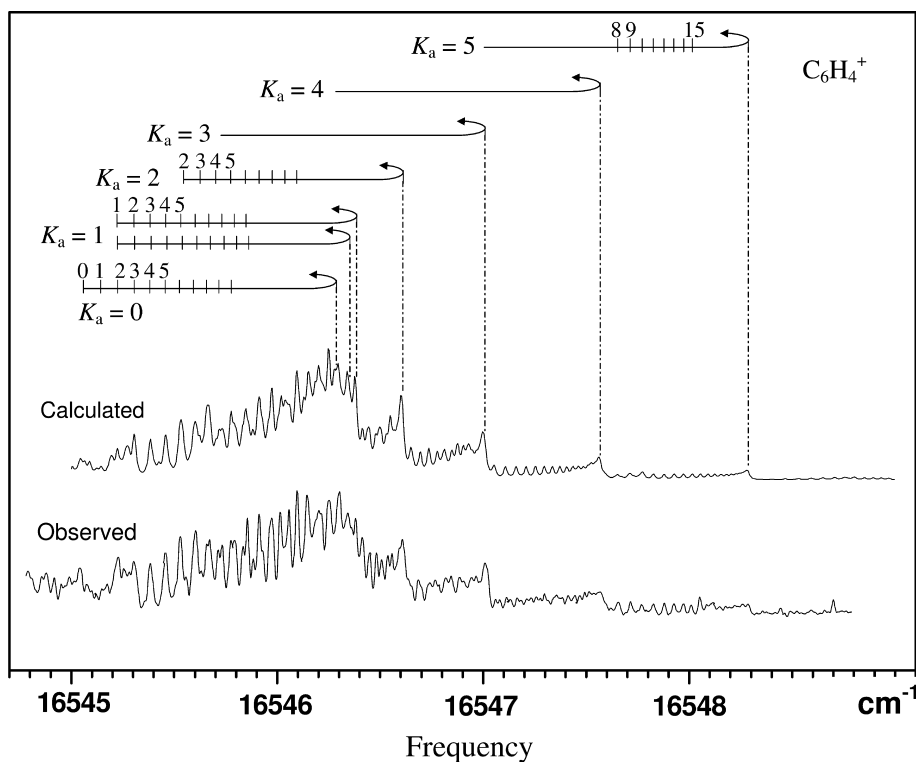


Fig. 2. The rotationally resolved electronic absorption spectra of the origin band in the ${}^2A''-X^2A''$ transition for $C_6H_4^+$ and the simulated rotational structure at 20 K.

Table 1

The observed and fitted rovibronic lines for the origin band in the ${}^2A''-X^2A''$ electronic transition of $C_6H_4^+$

$N_{K_a K_c}$	$\nu_{\text{obs}} (\text{cm}^{-1})$	$\nu_{\text{calc}} (\text{cm}^{-1})$	$o - c (\text{cm}^{-1})$
3 _{0 3} -2 _{0 2}	16545.2258	16545.2258	0.0000
2 _{1 1} -1 _{1 0}		16545.2242	0.0016
2 _{1 2} -1 _{1 1}		16545.2219	0.0039
4 _{0 4} -3 _{0 3}	16545.3036	16545.3053	-0.0017
3 _{1 3} -2 _{1 2}		16545.3039	-0.0003
3 _{1 2} -2 _{1 1}		16545.3073	-0.0037
4 _{1 4} -3 _{1 3}	16545.3842	16545.3828	0.0014
4 _{1 3} -3 _{1 2}		16545.3874	-0.0032
5 _{0 5} -4 _{0 4}		16545.3817	0.0025
6 _{0 6} -5 _{0 5}	16545.4574	16545.4550	0.0024
5 _{1 5} -4 _{1 4}		16545.4587	-0.0013
5 _{1 4} -4 _{1 3}		16545.4643	-0.0069
7 _{0 7} -6 _{0 6}	16545.5295	16545.5252	0.0043
6 _{1 6} -5 _{1 5}		16545.5314	-0.0019
6 _{1 5} -5 _{1 4}		16545.5382	-0.0087
8 _{0 8} -7 _{0 7}	16545.6028	16545.5924	0.0104
7 _{1 7} -6 _{1 6}		16545.6011	0.0017
7 _{1 6} -6 _{1 5}		16545.6090	-0.0062
9 _{0 9} -8 _{0 8}	16545.6582	16545.6564	0.0018
8 _{1 8} -7 _{1 7}	16545.6711	16545.6677	0.0034
8 _{1 7} -7 _{1 6}		16545.6767	-0.0056
10 _{0 10} -9 _{0 9}	16545.7138	16545.7174	-0.0036
9 _{1 9} -8 _{1 8}	16545.7319	16545.7312	0.0007
9 _{1 8} -8 _{1 7}		16545.7414	-0.0095
11 _{0 11} -10 _{0 10}	16545.7761	16545.7753	0.0008
6 _{2 5} -5 _{2 4}		16545.7743	0.0018
10 _{1 10} -9 _{1 9}	16545.7920	16545.7916	0.0004 ^a
10 _{1 9} -9 _{1 8}		16545.8029	-0.0109 ^a
12 _{0 12} -11 _{0 11}	16545.8344	16545.8300	0.0044
11 _{1 11} -10 _{1 10}	16545.8547	16545.8489	0.0058 ^a
11 _{1 10} -10 _{1 9}		16545.8614	-0.0067 ^a
7 _{2 5} -6 _{2 4}		16545.8446	0.0101
13 _{0 13} -12 _{0 12}	16545.8836	16545.8817	0.0019
12 _{1 12} -11 _{1 11}	16545.9120	16545.9032	0.0088 ^a
12 _{1 11} -11 _{1 10}		16545.9168	-0.0048 ^a
8 _{2 7} -7 _{2 6}		16545.9117	0.0003
14 _{0 14} -13 _{0 13}	16545.9277	16545.9303	-0.0026
13 _{1 13} -12 _{1 12}	16545.9710	16545.9544	0.0166 ^a
13 _{1 12} -12 _{1 11}		16545.9691	0.0019 ^a
15 _{0 15} -14 _{0 14}		16545.9759	-0.0049
9 _{2 7} -8 _{2 6}		16545.9758	-0.0048
14 _{1 14} -13 _{1 13}	16546.0147	16546.0024	0.0123 ^a
14 _{1 13} -13 _{1 12}		16546.0183	-0.0036 ^a
16 _{0 16} -15 _{0 15}		16546.0183	-0.0036
17 _{0 17} -16 _{0 16}	16546.0564	16546.0576	-0.0012
15 _{1 15} -14 _{1 14}		16546.0474	0.0090 ^a
15 _{1 14} -14 _{1 13}		16546.0644	-0.0080 ^a
16 _{1 16} -15 _{1 15}	16546.0966	16546.0893	0.0073 ^a
16 _{1 15} -15 _{1 14}		16546.1074	-0.0108 ^a
18 _{0 18} -17 _{0 17}		16546.0939	0.0027

Table 1 (continued)

$N_{K_a K_c}$	$\nu_{\text{obs}} (\text{cm}^{-1})$	$\nu_{\text{calc}} (\text{cm}^{-1})$	$o - c (\text{cm}^{-1})$
11 _{2 10} -10 _{2 9}		16546.0946	0.0020
28 _{0 28} -27 _{0 27}	16546.3000	16546.2865	0.0135
31 _{0 31} -30 _{0 30}		16546.2840	0.0160
29 _{0 29} -28 _{0 28}		16546.2887	0.0113
30 _{0 30} -29 _{0 29}		16546.2879	0.0121
28 _{1 28} -27 _{1 27}	16546.3414	16546.3516	-0.0102
31 _{1 31} -30 _{1 30}		16546.3478	-0.0064
29 _{1 29} -28 _{1 28}		16546.3534	-0.0120
30 _{1 30} -29 _{1 29}		16546.3521	-0.0107
32 _{1 31} -31 _{1 30}	16546.3800	16546.3765	0.0035
28 _{1 27} -27 _{1 26}		16546.3833	-0.0033
31 _{1 30} -30 _{1 29}		16546.3828	-0.0028
29 _{1 28} -28 _{1 27}		16546.3862	-0.0062
30 _{1 29} -29 _{1 28}		16546.3860	-0.0060
19 _{2 18} -18 _{2 17}	16546.4475	16546.4468	0.0007
19 _{2 17} -18 _{2 16}		16546.4474	0.0001
20 _{2 19} -19 _{2 18}	16546.4820	16546.4769	0.0051
20 _{2 18} -19 _{2 17}		16546.4776	0.0044
21 _{2 20} -20 _{2 19}	16546.5067	16546.5040	0.0027
21 _{2 19} -20 _{2 18}		16546.5048	0.0019
28 _{2 27} -27 _{2 26}	16546.6072	16546.6070	0.0002
28 _{2 26} -27 _{2 25}		16546.6086	-0.0014
31 _{2 30} -30 _{2 29}		16546.6049	0.0023
31 _{2 29} -30 _{2 28}		16546.6068	0.0004
29 _{2 28} -28 _{2 27}		16546.6094	-0.0022
29 _{2 27} -28 _{2 26}		16546.6111	-0.0039
30 _{2 29} -29 _{2 28}		16546.6087	-0.0015
30 _{2 28} -29 _{2 27}		16546.6105	-0.0033
28 _{3 26} -27 _{3 25}	16547.0091	16547.0065	0.0026
28 _{3 25} -27 _{3 24}		16547.0066	0.0025
31 _{3 29} -30 _{3 28}		16547.0045	0.0046
31 _{3 28} -30 _{3 27}		16547.0045	0.0046
29 _{3 26} -28 _{3 25}		16547.0090	0.0001
29 _{3 27} -28 _{3 26}		16547.0089	0.0002
30 _{3 27} -29 _{3 26}		16547.0083	0.0008
30 _{3 28} -29 _{3 27}		16547.0083	0.0008
28 _{4 25} -27 _{4 24}	16547.5636	16547.5652	-0.0016
28 _{4 24} -27 _{4 23}		16547.5652	-0.0016
31 _{4 27} -30 _{4 26}		16547.5631	0.0005
31 _{4 28} -30 _{4 27}		16547.5631	0.0005
29 _{4 26} -28 _{4 25}		16547.5676	-0.0040
29 _{4 25} -28 _{4 24}		16547.5676	-0.0040
30 _{4 26} -29 _{4 25}		16547.5669	-0.0033
30 _{4 27} -29 _{4 26}		16547.5669	-0.0033
9 _{5 4} -8 _{5 3}	16547.6546	16547.6519	0.0027
9 _{5 5} -8 _{5 4}		16547.6519	0.0027
10 _{5 6} -9 _{5 5}	16547.7158	16547.7129	0.0029
10 _{5 5} -9 _{5 4}		16547.7129	0.0029
11 _{5 6} -10 _{5 5}	16547.7693	16547.7708	-0.0015
11 _{5 7} -10 _{5 6}		16547.7708	-0.0015
12 _{5 8} -11 _{5 7}	16547.8258	16547.8256	0.0002
12 _{5 7} -11 _{5 6}		16547.8256	0.0002
13 _{5 9} -12 _{5 8}	16547.8789	16547.8774	0.0015
13 _{5 8} -12 _{5 7}		16547.8774	0.0015
14 _{5 10} -13 _{5 9}	16547.9262	16547.9260	0.0002

Table 1 (continued)

$N_{K_a K_c}$	$\nu_{\text{obs}} (\text{cm}^{-1})$	$\nu_{\text{calc}} (\text{cm}^{-1})$	$\text{o} - \text{c} (\text{cm}^{-1})$
14 _{5 9} –13 _{5 8}		16547.9260	0.0002
15 _{5 10} –14 _{5 9}	16547.9713	16547.9716	–0.0003
15 _{5 11} –14 _{5 10}		16547.9716	–0.0003
16 _{5 11} –15 _{5 10}	16548.0097	16548.0141	–0.0044
16 _{5 12} –15 _{5 11}		16548.0141	–0.0044
28 _{5 24} –27 _{5 23}	16548.2844	16548.2835	0.0009
28 _{5 23} –27 _{5 22}		16548.2835	0.0009
31 _{5 27} –30 _{5 26}		16548.2814	0.0030
31 _{5 26} –30 _{5 25}		16548.2814	0.0030
29 _{5 24} –28 _{5 23}		16548.2859	–0.0015
29 _{5 25} –28 _{5 24}		16548.2859	–0.0015
30 _{5 25} –29 _{5 24}		16548.2852	–0.0008
30 _{5 26} –29 _{5 25}		16548.2852	–0.0008

^a Weight is 0.1 in the least-squares fit.

0.15 cm^{–1} resolution [6]. In order to determine more accurate rotational constants, the *R*-branch region of this band, which includes a lot of unblended lines, was re-measured using a resolution of 0.01 cm^{–1}. More than 40 rotational lines were recorded and the observed spectrum is shown in Fig. 2 (lower trace). The assignment is based on the constants given in [6]. The analysis was carried out using a conventional Hamiltonian for an asymmetric top molecule where the energy levels were calculated by direct numerical diagonalisation of Hamiltonian matrices and molecular parameters were determined by a least-squares fit to the observed line frequencies. The ground-state rotational constant A'' was fixed to the value deduced in [6], because it could not be determined from the observed *a*-type transitions. The rotational constant differences between the ground

and excited state, ΔB and ΔC , which cannot be computed independently from the present data, were assumed to be equal. The measured line frequencies and their assignments are given in Table 1, and the constants inferred in Table 2. A rotational-profile simulation program WANG [11] reproduced well the observed spectrum as shown in Fig. 2 (upper trace).

Asymmetry of a near prolate top molecule can be expressed by $B - C$, which is obtained mainly from the asymmetry splitting of a $K_a = 1$ series in the *R*-branch. However, this separation was not resolved for the transitions having $J \leq 15$. Both components were assigned to one line: for instance the $J_{K_a K_c} = 16_{1 16} - 15_{1 15}$ and $16_{1 15} - 15_{1 14}$ transitions were assigned to the 16546.0966 cm^{–1} peak (Table 1). Thus, the difference $B - C$ will be underestimated by the least-squares fit and the obtained value ($= 0.0011 \text{ cm}^{-1}$) is smaller than that obtained from an ab initio calculation (CASSCF/cc-pVTZ, 0.0016 cm^{–1}). An average, $\frac{1}{2}(B + C)$, of the two constants was determined accurately from the present data and agrees well with the previous report [6] but with increased accuracy. Frequencies of the pure rotational transitions in the millimetre region can be adequately predicted by the rotational constant $\frac{1}{2}(B + C)$: for example the *a*-type $J = 7 - 6$ transition is at 19 271 MHz with an 1σ error of 62 MHz, excluding the effect of spin-rotation constants.

3.2. Vibrationally excited band

An absorption band observed at 585.3 (584.7) nm following mass-selection of C₆H₄⁺ (C₆D₄⁺) in a 6 K neon matrix was assumed to belong to another isomer of C₆H₄⁺ because of difference in the band profile compared

Table 2
Molecular constants for C₆H₄⁺ and C₆D₄⁺ (cm^{–1})^a

		C ₆ H ₄ ⁺				C ₆ D ₄ ⁺			
		604 nm	581 nm	Ref. [6]	Calc. ^b	581 nm	Ref. [6]	Calc. ^b	
Ground state X^2A''	A''	1.24 ^c	1.24 ^c	1.24	1.271	0.89 ^c	0.89	0.923	
	B''	0.046481(149)	0.046608(193)	0.0467	0.0466	0.04281(97)	0.0416	0.0415	
	C''	0.045349(145)	0.045378(193)	0.0449	0.0450	0.04061(97)	0.0400	0.0397	
	$\frac{1}{2}(B'' + C'')$	0.045915(147)	0.045993(193)			0.04171(97)			
Excited state $^2A''$	Origin $v = 0$	ΔA	0.078274(50)	0.0767	0.080		0.0450	0.047	
		$\Delta\frac{1}{2}(B + C)$	–0.0014519(72)	–0.0015	–0.0011		–0.0013	–0.010	
		T_{00}	16544.96879(196) ^d	16544.980			16611.91		
	$v_{12} = 1$	ΔA		0.07602(82)			0.04665(63)		
		$\Delta\frac{1}{2}(B + C)$		–0.0014613(151)			–0.001444(79)		
		T_{10}		17213.7228(22) ^d			17218.1664(118) ^d		
		ν		668.7540(42)			606.26		
	rms		0.0046	0.0043			0.0066		

^a Values in parentheses denote the standard deviation and apply to the last digits of the constants.

^b Calculated with CASSCF/cc-pVTZ.

^c Fixed to the value of [6].

^d The error is from the least-squares fitting, and uncertainty of the calibration is 0.007 cm^{–1}.

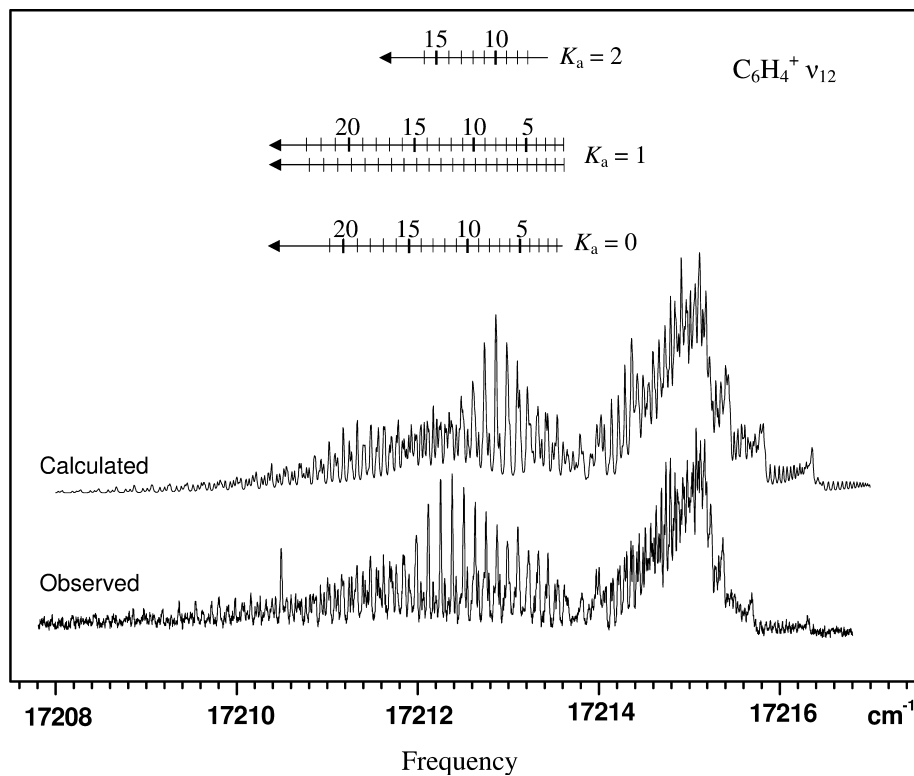


Fig. 3. The rotationally resolved electronic absorption spectra of the 581 nm band in the ${}^2A'' (v_{12} = 1) \rightarrow X^2A'' (v = 0)$ transition for $C_6H_4^+$ and the simulated rotational structure at 20 K.

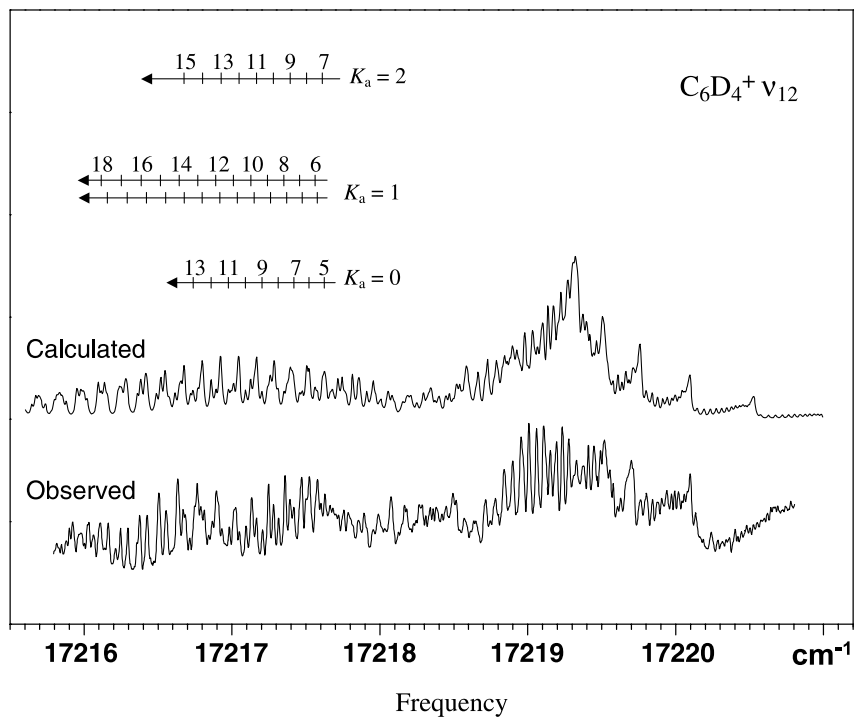


Fig. 4. The rotationally resolved electronic absorption spectra of the 581 nm band in the ${}^2A'' (v_{12} = 1) \rightarrow X^2A'' (v = 0)$ transition for $C_6D_4^+$ and the simulated rotational structure at 20 K.

Table 3

The observed and fitted rovibronic lines in the 581 nm band of the ${}^2A''\text{-}X^2A''$ electronic transition of C_6H_4^+

$N_{K_a K_c}$	$\nu_{\text{obs}} (\text{cm}^{-1})$	$\nu_{\text{calc}} (\text{cm}^{-1})$	$\text{o} - \text{c} (\text{cm}^{-1})$
$1_{11}\text{-}2_{12}$	17213.6180	17213.6146	0.0034
$1_{10}\text{-}2_{11}$		17213.6122	0.0058
$1_{01}\text{-}2_{02}$	17213.5417	17213.5359	0.0058
$2_{12}\text{-}3_{13}$	17213.5145	17213.5174	-0.0029
$2_{11}\text{-}3_{12}$		17213.5137	0.0008
$2_{02}\text{-}3_{03}$	17213.4377	17213.4381	-0.0004
$3_{13}\text{-}4_{14}$	17213.4146	17213.4173	-0.0027
$3_{12}\text{-}4_{13}$		17213.4124	0.0022
$3_{03}\text{-}4_{04}$	17213.3325	17213.3373	-0.0048
$4_{14}\text{-}5_{15}$	17213.3143	17213.3142	0.0001
$4_{13}\text{-}5_{14}$		17213.3081	0.0062
$4_{04}\text{-}5_{05}$	17213.2231	17213.2337	-0.0106
$5_{15}\text{-}6_{16}$	17213.2065	17213.2082	-0.0017
$5_{14}\text{-}6_{15}$		17213.2009	0.0056
$7_{26}\text{-}8_{27}$	17213.1985	17213.2150	-0.0165 ^a
$7_{25}\text{-}8_{26}$		17213.2149	-0.0164 ^a
$5_{05}\text{-}6_{06}$	17213.1221	17213.1271	-0.0050
$6_{16}\text{-}7_{17}$	17213.1054	17213.0993	0.0061 ^a
$6_{15}\text{-}7_{16}$		17213.0907	0.0147 ^a
$6_{06}\text{-}7_{07}$	17213.0125	17213.0176	-0.0051
$7_{17}\text{-}8_{18}$	17212.9911	17212.9875	0.0036 ^a
$7_{16}\text{-}8_{17}$		17212.9777	0.0134 ^a
$9_{28}\text{-}10_{29}$	17212.9621	17212.9814	-0.0193 ^a
$9_{27}\text{-}10_{28}$		17212.9812	-0.0191 ^a
$7_{07}\text{-}8_{08}$	17212.9060	17212.9052	0.0008
$8_{18}\text{-}9_{19}$	17212.8756	17212.8728	0.0028 ^a
$8_{17}\text{-}9_{18}$		17212.8617	0.0139 ^a
$10_{29}\text{-}11_{30}$	17212.8433	17212.8602	-0.0169 ^a
$10_{28}\text{-}11_{29}$		17212.8599	-0.0166 ^a
$8_{08}\text{-}9_{09}$	17212.7846	17212.7899	-0.0053
$9_{19}\text{-}10_{20}$	17212.7541	17212.7551	-0.0010 ^a
$9_{18}\text{-}10_{19}$		17212.7428	0.0113 ^a
$11_{210}\text{-}12_{211}$	17212.7300	17212.7361	-0.0061 ^a
$11_{29}\text{-}12_{30}$		17212.7357	-0.0057 ^a
$9_{09}\text{-}10_{10}$	17212.6697	17212.6716	-0.0019
$10_{110}\text{-}11_{111}$	17212.6331	17212.6345	-0.0014 ^a
$10_{19}\text{-}11_{20}$		17212.6210	0.0121 ^a
$10_{10}\text{-}11_{11}$	17212.5477	17212.5505	-0.0028
$11_{111}\text{-}12_{112}$	17212.5089	17212.5110	-0.0021 ^a
$11_{10}\text{-}12_{11}$		17212.4963	0.0126 ^a
$11_{011}\text{-}12_{012}$	17212.4235	17212.4264	-0.0029
$12_{112}\text{-}13_{113}$	17212.3802	17212.3846	-0.0044 ^a
$12_{11}\text{-}13_{12}$		17212.3686	0.0116 ^a
$14_{213}\text{-}15_{214}$	17212.3397	17212.3462	-0.0065 ^a
$14_{212}\text{-}15_{213}$		17212.3455	-0.0058 ^a

Table 3 (continued)

$N_{K_a K_c}$	$\nu_{\text{obs}} (\text{cm}^{-1})$	$\nu_{\text{calc}} (\text{cm}^{-1})$	$\text{o} - \text{c} (\text{cm}^{-1})$
$12_{012}\text{-}13_{013}$	17212.2984	17212.2994	-0.0010
$13_{113}\text{-}14_{114}$	17212.2566	17212.2553	0.0013
$13_{112}\text{-}14_{113}$	17212.2470	17212.2381	0.0089
$15_{214}\text{-}16_{215}$	17212.2008	17212.2104	-0.0096 ^a
$15_{213}\text{-}16_{214}$		17212.2096	-0.0088 ^a
$13_{013}\text{-}14_{014}$	17212.1697	17212.1696	0.0001
$14_{114}\text{-}15_{115}$	17212.1219	17212.1230	-0.0011
$14_{113}\text{-}15_{114}$	17212.1096	17212.1046	0.0050
$16_{215}\text{-}17_{216}$	17212.0632	17212.0717	-0.0085 ^a
$16_{214}\text{-}17_{215}$		17212.0707	-0.0075 ^a
$14_{014}\text{-}15_{015}$	17212.0346	17212.0368	-0.0022
$15_{115}\text{-}16_{116}$	17211.9886	17211.9878	0.0008
$15_{114}\text{-}16_{115}$	17211.9743	17211.9682	0.0061
$15_{015}\text{-}16_{016}$	17211.9021	17211.9011	0.0010
$16_{116}\text{-}17_{117}$	17211.8504	17211.8498	0.0006
$16_{115}\text{-}17_{116}$	17211.8386	17211.8289	0.0097
$16_{016}\text{-}17_{017}$	17211.7627	17211.7625	0.0002
$17_{117}\text{-}18_{118}$	17211.7087	17211.7087	0.0000
$17_{116}\text{-}18_{117}$	17211.6902	17211.6866	0.0036
$17_{017}\text{-}18_{018}$	17211.6224	17211.6211	0.0013
$18_{118}\text{-}19_{119}$	17211.5661	17211.5648	0.0013
$18_{117}\text{-}19_{118}$	17211.5447	17211.5415	0.0032
$18_{018}\text{-}19_{019}$	17211.4766	17211.4767	-0.0001
$19_{119}\text{-}20_{120}$	17211.4184	17211.4180	0.0004
$19_{118}\text{-}20_{119}$	17211.3938	17211.3934	0.0004
$19_{019}\text{-}20_{020}$	17211.3261	17211.3294	-0.0033
$20_{120}\text{-}21_{121}$	17211.2709	17211.2682	0.0027
$20_{119}\text{-}21_{120}$	17211.2411	17211.2424	-0.0013
$20_{020}\text{-}21_{021}$	17211.1662	17211.1793	-0.0131
$21_{121}\text{-}22_{122}$	17211.1169	17211.1156	0.0013
$21_{120}\text{-}22_{121}$	17211.0842	17211.0885	-0.0043
$21_{021}\text{-}22_{022}$	17211.0265	17211.0262	0.0003
$22_{122}\text{-}23_{123}$	17210.9655	17210.9600	0.0055
$22_{121}\text{-}23_{122}$	17210.9274	17210.9317	-0.0043
$23_{123}\text{-}24_{124}$	17210.8091	17210.8015	0.0076
$23_{122}\text{-}24_{123}$	17210.7638	17210.7720	-0.0082

^a Weight is 0.1 in the least-squares fit.

to the origin band [6]. In order to identify the carrier this wavelength region was scanned with both normal and deuterated precursors using the cw-CRD spectrometer. As a result rotationally resolved bands were observed in the 581 nm region (Figs. 3 and 4). However a complete reproduction of the rotational structure did not prove possible using an asymmetric-top Hamiltonian as for the 604 nm band. The spectrum could only be analysed for $K_a = 0, 1, 2$ transitions in the P -branch. The assignments are given in Tables 3 and 4 and the molecular constants in Table 2. The observed turning points in the R -branch could not be reproduced by the simulations. This may be caused by Fermi and Coriolis interactions [12].

It was considered if the 581 nm band could be the origin of another isomer of C_6H_4^+ . In this case the shift of the transition energy for the fully deuterated species should be approximately equal to that of $\text{C}_6\text{H}_4^+/\text{C}_6\text{D}_4^+$ (66.94 cm^{-1}). However, the shift observed on deutera-

Table 4
The observed and fitted rovibronic lines in the 581 nm band of the ${}^2A''$ – X^2A'' electronic transition of $C_6D_4^+$

$N_{K_a K_c}$	$\nu_{\text{obs}} \text{ (cm}^{-1}\text{)}$	$\nu_{\text{calc}} \text{ (cm}^{-1}\text{)}$	$o - c \text{ (cm}^{-1}\text{)}$
5 ₀ 5–6 ₀ 6	17217.6289	17217.6227	0.0062
7 ₂ 6–8 ₂ 7	17217.6012	17217.6105	–0.0093
7 ₂ 5–8 ₂ 6		17217.6101	–0.0089
6 ₁ 6–7 ₁ 7	17217.5804	17217.5777	0.0027
6 ₁ 5–7 ₁ 6	17217.5704	17217.5622	0.0082
6 ₀ 6–7 ₀ 7	17217.5229	17217.5221	0.0008
8 ₂ 7–9 ₂ 8	17217.5012	17217.5040	–0.0028
8 ₂ 6–9 ₂ 7		17217.5035	–0.0023
7 ₁ 7–8 ₁ 8	17217.4743	17217.4752	–0.0009
7 ₁ 6–8 ₁ 7	17217.4573	17217.4575	–0.0002
7 ₀ 7–8 ₀ 8	17217.4177	17217.4186	–0.0009
9 ₂ 8–10 ₂ 9	17217.3932	17217.3947	–0.0015
9 ₂ 7–10 ₂ 8		17217.3939	–0.0007
8 ₁ 8–9 ₁ 9	17217.3637	17217.3698	–0.0061
8 ₁ 7–9 ₁ 8	17217.3568	17217.3499	0.0069
8 ₀ 8–9 ₀ 9	17217.3155	17217.3122	0.0033
10 ₂ 9–11 ₂ 10	17217.2811	17217.2824	–0.0013
10 ₂ 8–11 ₂ 9		17217.2814	–0.0003
9 ₁ 9–10 ₁ 10	17217.2508	17217.2616	–0.0108
9 ₁ 8–10 ₁ 9	17217.2446	17217.2395	0.0051
9 ₀ 9–10 ₀ 10	17217.2070	17217.2031	0.0039
11 ₂ 10–12 ₂ 11	17217.1656	17217.1673	–0.0017
11 ₂ 9–12 ₂ 10		17217.1659	–0.0003
10 ₁ 10–11 ₁ 11	17217.1394	17217.1505	–0.0111
10 ₁ 9–11 ₁ 10	17217.1301	17217.1262	0.0039
10 ₀ 10–11 ₀ 11	17217.0959	17217.0910	0.0049
12 ₂ 11–13 ₂ 12	17217.0495	17217.0493	0.0002
12 ₂ 10–13 ₂ 11		17217.0475	0.0020
11 ₁ 11–12 ₁ 12	17217.0262	17217.0365	–0.0103
11 ₁ 10–12 ₁ 11	17217.0119	17217.0100	0.0019
11 ₀ 11–12 ₀ 12	17216.9824	17216.9762	0.0062
13 ₂ 12–14 ₂ 13	17216.9322	17216.9284	0.0038
13 ₂ 11–14 ₂ 12		17216.9261	0.0061
12 ₁ 12–13 ₁ 13	17216.9111	17216.9196	–0.0085
12 ₁ 11–13 ₁ 12	17216.8965	17216.8909	0.0056
12 ₀ 12–13 ₀ 13	17216.8681	17216.8585	0.0096
14 ₂ 13–15 ₂ 14	17216.8123	17216.8047	0.0076
14 ₂ 12–15 ₂ 13		17216.8018	0.0105
13 ₁ 13–14 ₁ 14	17216.7907	17216.7999	–0.0092
13 ₁ 12–14 ₁ 13	17216.7641	17216.7689	–0.0048
13 ₀ 13–14 ₀ 14	17216.7486	17216.7380	0.0106
15 ₂ 14–16 ₂ 15	17216.6837	17216.6780	0.0057
15 ₂ 13–16 ₂ 14		17216.6746	0.0091
14 ₁ 14–15 ₁ 15	17216.6710	17216.6772	–0.0062
14 ₁ 13–15 ₁ 14	17216.6343	17216.6441	–0.0098
15 ₁ 15–16 ₁ 16	17216.5553	17216.5518	0.0035
15 ₁ 14–16 ₁ 15	17216.5064	17216.5165	–0.0101
16 ₁ 16–17 ₁ 17	17216.4264	17216.4234	0.0030
16 ₁ 15–17 ₁ 16	17216.3762	17216.3860	–0.0098
17 ₁ 17–18 ₁ 18	17216.2965	17216.2922	0.0043
17 ₁ 16–18 ₁ 17	17216.2466	17216.2526	–0.0060
18 ₁ 18–19 ₁ 19	17216.1634	17216.1582	0.0052
18 ₁ 17–19 ₁ 18	17216.1083	17216.1163	–0.0080

tion is only 4.4 cm^{-1} , and thus excludes this possibility. Rather, these results suggest that this band is a transition to a vibrationally excited level of a $C_6H_4^+$ isomer. The rotational constants of a *trans*- $H-C\equiv C-CH=CH-C\equiv CH^+$ isomer, which could be a candidate due to similarity of the structure with that of the 604 nm band, were calculated to be $A = 1.451$, $B = 0.0489$, and $C = 0.0473 \text{ cm}^{-1}$ (B3LYP/cc-pVTZ Gaussian 03 [13]). These are not in agreement with the deduced constants (Table 2). On the other hand, the B and C constants inferred for the ground state agree within the errors of the fit to those from the analysis of 604 nm band (Table 1). Therefore the 581 nm band is assigned to a transition from the ground state to vibrationally excited level of $C_6H_4^+$ of the ${}^2A''$ – X^2A'' system.

The 585.3 nm peak in the matrix spectrum (Fig. 4 in [6]) is thus an overlap of the transition observed at 581 nm in the gas phase and that of another isomer, because the site structure is not the same as on the origin band (at 609 nm in neon). This isomer was not detected in the present work presumably because the discharge sources used in the two experiments are quite different.

3.3. *Ab initio* calculations

To assign the vibration excited in the upper electronic state *ab initio* calculations were carried out using MOLPRO [14]. At first the adiabatic transition energies of the ${}^2A''$ – X^2A'' transition of $C_6H_4^+$ ($H-C\equiv C-C\equiv C-CH=CH_2^+$), using optimised geometry, were computed to be 2.18 and 1.95 eV using CASSCF [15,16] and RS2C (CASPT2) [17,18] method, respectively, with the cc-pVTZ basis sets. The calculated values are in good agreement with the experiment, 2.05 eV. Subsequently the vibrational frequencies of the normal modes [19] of $C_6H_4^+$ and $C_6D_4^+$ in the ${}^2A''$ excited state were calculated using a simpler CASSCF method (Table 5). All 10 π orbitals of the molecule were included in the active space: $6a''$ and $4a'$. The core orbitals were kept uncorrelated. Assignment of the vibrations of the ground state, the excited state and the deuterated species was based on Duschinsky matrices.

To assign the vibrational excitation associated with the 581 nm band, both the frequency and their ratio for $C_6H_4^+$ and $C_6D_4^+$ were used as indicated in Fig. 5. The electronic transitions observed in the absorption spectrum in a neon matrix, 600 (599) and 591 (590) nm in $C_6H_4^+$ ($C_6D_4^+$) [6], and the 581 nm band observed in the gas phase also plotted in the same figure. The vibrational mode excited in the upper state should have a' symmetry due to the selection rules for ${}^2A''$ – X^2A'' transition. The position of the 581 nm band implies a vibrational frequency of 668.8 cm^{-1} and agrees with the value 713.6 cm^{-1} calculated for the in-plane bending mode. The two bands observed in the matrix, which correspond to 232 and 494 cm^{-1} frequencies, are also in

Table 5

Calculated and observed vibrational frequencies (cm^{-1}) in the ground X^2A'' and excited $^2A''$ state of C_6H_4^+ and C_6D_4^+

Mode	Symmetry	C_6H_4^+				C_6D_4^+			
		X^2A''		$^2A''$		X^2A''		$^2A''$	
		$\omega_{\text{Cal.}}$	Intensity ^b	$\nu_{\text{Obs.}}$	$\omega_{\text{Calc.}}$	$\omega_{\text{Cal.}}$	Intensity ^b	$\nu_{\text{Obs.}}$	$\omega_{\text{Calc.}}$
17	a'	98	0.0		97	90	0.0		90
24	a''	136	0.0		131	122	0.0		118
16	a'	219	0.1	232.3 ^c	222	207	0.2	213.6 ^c	211
23	a''	304	0.0		349	271	0.0		300
15	a'	434	0.1		430	423	0.3		424
22	a''	489	0.4		457	434	0.2		429
14	a'	503	2.1	493.7 ^c	496	471	1.4	468.1 ^c	464
21	a''	621	0.0		548	564	0.1		480
13	a'	631	2.2		591	490	1.0		451
20	a''	709	1.5		486	557	0.9		373
12	a'	731	2.2	668.8	714	667	2.9	606.3	653
19	a''	1000	1.6		933	770	0.7		718
11	a'	1111	1.1		1058	892	0.4		863
18	a''	1165	0.6		1007	954	0.1		853
10 ^d	a'	1311	3.9		1273	1125	1.2		1107
9	a'	1361	11.9		1222	1077	1.3		1055
8 ^d	a'	1566	11.3		1533	1526	36.7		1390
7 ^d	a'	1648	17.8		1612	1323	5.8		1236
6	a'	2119	33.7		1989	2013	48.0		1935
5	a'	2258	100.0		2208	2250	100.0		2177
4	a'	3313	1.0		3320	2409	1.3		2407
3	a'	3339	0.5		3337	2471	1.8		2465
2	a'	3429	0.6		3443	2559	0.2		2570
1	a'	3575	4.4		3558	2741	1.6		2699

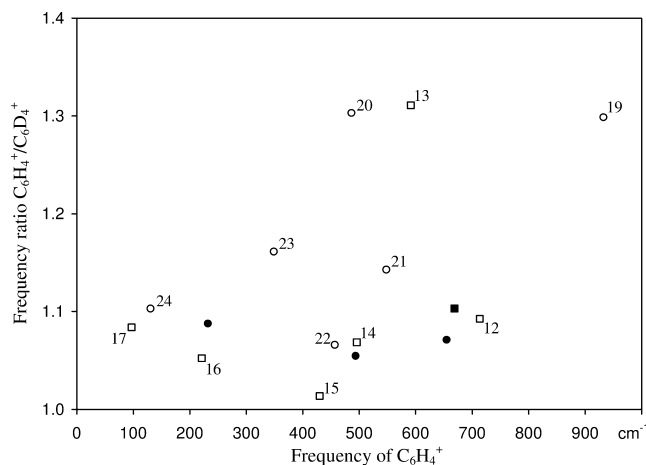
^a Using CASSCF/cc-pVTZ.^b Relative infrared intensity.^c Neon-matrix data in [6].^d The three modes are mixed.

Fig. 5. The calculated frequencies and their ratios $\omega(\text{C}_6\text{H}_4^+)/\omega(\text{C}_6\text{D}_4^+)$ assuming a harmonic potential in the upper $^2A''$ state. The observed values are $\nu(\text{C}_6\text{H}_4^+)/\nu(\text{C}_6\text{D}_4^+)$. “●” indicates an observed value in gas phase, “○” in neon-matrix, “□” calculated ones with a' symmetry and “○” calculated ones with a'' symmetry. The numbers attached in the calculated values indicate the vibrational modes as listed in Table 5.

accord with the 222 and 496 cm^{-1} calculated values and their ratio. Therefore the 600 and 591 nm bands in the matrix and the 581 nm one in the gas phase can be assigned transitions from the lowest level in the ground

state to the upper electronic state involving the excitation of the ν_{16} , ν_{14} , and ν_{12} vibrational modes, respectively. Additionally, the calculation indicates that several overtones and combination bands can be found around the ν_{12} vibrational level: $\nu_{14} + \nu_{16}$ (718 cm^{-1}), $\nu_{13} + \nu_{17}$ (689), $2\nu_{23}$ (698), and $\nu_{21} + \nu_{24}$ (679) with a' symmetry and $\nu_{16} + \nu_{22}$ (679) and $\nu_{16} + \nu_{20}$ (708) with a'' symmetry. The observed irregular rotational structure of the 581 nm band may be due to Fermi and Coriolis interactions among such adjacent vibrational levels.

Vibrational frequencies, infrared intensities (Table 5) and a permanent dipole moment in the ground state were also calculated using the same method and basis set. This may help in the search for the vibrational transitions in the infrared region. The permanent dipole moment in the ground state was calculated to be $\mu_a = 0.63$ and $\mu_b = 0.38\text{ D}$. Thus in the pure rotational spectrum the a -type transition should be 2.8 times stronger than the b -type one and suggests that the detection of C_6H_4^+ is possible.

4. Summary

The electronic absorption spectrum of the $^2A''-X^2A''$ origin band of the nonlinear carbon chain radical C_6H_4^+

was rotationally resolved by cw-CRD spectroscopy. It was analysed using a least-squares method, and the rotational constants of the ground and excited states were determined accurately. The 581 nm band observed under the same discharge conditions is assigned to the same electronic transition of $C_6H_4^+$ but involving the excitation of the ν_{12} vibrational mode in the upper state based on comparison with ab initio results. The presented data provide a basis for future observations of the $C_6H_4^+$ radical in both millimetre and infrared regions.

Acknowledgment

This work has been supported by the Swiss National Science Foundation (Project 200020-100019).

References

- [1] J.H. Callomon, *Can. J. Phys.* 34 (1956) 1046.
- [2] W.E. Sinclair, D. Pfluger, H. Linnartz, J.P. Maier, *J. Chem. Phys.* 110 (1999) 296.
- [3] D. Pfluger, T. Motylewski, H. Linnartz, W.E. Sinclair, J.P. Maier, *Chem. Phys. Lett.* 329 (2000) 29.
- [4] P. Cias, O. Vaizert, A. Denisov, J. Mes, H. Linnartz, J.P. Maier, *J. Phys. Chem. A* 106 (2002) 9890.
- [5] See for example: H. Linnartz, T. Motylewski, J.P. Maier, *J. Chem. Phys.* 109 (1998) 3819.
- [6] M. Araki, H. Linnartz, P. Cias, A. Denisov, J. Fulara, A. Batalov, I. Shnitko, J.P. Maier, *J. Chem. Phys.* 118 (2003) 10561.
- [7] M. Araki, P. Cias, A. Denisov, J. Fulara, J.P. Maier, *Can. J. Chem.* 82 (2004) 1.
- [8] M. Ohishi, W.M. Irvine, N. Kaifu, in: P.D. Singh (Ed.), *Astrochemistry of Cosmic Phenomena*, 1992, pp. 171–177.
- [9] P. Birza, D. Khoroshev, A. Chirokolava, T. Motylewski, J.P. Maier, *Chem. Phys. Lett.* 382 (2003) 245.
- [10] M. Hippler, M. Quack, *Chem. Phys. Lett.* 314 (1999) 273.
- [11] D. Luckhaus, M. Quack, *Mol. Phys.* 63 (1989) 745.
- [12] D.L. Joo, D.J. Clouthier, A.J. Merer, *J. Chem. Phys.* 101 (1994) 31.
- [13] M.J. Frisch et al., *Gaussian 03*, Revision A.1, Inc., Pittsburgh, PA, 2003.
- [14] MOLPRO, a package of ab initio programs designed by H.-J. Werner and P.J. Knowles, version 2002.1, with contributions from others. Available from <www.molpro.net>.
- [15] P.J. Knowles, H.-J. Werner, *Chem. Phys. Lett.* 115 (1985) 259.
- [16] H.-J. Werner, P.J. Knowles, *J. Chem. Phys.* 82 (1985) 5053.
- [17] H.-J. Werner, *Mol. Phys.* 89 (1996) 645.
- [18] P. Celani, H.-J. Werner, *J. Chem. Phys.* 112 (2000) 5546.
- [19] G. Rauhut, A. El Azhary, F. Eckert, U. Schumann, H.-J. Werner, *Spectrochim. Acta A* 55 (1999) 647.

5.4 Curriculum vitae of author

Personal information:

Name: BIRZA A. PETRE AUREL

Day of birth: 30.05.1973

Place: Draganesti-Olt, Romania

Nationality: Romanian

Marital status: Single

Education :

1989-1992 Theoretical High school Draganesti-Olt

1994-1998 Faculty of Physics Bucharest ‘Molecular and Atomic Physics, Astrophysics’ section.

Graduation paper on Molecular Physics:

‘The Study of the Initiating Process of the Acrylamide Polymerization’

1998-2000 Faculty of Physics Bucharest

MS degree in ‘Molecular and Atomic Physics, Astrophysics’

Dissertation paper on Astrophysics:

‘The Determination of the Contact Moments during the Total Solar Eclipse’.

2001-2004 Ph.D. Department of Chemistry, University of Basel

Publication in peer reviewed journals:

1. The Acrylamide Polymerization Initiation Reaction Induced by γ Irradiation: An EPR and Extended Hückel Study.

C.G. Palivan, P. Birza, M. Dragusin, Roum. Reports in Phys., **51**, (1999), (7-10), 961-967.

2. Rotationally resolved $A^2\Pi_u-X^2\Pi_g$ electronic transition of NC_6N^+ .

H. Linnartz, D. Pfluger, O. Vaizert, P. Cias, P. Birza, D. Khoroshev, J. P. Maier, Journal of Chemical Physics, **116**, (2002), 924-927.

3. Cw cavity ring down spectroscopy in a pulsed planar plasma expansion.

P. Birza, T. Motylewski, D. Khoroshev, A. Chirokolava, H. Linnartz, J.P. Maier, Chem. Phys., **283**, (2002), 119

4. Lifetime broadening in the gas phase $B^2\Pi - X^2\Pi$ electronic spectrum of C_8H .

P. Birza, D. Khoroshev, A. Chirokolava, T. Motylewski, J. P. Maier. Chemical Physics Letters, **382** (2003), 245-248

5. Rotationally resolved electronic spectroscopy of a nonlinear carbon chain radical $C_6H_4^+$

D. Khoroshev, M. Araki, P. Kolek, P. Birza, A. Chirokolava, J. P. Maier, Journal of Molecular Spectroscopy **227** (2004), 81–89

6. Rotationally Resolved Electronic Spectrum of Propadienylidene

P. Birza, A. Chirokolava, M. Araki, P. Kolek, and J. P. Maier Journal of Molecular Spectroscopy (in preparation)

